Investigation of Residual Stress and Microstructure Effects on the Fatigue Behaviour of an Aluminium-Silicon Eutectic Alloy Produced by Laser Powder Bed Fusion

Vom Fachbereich 13 – Bau- und Umweltingenieurwissenschaften
der Technischen Universität Darmstadt

zur
Erlangung des akademischen Grades eines
Doktor-Ingenieurs

genehmigte
DISSERTATION

vorgelegt von

M. Sc. Ilaria Roveda

aus Vittorio Veneto, Italien

1. Gutachten: Prof. Dr.-Ing. Michael Vormwald
2. Gutachten: Prof. Dr.-Ing. Uwe Zerbst
Tag der Einreichung: 24. Februar 2023
Tag der mündlichen Prüfung: 26. Juni 2023

Darmstadt 2023

D 17

Ilaria Roveda
Investigation of Residual Stress and Microstructure Effects on the Fatigue Behaviour of an Aluminium-Silicon Eutectic Alloy Produced by Laser Powder Bed Fusion

Darmstadt, Technische Universität Darmstadt,
Jahr der Veröffentlichung der Dissertation auf TUprints: 2023
URN: urn:nbn:de:tuda-tuprints-244006
URL: https://tuprints.ulb.tu-darmstadt.de/id/eprint/24400
Tag der mündlichen Prüfung: 26.06.2023

Abstract

The advent of additive manufacturing (AM) techniques has paved the way for new possibilities in the production of topologically optimized, near-net shape components. In recent decades, research triggered numerous developments in the field of metal additive manufacturing. Among the AM techniques, Laser Powder Bed Fusion (PBF-LB/M) is a powder-based technique, in which a laser beam selectively melts the material. PBF-LB/M is widely used for the production of near-eutectic Al-Si alloy components, highly demanded material in the aerospace, automotive and biomedical fields due to attractive properties such as excellent corrosion resistance, processability and thermal conductivity at a low price.
Whilst the PBF-LB/M technology exhibits high potential, at the same time, it presents major challenges that still prevent its wide and safe industrial application. In particular, fatigue properties are essential for load-bearing applications and are less studied in the literature than static properties.
The PBF-LB/M process is characterised by localized thermal cycles, with extremely rapid heating and cooling, as well as a simultaneous melting of the top powder layer and re-melting of the previously solidified layers. The complex cycles can lead to a unique multi-scale microstructure with a high content of manufacturing defects and high-level residual stress (RS). These aspects influence in determining the fatigue resistance of a component. Therefore, a prediction of the material behaviour is not possible without experimental data on the microstructure, defect distribution, and RS fields. For this reason, the aim of the study is to give a comprehensive characterisation of the microstructure and residual stress state as a function of the heat treatments. Gathering this information, in addition to the analysis of the defect content, the fatigue behaviour of PBF-LB/M AlSi10Mg can be more accurately interpreted. Several techniques have been applied for this purpose: optical and scanning electron microscopy, x-ray micro-computed tomography (μCT), diffraction methods for residual stress analysis, as well as static and cyclic testing.
As the nanometric PBF-LB/M AlSi10Mg as-built microstructure significantly differs from the as-cast material, its evolution during post-processing heat treatments will also differ greatly. In fact, some studies observed that already at temperatures below 300°C, microstructural and RS modifications are triggered. Therefore, this study focuses on

evaluating the effects of two low temperature heat treatments (265°C for 1 hour, HT1, and 300°C for 2 hours, HT2), which have been still scarcely studied in the literature. It is shown herein that the microstructure and residual stress state are subject to significant changes at these temperatures. A precipitation of the supersaturated silicon from the aluminium matrix was observed at 265°C. At 300°C, the fragmentation of the eutectic silicon network, present in the as-built condition, occurred. Various techniques were combined to give a full picture of the changes in the residual stress state: energy-dispersive laboratory x-ray diffraction (EDXRD) provided information on the near-surface volume, while synchrotron x-ray diffraction (SXRD) and neutron diffraction (ND) allowed the investigation of the bulk. These measurements showed that the microstructure changes are accompanied by a partial relaxation of the residual stresses in the bulk, superior in the case of the 265°C heat treatment (-55%) than at 300°C (-35%). The lower RS reduction in the case of HT2 is ascribed to the spheroidization of the silicon phase.
These microstructure and RS modifications can have a beneficial effect on the fatigue properties. An extensive experimental campaign was deployed to cover High Cycle Fatigue (HCF) testing at stress ratio 0.1, and fatigue crack growth tests at stress ratios -1, 0.1 and 0.8. This allowed for the characterisation of the fatigue life through the description of S-N curves, as well as the investigation of the fatigue crack propagation threshold in the physically short (cyclic R-curve) and long ($\mathrm{d}a/\mathrm{d}N - \Delta K$ curve) crack regime.
Regarding fatigue crack propagation properties, it is observed that the microstructure is the prevailing factor influencing the fatigue resistance. The near-threshold regime is controlled by closure phenomena: the progressive increase in ductility after HT1 and HT2 leads to the development of plasticity-induced crack closure effects, which hinders fatigue crack propagation.
Differently, considering the total fatigue life by means of S-N curves, the beneficial effect of the heat treatments was overshadowed by the effect of manufacturing defects. Prior to the fatigue testing, the defect distribution was analysed by means of μCT. Subsequently, the peak over threshold method was successfully applied to provide a prediction of the killer defects.
Since defects play a governing role in the fatigue behaviour, defect-tolerant fatigue design has proven to be crucial. The effect of defects on crack initiation and early propagation is considered by deploying fracture mechanics approaches, which cover the specific characteristics of so-called short fatigue cracks. These approaches have been adopted to re-elaborate the experimental data, taking defects into account. This allowed the threshold stress level to be related to the defect size. The Kitagawa-Takahashi diagram, obtained by various methods such as the El-Haddad model, the Murakami's $\sqrt{area}$ approach and the cyclic R-curve analysis, proved to be a good approach to establish the maximum permissible load, below which no fatigue crack growth occurs.

Zusammenfassung

Die Entwicklung von additiven Fertigungsverfahren (*Additive Manufacturing*, AM) hat neue Möglichkeiten bei der Herstellung topologisch optimierter, endkonturnaher Bauteile eröffnet. In den letzten Jahrzehnten gab es – dank eines immensen Forschungsinteresses – zahlreiche Entwicklungen auf dem Feld der additiven Fertigung von Metallen. Unter den AM Verfahren wird das pulverbettbasierte Schmelzen mittels Laserstrahl (Eng.: *Laser Powder Bed Fusion*, PBF-LB/M) häufig für die Herstellung von Bauteilen aus nah-eutektischen Al-Si-Legierungen verwendet. Aufgrund attraktiver Eigenschaften wie ihrer hervorragenden Korrosionsbeständigkeit, Verarbeitbarkeit und Wärmeleitfähigkeit bei gleichzeitig niedrigem Preis sind diese Legierungen in der Luft- und Raumfahrt, im Automobilbau und in der Biomedizin sehr gefragt. Die PBF-LB/M-Technologie weist zwar ein hohes Potenzial auf, ist aber gleichzeitig mit großen Herausforderungen verbunden, die eine breite und sichere industrielle Anwendung noch verhindern. Insbesondere die Ermüdungseigenschaften der resultierenden Materialien sind für Bauteile in tragenden Anwendungen von entscheidender Bedeutung und werden in der Literatur weniger häufig untersucht als statische Eigenschaften. Das PBF-LB/M-Verfahren ist durch thermische Zyklen mit extrem schnellem lokalem Aufheizen und Abkühlen sowie gleichzeitigem Schmelzen der oberen Pulverschicht und Wiederaufschmelzen der zuvor erstarrten Schichten gekennzeichnet. Diese komplexen Zyklen können zu einer einzigartigen multiskalaren Mikrostruktur mit einem hohen Gehalt an Herstellungsfehlern und hohen Eigenspannungen führen. Diese Aspekte können die Ermüdungsfestigkeit eines Bauteils beeinflussen. Daher ist eine Vorhersage des Werkstoffverhaltens ohne experimentelle Daten hinsichtlich der Mikrostruktur, der Defektverteilung und der Eigenspannungen nicht möglich. Das Ziel dieser Studie ist eine umfassende Charakterisierung der Mikrostruktur und der Eigenspannungen einer mittels PBF-LB/M-Verfahren gefertigten AlSi10Mg-Legierung in Abhängigkeit ihres Wärmebehandlungszustandes. Mithilfe dieser Informationen kann zusammen mit einer Analyse des Defektgehaltes das Ermüdungsverhalten von PBF-LB/M AlSi10Mg interpretiert werden. Für die Untersuchung der oben genannten Eigenschaften wurden verschiedene Techniken angewandt: optische Mikroskopie und Rasterelektronenmikroskopie, Röntgen-Mikrotomographie (μCT), Beugungsmethoden für die Eigenspannungsermittlung sowie statische und zyklische mechanische Versuche. Da sich die nanometrische Mikrostruk-

tur der AlSi10Mg-Legierung, die sich aus dem PBF-LB/M-Verfahren ergibt, erheblich von konventionell gegossenem Material unterscheidet, ist davon auszugehen, dass ihre Entwicklung während einer Wärmebehandlung ebenfalls stark unterschiedlich ist. Tatsächlich wurde in einigen Studien festgestellt, dass bereits bei Temperaturen unter 300 °C Mikrostruktur- und Eigenspannungsveränderungen ausgelöst werden. Daher konzentriert sich diese Studie insbesondere auf die Bewertung der Auswirkungen von zwei Wärmebehandlungen bei niedriger Temperatur (265°C für 1 Stunde, HT1, und 300°C für 2 Stunden, HT2), die nach aktuellem Stand der Literatur bisher kaum untersucht worden sind. Es wird gezeigt, dass die Mikrostruktur und der Eigenspannungzustand bei diesen Temperaturen erheblichen Veränderungen unterworfen sind. Eine Ausscheidung von übersättigtem Silizium aus der Aluminiummatrix wurde bei 265°C beobachtet. Bei 300°C kam es zur Fragmentierung des eutektischen Siliziumnetzwerks, welches im Ausgangszustand vorhanden war. Um ein vollständiges Bild der Veränderungen des Eigenspannungszustandes zu erhalten, wurden verschiedene Techniken kombiniert: Energiedispersive Labor-Röntgendiffraktion (EDXRD) lieferte Informationen über das oberflächennahe Volumen, während Synchrotron-Röntgendiffraktion (SXRD) und Neutronendiffraktion (ND) die Untersuchung des inneren Volumens ermöglichen. Diese Messungen zeigen, dass die Mikrostrukturänderungen mit einer teilweisen Reduzierung der Eigenspannungen im inneren Volumen einhergehen, die bei der Wärmebehandlung bei 265°C (-55%) größer ist als bei 300°C (-35%). Die geringere Reduzierung der Eigenspannungen im Fall von HT2 wird auf die Sphäroidisierung der Siliziumphase zurückgeführt. Die beobachteten Mikrostruktur- und Eigenspannungsveränderungen können sich positiv auf die Ermüdungseigenschaften auswirken. Es wurde eine umfangreiche Versuchskampagne durchgeführt, die Zeitfestigkeitsversuche (High Cycle Fatigue, HCF) bei einem Spannungsverhältnis von R=0,1 und Ermüdungsrisswachstumsversuche bei Spannungsverhältnissen von R=-1, 0,1 und 0,8 umfasste. Dies ermöglichte die Charakterisierung der Zeitfestigkeit mithilfe von Wöhlerkurven sowie die Untersuchung der Ermüdungsrissausbreitung im physikalisch kurzen (zyklische R-Kurve) und langen ($\mathrm{d}a/\mathrm{d}N - \Delta K$-Kurve) Rissbereich. Hinsichtlich des Ermüdungsrisswachstums ist festzustellen, dass die Mikrostruktur der beherrschende Faktor ist, der die Ermüdungsbeständigkeit beeinflusst. Der Schwellenwertbereich wird von Rissschließeffekten gesteuert: der progressive Anstieg der Duktilität nach HT1 und HT2 führt zur Entwicklung von plastizitäts-induziertem Rissschließen, das die Ausbreitung von Ermüdungsrissen behindert. Betrachtet man dagegen die gesamte Ermüdungslebensdauer anhand von Wöhlerkurven, so wird die positive Wirkung der Wärmebehandlungen von den Auswirkungen der Herstellungsfehler überschattet. Vor der Ermüdungsprüfung wurde die Fehlerverteilung mit Hilfe von Röntgen-Mikrotomographie analysiert. Anschließend wurde die *Peak-over-Threshold*-Methode erfolgreich angewandt, um eine Vorhersage der Größe und der Position der fatalen Defekte zu ermöglichen. Da Defekte eine entscheidende Rolle

für das Ermüdungsverhalten spielen, hat sich eine defekttolerante Bauteilauslegung gegen Ermüdung als zielführend erwiesen. Die Auswirkung von Defekten auf die Rissentstehung und Ihre frühe Ausbreitung wird durch den Einsatz bruchmechanischer Ansätze berücksichtigt, die die spezifischen Eigenschaften sogenannter kurzer Ermüdungsrisse abdecken. Diese Ansätze wurden verwendet, um die experimentellen Daten unter Berücksichtigung von Defekten zu rekonstruieren. Auf diese Weise konnte die Schwellenwertspannung, oberhalb derer kein Rissarrest stattfindet (Dauerfestigkeit), in Abhängigkeit der initialen Defektgröße bestimmt werden. Die Darstellung als Kitagawa-Takahashi-Diagramm, das mit verschiedenen Methoden wie dem El-Haddad-Modell, dem $\sqrt{area}$-Ansatz von Murakami und der zyklischen R-Kurven-Analyse ermittelt wurde, erwies sich als guter Ansatz zur Bestimmung der maximal zulässigen Belastung.

Contents

Acknowledgements 1

Abbreviation 3

1. Introduction 5

2. State of the art 11
2.1. Laser Powder Bed Fusion Additive Manufacturing of Al-Si-Mg alloys 11
2.2. Post-processing of Al-Si-Mg alloys produced by Laser Powder Bed Fusion . 12
2.2.1. Differential Scanning Calorimetry 13
2.3. Defect formation in Al-Si-Mg alloys produced by Laser Powder Bed Fusion 15
2.4. Residual stress state in Al-Si-Mg alloys produced by Laser Powder Bed Fusion 16
2.4.1. Process-induced residual stress state 16
2.4.2. Residual stress classification 16
2.4.3. Process parameter optimisation for reducing residual stress 17
2.4.4. Heat treatments for residual stress optimisation 19
2.5. Mechanical properties of Al-Si-Mg alloys produced by Laser Powder Bed Fusion 21
2.5.1. Quasi-static mechanical properties 21
2.5.2. Fatigue properties 23

3. Materials and Methods 31
3.1. AlSi10Mg samples production by Laser Powder Bed Fusion 31
3.2. Microstructure and mechanical properties characterization 33
3.3. Residual stress characterization 35
3.3.1. Laboratory Energy Dispersive X-rays 38
3.3.2. Neutron Diffraction 39
3.3.3. Synchrotron X-ray Diffraction 40
3.3.4. Measured points and optics arrangement 41
3.3.5. Stress-free reference (d_0) determination 44

3.4. Fatigue behaviour of Al-Si-Mg alloys produced by Laser Powder Bed Fusion 46
3.4.1. Fatigue crack propagation . . . 46
3.4.2. High Cycle Fatigue . . . 51
3.4.3. Cyclic stress-strain response . . . 51
3.4.4. Modelling of fatigue resistance . . . 53

4. Microstructure, Mechanical Properties and Residual Stress Characterisation 59
4.1. Microstructure characterisation . . . 59
4.1.1. Scanning electron microscopy (SEM) . . . 59
4.1.2. X-ray microtomography (μCT) . . . 62
4.2. Mechanical properties . . . 64
4.3. Residual stress state in SENB samples . . . 68
4.3.1. Laboratory Energy Dispersive X-rays . . . 68
4.3.2. Stress-free reference d_0 . . . 71
4.3.3. Neutron Diffraction . . . 77
4.3.4. Synchrotron X-ray Diffraction . . . 81
4.3.5. The effect of internal voids on residual stress measurements . . . 84
4.4. Final remarks and conclusion . . . 84

5. Fatigue Crack Propagation Behaviour 87
5.1. Short crack growth regime . . . 87
5.2. Long crack growth regime . . . 87
5.3. Effect of heat treatments on fatigue crack propagation . . . 94
5.4. Conclusion . . . 100

6. Fatigue Behaviour: Experiments and Modelling 103
6.1. Cyclic stress-strain response . . . 103
6.2. High Cycle Fatigue resistance . . . 105
6.2.1. Defects at the fracture origin . . . 107
6.2.2. Determination of the $\Delta K - N$ curves . . . 112
6.2.3. Modelling of fatigue resistance . . . 116
6.3. Conclusion . . . 123

7. Summary and concluding remarks 125

A. Heat treatment documentation 129

B. Peak-Over-Threshold method for μCT data analysis 131

C. HCF parameter and test results **135**

D. Masing's behaviour of the PBF-LB/M AlSi10Mg alloy **141**

E. Synchrotron X-ray diffraction results **143**

Acknowledgements

This thesis is the result of the research work conducted during my doctoral studies at the weld mechanics and non-destructive microtesting sections of the Bundesanstalt für Materialforschung und -Prüfung (BAM) in Berlin. The project was supported by internal Bundesanstalt für Materialforschung und -prüfung (BAM) funding.

An important contribution was made by the Institute of Materials Research, German Aerospace Center (DLR), in Cologne, who provided the material for this study. In this regard, I would like to thank Guillermo Requena and Jan Haubrich for their helpfulness and valuable scientific contribution.
Moreover, I would like to acknowledge all the people whose technical and experimental contributions made this work possible. Romeo Saliwan Neumann, for his guidance and technical assistance during the SEM microstructural investigation. Björn Mieller, for performing the heat treatments. Mareike Kirstein and Marina Marten, for the metallographic sample preparations and their constant availability and competence. Karsten Zieger, for conducting the roughness measurements. Thorid Lange, for carrying out the nanoindentation measurements. Ralf Häcker, for his involvement in the tensile testing campaign.
This project gave me the opportunity to perform experiments at various large-scale facilities in Europe. I would like to acknowledge the Institute Laue-Langevin (ILL), France, and Thilo Pirling in particular, for the Neutron diffraction beamtime on SALSA. I am also thankful to the Helmholtz-Zentrum Berlin für Materialien und Energie and Manuela Klaus and Christopf Genzel, for granting access to the LIMAX-160 instrument at the X-Ray Corelab Facility and for their valuable technical and scientific support. I express my appreciation to the European Synchrotron Radiation Facility (ESRF), France, and Andrew Fitch for the Synchrotron diffraction beamtime on ID22. Finally, all my colleagues from whom I learned a lot and with whom I shared gruelling but entertaining shifts.

I would like to express my special thanks to my supervisors. Mauro Madia, without whom this project would not have come about, who provided me with the opportunity to undertake this new and challenging experience. Itziar Serrano Munoz, whose positive and reassuring attitude has always encouraged me on my path and served as a valuable

source of scientific advice and much more.
I would like to express my gratitude towards Professor Michael Vormwald, who kindly accepted the role of main supervisor and provided many opportunities for enriching discussions and exchange of ideas. Special thanks to Professor Uwe Zerbst for overseeing my project and offering valuable technical insights. A special mention to Professor Giovanni Meneghetti for providing me with my first research opportunity and consistently offering his invaluable scientific advice.

During my time at BAM, I received extraordinary help from many colleagues. The connections I have built over these three years have surpassed my expectations, and I consider myself fortunate. I would like to express my deepest gratitude to Sergio, who has been like the older brother I never had. Your guidance, support, and shared moments have been essential in helping me overcome the challenges I faced. Tiago, for whom I have deep gratitude and esteem, for his extreme competence, tirelessly accompanied by kindness and generosity. Besonderen Dank an meinen geduldigen Deutschlehrer Thomas. Danke für die Lacher vor der Kaffeemaschine und deine tolle Unterstützung. Many thanks to Julius, for all his unwavering support and patience during my test campaign, as well as his pleasant company. I would like to thank Matthias, who always came to my rescue whenever I encountered technical problems in the lab, and who is always ready to share a joke and a laugh. Thanks to my office mates, Jiangchao, with whom I shared the torments of experimental testing but also the joy of good pizza and noodles, and Larissa, who accompanied me in the early days at BAM when I was still inexperienced. I would also like to extend my deepest appreciation to Tatiana, who has been a constant advisor and confidant for me. Thanks to Sotiri for our philosophical chats. Gratitude to Keerthana for our sweet breaks at the vending machines and to Max, who has been a professional and human example. Finally, I sincerely thank all the colleagues not mentioned here who provided me with assistance and a warm welcome throughout these years.

A special thought goes to my family, who have always supported me, even during my moments of silence. I embarked on this journey with a light heart, knowing that I always had a safe haven to retreat to.
I would like to express my gratitude to all the friends who have made the distance between us feel insignificant. Bianca, for her indispensable constant presence, this achievement would not have been possible without her. Thank you for our endless phone calls. Mario, for his deep understanding of my wishes and aspirations, your support means the world. Finally thanks to Riccardo, without whom I would never have found the strength to start and complete this adventure. It is remarkable how our lives run in parallel, and yet we always manage to find each other.

Abbreviation

A	→ Strain at break
A_g	→ Uniform extension
AB	→ as-built
AM	→ Additive manufacturing
BD	→ Building direction
CT	→ Computed Tomography
DSC	→ Differential Scanning Calorimetry
EDM	→ Electric Discharge Machining
EDXRD	→ Energy-dispersive X-ray diffraction
F	→ Shape factor
GPD	→ generalized Pareto distribution
HAZ	→ Heat affected zone
HT	→ Heat treatment
HT1	→ heat treatment at 265°C for 1 hour
HT2	→ heat treatment at 300°C for 2 hours
HV	→ Vickers Hardness
LD	→ Longitudinal direction
ND	→ Neutron Diffraction
PBF-LB/M	→ Laser Powder Bed Fusion
POT	→ Peak-Over-Threshold
R_m	→ Ultimate Tensile Strength
$R_{p0,2}$	→ Yield Strength
ROM	→ Rule of Mixture
RS	→ Residual Stress
SXRD	→ Synchrotron X-ray diffraction
TD	→ Transversal direction
u	→ threshold value for the POT
XRD	→ X-Ray Diffraction

$\sqrt{area}$ → Murakami's parameter: root area of the defect
$\varepsilon_{\mathbf{el}}$ → Elastic strain
$\varepsilon_{\mathbf{pl}}$ → Plastic strain
Δa → crack extension
ΔK, SIF → Stress intensity Factor
$\Delta K_{\mathbf{th}}$ → Fatigue crack propagation threshold
$\Delta K_{\mathbf{th,eff}}$ → Fatigue crack propagation intrinsic threshold
$\Delta K_{\mathbf{th,op}}$ → Fatigue crack propagation extrinsic threshold
$\Delta K_{\mathbf{th,LC}}$ → Fatigue crack propagation long crack threshold
$\Delta\sigma$ → Stress range
$\Delta\sigma_{\mathbf{e}}$ → (Defect-free) fatigue limit
σ → scale parameter of the generalized Pareto distribution
$\sigma_{\mathbf{tens}}$ → Tensile stress
$\sigma_{\mathbf{comp}}$ → Compressive stress

1. Introduction

The Laser Powder Bed Fusion (PBF-LB/M) technology shows high potential in many industrial fields but, at the same time, it presents great challenges. The unique multi-scale microstructure, the presence of defects and residual stress are the main factors hindering its full exploitation. In particular, these aspects can play a crucial role in the fatigue durability of a component. It is therefore necessary to adapt the traditional approaches to include the complex thermal history that characterises the PBF-LB/M processes.

In this work the effects of thermal post-processing on microstructure and residual stress (RS) on the fatigue behaviour of an AlSi10Mg material are investigated. Due to the fundamental difference between the as-built and as-cast microstructure, an example of which is shown in Figure 1.1, a very different evolution during heat treatment has been observed [1, 2]. In particular, it is noticed that the nanometric PBF-LB/M microstructure, resulting from the extremely high heating and cooling rates occurring during the process, evolves at considerably lower temperatures and much faster than the coarser as-cast microstructure. In contrast to the cast material, where the spheroidization of the Si phase needs longer times and higher temperatures [3], in the PBF-LB/M material, significant changes in the microstructure can be induced already between 170 and 300°C [2, 4–6]. Therefore, the conventionally-adopted heat treatments (such as T6, consisting of solutioning above 500°C and ageing at about 180°C) are not originally conceived for PBF-LB/M parts and can result in inferior mechanical properties compared to conventionally processed parts. For this purpose, in this study two low temperature heat treatments (265°C for 1h and 300°C for 2h) are studied and compared to the as-built condition.

In parallel to a change in the microstructure, a modification in the residual stress state is generally observed. A multi-phase Al-Si-(Mg) alloy is in fact comparable to a composite material. In composites, a change in the morphology of the phases can lead to a relaxation or redistribution of residual stresses [7].

Although RS is considered one of the most influential factors affecting fatigue resistance, which results in an additional load on the component and can cause an unexpected failure, the topic is not fully addressed in the current literature, partly due to the lack of a well-established methodology for the calculation of RS in AM materials. Moreover, the

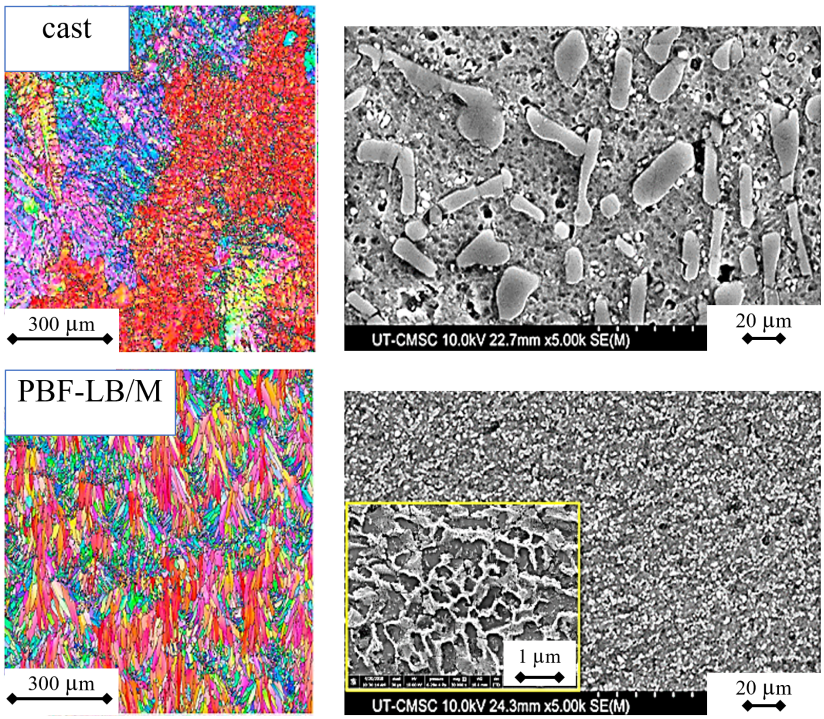

Figure 1.1.: Comparison between the as-cast and as-built microstructure of an Al-Si-Mg alloy [1].

published studies mainly focus on the surface RS state, whereas a lack of information on the bulk RS is pointed out. In addition, the impact of heat treatments on the RS state is scarcely studied in AlSi10Mg materials.

It is within the scope of this work to provide a comprehensive description of RS field in the PBF-LB/M material, combining various techniques such as laboratory x-rays diffraction (XRD) for the near-surface stress and synchrotron x-ray (SXRD) and neutron diffraction (ND) to investigate the bulk stresses.

The changes in the microstructure and RS state, induced by heat treatment, can have a beneficial or detrimental effect on the fatigue life of a component. Fatigue and fatigue crack growth properties are essential for load-bearing applications and are typically less studied in the literature than static properties. In this work, **the fatigue behaviour of the AlSi10Mg material and the effect of heat treatments on it are studied in depth. The**

High Cycle Fatigue (HCF) behaviour (S-N curve), as well as the fatigue short (cyclic R-curve) and long (da / d$N - \Delta K$ curve) crack growth behaviour are tested.
When residual stresses are high, they overshadow microstructural effects. However, when residual stresses are moderate the impact of the microstructure becomes dominant. In this respect, a competition between various types of defects can be observed: those that cause the highest stress concentration also control the fatigue behaviour. Frequently, in case of AM components, the controlling defect type will be surface roughness. However, when the surface is smoothed, manufacturing defects, such as gas porosity or lack of fusion, will dominate.

All these defects are usually narrow enough to approximate the mechanical characteristics of cracks. Furthermore, they generate local stress concentrations with a magnitude which depends on the defect size and morphology. Consequently, these defects act as crack initiation sites and can be treated as cracks. This allows the application of fracture mechanics concepts.
A preliminary investigation of the defect distribution by means of computed tomography (CT), combined with fracture mechanics approaches, can provide a valuable tool for fatigue assessment [8]. By means of statistical methods, e.g., the peak over threshold method, which is well suited for analysing data from CT scans, a prediction of the killer defects distribution can be estimated [9, 10].
Since defects play a fundamental role in the fatigue behaviour of an AM component, it is expected that taking them into account to establish fatigue assessment methods will be necessary. The aim of a defect tolerant assessment is the determination of the load carrying capacity of the AM components in the presence of defects. In this work, **the possible limitations of a fatigue design based on the S-N curve approach are investigated. Furthermore, different fracture mechanics approaches are applied: the Kitagawa-Takahashi diagram obtained by the El-Haddad model, the Murakami's $\sqrt{area}$ approach and the cyclic R-curve analysis, with the aim of showing their potentials.**

The work presented is composed as follows. In **Chapter 2** the state of the art on the microstructure, residual stress state and fatigue behaviour of a PBF-LB/M AlSi10Mg alloy will be presented, addressing in particular the research gaps present to date on the topic of thermal post-processing. **Chapter 3** details the manufacturing of the test specimens and presents the methods applied for the microstructure and monotonic mechanical properties characterisation, the diffraction based determination of the residual stress state and the fatigue testing. Furthermore, the fracture mechanics concepts and models are introduced. The results of the microstructural characterisation by microscopy and x-ray

micro-computed tomography are given in **Chapter 4**. The extreme values statistics is applied to evaluate the defect distribution. A comprehensive description of the residual stress is presented. The comparison of various diffraction techniques is aimed at developing a reliable methodology to evaluate the residual stress state in a PBF-LB/M component. The influence of the microstructural and residual stress results on the short and long fatigue crack propagation are showed in **Chapter 5**, focusing on the near-threshold regime. The S-N curves of the material are provided in **Chapter 6**. The test results on two batches of materials with very different defectology show a high influence of defect size on fatigue life and provide a good test case for fracture mechanics approaches. The experimental results are re-elaborated through fracture mechanics concepts, aiming at providing a method for fatigue life prediction suitable for an AM material. Finally, the concluding remarks are presented in **Chapter 7**.

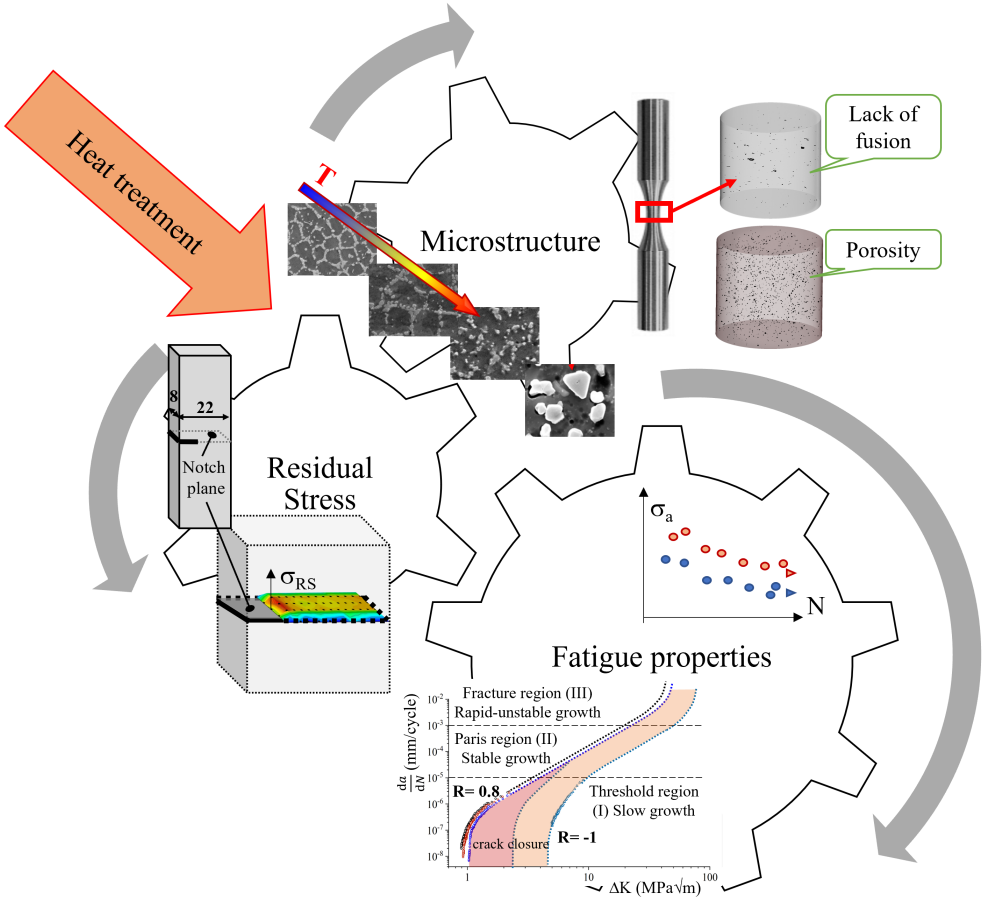

Figure 1.2.: Schematic of the project topics: study of the influence of heat treatments on the microstructure and residual stress and the corresponding impact of these changes on the fatigue life.

2. State of the art

2.1. Laser Powder Bed Fusion (PBF-LB/M) Additive Manufacturing (AM) of Al-Si-Mg alloys

Additive manufacturing (AM) is reaching a well-established position in the production of high-performance components. Among the AM techniques, Laser Powder Bed Fusion (PBF-LB/M) processes allow the building of metallic components from 3D models in a layer-by-layer manner, reducing the post-processing and the consequent waste of material. A near net-shape complex component can be produced, minimizing the use of expensive subtractive tools. Therefore, great efforts have been undertaken to improve various aspect of the production technique including the technological metallurgical and design aspect. This enabled the PBF-LB process to evolve from a rapid prototyping technique to an established industrial reality [11–14].
PBF-LB/M is applied in the production of camseveral engineering alloys such as steel, titanium, nickel, and aluminium systems. The processability of aluminium alloys usually present issues such as high reflectivity and thermal conductivity, strong oxidation tendency, and wide solidification range [15]. To address these limitations, a whole new body of research is now focused on the development of Al alloys tailored for PBF-LB/M.
Up to date, the most popular aluminium alloys processed by AM are the eutectic Al-Si and the hardenable Al-Si-Mg alloys [16]. Alloying Si to aluminium lowers the melting point, minimizing the required energy to melt the metal powder allowing a tighter dimensional control for manufacturing complicated shapes and overhang structures. It improves weldability and fatigue performances, provides excellent corrosion resistance, and the ductility of the alloy can be modified and improved after heat treatment. Due to their attractive combination of mechanical properties, high heat conductivity, low weight and price, the Al-Si alloys found a large number of applications in the automotive, aerospace and domestic industries. Alloying Mg can significantly enhance mechanical strength and impact performances through solution heat treatment and ageing, without compromising other desirable mechanical performance aspects. These improvements are largely due the formation of β" Mg_2Si precipitates, a strengthening phase for the Al matrix [5, 17].

The PBF-LB/M technique is particularly interesting as it offers advantages over the well-established casting processes. PBF-LB/M AlSi10Mg materials possess, in the as-built condition, increased mechanical strength compared to the cast Al-Si due to the formation of finer nano-silicon networks and smaller grains.
As the process is based on the localised melting of small powder volumes by a high-energy source, it presents a number of peculiarities:

- Extremely high cooling rates (10^3–10^7 K/s)
- Formation of strongly supersaturated solid solutions
- Solidification of new melt pools overlapped with each other, due to the layer-by-layer construction
- Successive heating and cooling cycles on previously solidified material

This leads to:

- Generation of high magnitude residual stress
- Epitaxial growth: directional solidification and mechanical anisotropy
- In-situ heat treatment of previously solidified material: local phase transformations and precipitation

Considering the complexity of the topic, further investigations are even now required.

2.2. Post-processing of Al-Si-Mg alloys produced by Laser Powder Bed Fusion

Unique thermal cycles occur during the PBF-LB/M process with extremely rapid heating and cooling rates and with simultaneous melting of the top powder layer and re-melting of previously solidified layers [18]. These characteristic processing conditions lead to a very fine but inhomogeneous microstructure and to the build-up of significant residual stress (RS). For this reason heat treatments are commonly applied to the components before qualifying it for service.

2.2.1. Understanding the microstructure evolution during heating: Differential Scanning Calorimetry

At the beginning of the project, a lack of understanding regarding how such a unique microstructure could be exploited for achieving enhanced fatigue performance was emphasized, which reflected on the choice of not optimal thermal post-processing of PBF-LB/M parts. Heat treatments traditionally performed on cast alloys, such as T6, had been blindly transferred to the PBF-LB/M components. Considering the fundamental difference between the as-built and as-cast microstructure, their evolution during heat treatment can not be similar [2, 4–6]. Therefore, the conventionally-adopted heat treatments are often not optimal for PBF-LB/M parts and can result in inferior mechanical properties compared to conventionally processed parts. The research for optimised treatments contributes to the spread and progress in the use of AM materials. For this purpose, differential scanning calorimetry (DSC) analysis can highlight the temperatures at which modifications in the microstructure occur, revealing which are the most promising temperatures for post-processing. DSC is a thermal analysis method that measures the heat evolution from a sample under controlled temperature programs. It can identify solid state transformations such as precipitation, homogenisation, and recrystallisation. When a physical transformation occurs, the heat flux is affected. Several authors recorded two peaks during a DSC analysis [4–6]. The thermograms are characterised by the presence of two exothermic peaks: peak A, lying at approximately 260°C, and peak B at 320°C. An example from *Yang et al. 2018*, recorded with a constant heating rate of 20°C/min, is shown in Figure 2.1. During DSC, the microstructure evolution is monitored while the temperature is increasing. For this reason, the recorded peak temperatures need to be adapted for heat treatments, where the temperature is reached and held constant over time. It was assessed that the transformations occur at temperatures of 265°C and 295°C during isothermal heating [4]. Different authors interpreted the cause of these peaks yielding contradictory conclusions. In summary, the most accepted version is that the peak A should be attributed to Si precipitation from the supersaturated matrix and the peak B to the superposition of two effects: Mg_2Si formation and Si diffusion along the eutectic network. More in detail, the microstructure undergoes during heating the evolution summarised in Figure 2.1. The very fine microstructure, consisting of α-aluminium small grains preferentially solidifying along the <100>crystal direction towards the centre of the melt pool [19]. The sub-micron Al grains are decorated by a nanometric silicon phase (with a diamond crystal structure) and enclosed by an almost continuous eutectic silicon (Si) network. Part of the Si (ca. 2.7 wt%) and Mg (0.5 wt%) atoms is in a supersaturated solid solution in the aluminium matrix, thus exceeding the maximum Si equilibrium solubility (1.65 wt%) at the eutectic temperature [2, 20]. It follows that in the as-built

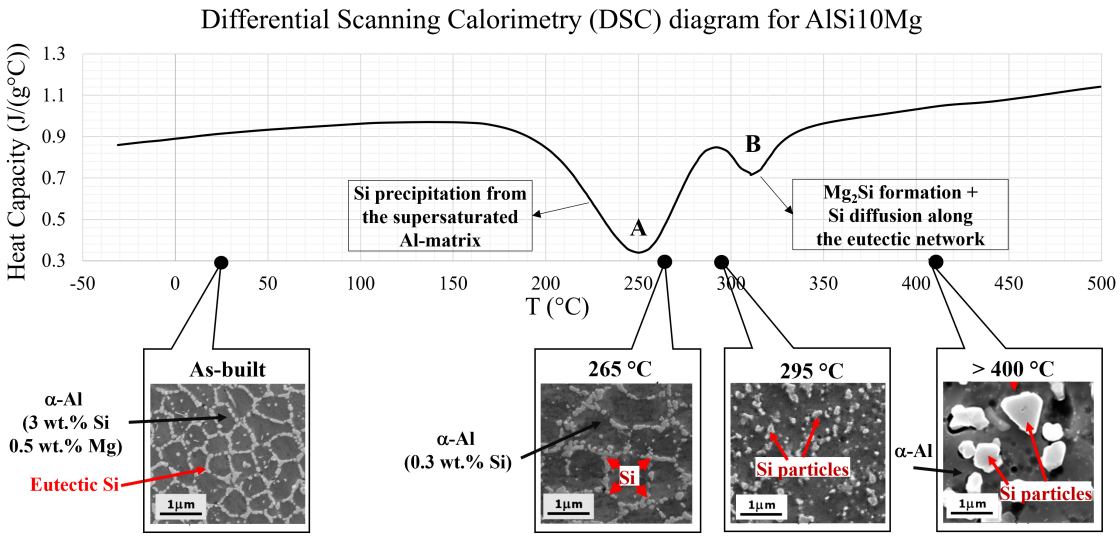

Figure 2.1.: Differential Scanning Calorimetry thermograph for an AlSi10Mg sample at a heating rate of 20°C/min under flowing nitrogen (data from [5]). The corresponding changes in microstructure are shown with SEM micrographs.

condition, a significant fraction of silicon is contained within the aluminium lattice. This fine dispersion leads to high hardness, ultimate tensile strength and elongation at fracture, higher or at least comparable to the cast AlSi10Mg material [16]. At temperatures above 265°C, ultrafine needle-like and cubic-like Si precipitates grow in the primary Al cell, while the eutectic network structure is still retained [2, 4, 11, 21, 22]. After 1 hour at 265°C, the process is almost completed, and the Si precipitated from the supersaturated matrix (supersaturation: 0.3 wt% Si) [2].

After reaching 300°C, the metastable as-built microstructure evolves towards a more stable condition with the formation of globulized Si particles through the disintegration of the Al/Si eutectic network [4, 11, 21]. The mesostructure (i.e., at the scale length of the layers) homogenises partially after heat treating at 300°C, as the melting pool boundaries are still noticeable in certain regions [2]. In support of this observation, *Mfusi* observed an isotropic response of the material after performing a heat treatment at 300°C for 2 hours [23].

Heat treating at temperatures higher than 450°C (the so-called T5) further coarsens (Ostwald ripening) the Si particles, creating a unimodal size distribution with average

particle size of $\tilde{2}$ μm. At these temperatures the mesostructure is completely homogenized: the melt pool boundaries are vanished [24]. Iron needle-shaped β intermetallics are formed [21, 25].
Also, temperatures above 450°C lead to the thermically induced growth of porosity [26]. Ageing at temperatures in the range between 160 and 180°C after solutionizing at temperatures above 500°C (the so-called T6 heat treatment) induces precipitation strengthening by the formation of Mg_2Si particles [2]. This heat treatment was originally optimised for conventionally cast Al-Si-Mg alloys and was then extended to the AM components. Nowadays T6 is still the most investigated scheme in the literature [27–32], nevertheless, by solutioning at >450°C the advantage of a finely dispersed Si particles is lost. In this regard, a direct ageing heat treatment on the as-built microstructure combines the potential of the fine as-built AlSi10Mg microstructure with Mg_2Si precipitation [2, 33, 34]. Nevertheless, this strategy is only possible when the platform pre-heating is below $\tilde{1}$50°C, which, in turn, increases the possibility of part distortion induced by residual stress [35]. Hot platform processing (as is the current study, with 200°C pre-heating) lead to a significant loss of the aging response. A long holding times at high temperature during processing could induce a substantial overaged microstructure [34].

2.3. Defect formation in Al-Si-Mg alloys produced by Laser Powder Bed Fusion

A further critical aspect in PBF-LB/M processes is the formation of voids and defects during manufacture. Two types of defects are mainly observed: lack of fusion and porosity [36]. A lack of fusion is the incomplete melting of the powder layer due to insufficient energy input or improper fusion among layers or hatches caused by a lack of overlap. Porosity includes metallurgical pores, which originate either from the absorption of the surrounding gas (N, O or H), or from the evaporation of certain alloying elements (e.g., Mg), and parameter based pores, which are mainly the result of a process fault. For example, the common keyhole pores are porosity generated when the laser power is excessive to cause evaporation of metal [37]. Hot Isostatic Pressing (HIP) is frequently adopted for PBF-LB/M components as a solution to this issue, to increase the density of the samples.

2.4. Residual stress state in Al-Si-Mg alloys produced by Laser Powder Bed Fusion

2.4.1. Process-induced residual stress state in PBF-LB/M AlSi10Mg

During AM processes, the irradiated material experiences large temperature fluctuations in a short time which causes the build-up of thermal stresses [38]. Two descriptive models are used to explain the mechanism of thermal stresses formation in PBF-LB: the Temperature Gradient Mechanism (TGM) model and the cool-down phase model [39].
In the TGM model, during the process, solid material is irradiated and heated up by the laser. As a result, in the laser spot size, the material tends to expand as shown in Figure 2.2(a). The thermal expansion (named $\varepsilon_{\mathbf{th}}$) is constrained by the surrounding colder material, generating a compressive stress/strain state in the irradiated zone. As illustrated in Figure 2.2(c-d), the compressive strain has an elastic component ($\varepsilon_{\mathbf{el}}$) and, if the compressive stress exceeds the compressive yield stress ($\sigma_{\mathbf{y}}$), a plastic one ($\varepsilon_{\mathbf{pl}}$) is generated. Thereafter, the laser beam leaves that area and the irradiated zone cools and tends to shrink. The shrinkage is partially inhibited as a consequence of the plastic deformation developed during heating, yielding a residual tensile stress ($\sigma_{\mathbf{tens}}$) condition. To respect the force equilibrium of the part, a zone of compressive stress ($\sigma_{\mathbf{comp}}$) must surround the irradiated zone.
Secondly, the cool-down phase model describes the formation of residual stresses as the previously molten material re-solidifies and shrinks back to a solid state. The shrinkage is partially inhibited by the underlying solidified layers, thus introducing tensile stresses in the added upper layer.
These RS distributions, if not evaluated and accounted for, can prove highly deleterious to the fatigue resistance of components. The RS state can add to the load remotely applied on the component, resulting in an unexpected failure. However, this also implies that with a suitable post-processing, harmful RS can be removed or even beneficial RS can be functionally introduced [40]. Thereby, for a the safe in-service operation of PBF-LB/M components, understanding the RS state is of extreme importance.

2.4.2. Classification of residual stress

Commonly, three types of residual stress are defined according to the length scale in which they act and selfequilibrate:

1. **Type I (σ_I, macrostress)** acts over a component-size length scale. It usually appears during thermal and/or mechanical processing of the material when plastic strain

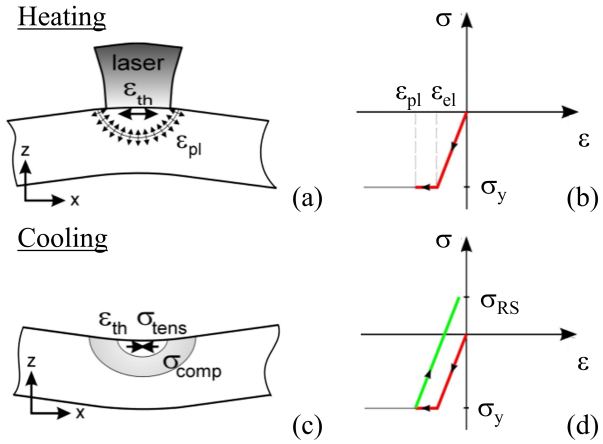

Figure 2.2.: Description of the TGM model: (a) Induced strain during laser heating and (b) simplified representation of the thermal elastic and plastic strain formation in the irradiated zone. (c) Induced deformation during the cool down and (d) simplified representation of the residual stresses formation. Adaption from *Kruth et al.* [38, 39].

gradients are introduced (e.g. shot-peening, bending). Macrostress can be relieved by heat treatment or plastic deformation. Macrostresses balance throughout the component.

2. **Type II (σ_{II}, microstress)** acts in the microstructure length scale (grain sizes). It is caused by inhomogeneities in the microstructure, e.g. thermal/elastic mismatch between phases or crystallographic texture. It is an intrinsic characteristic of polycrystalline materials, due to the intrinsic anisotropy of crystalline structures.

3. **Type III (σ_{III}, microstress)** acts at the smallest scale, the scale of inter-atomic distances, and is caused by intergranular defects inside the crystal (i.e., dislocations or vacancies).

2.4.3. Optimisation of the PBF-LB/M process parameters for reducing detrimental residual stress

Extensive research has been dedicated in recent years to optimise the process parameters (such as scan strategy, preheating temperature and contour strategy) to reduce the build-up of detrimental RS and to improve the mechanical properties in AM materials and in

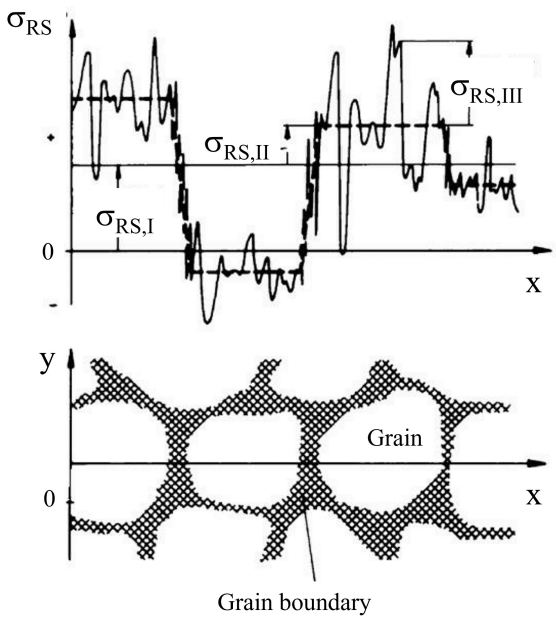

Figure 2.3.: Classification and length scale of the residual stress. Figure adapted from *Bertuzzi et al.* [41]

aluminium alloys. The focus of this paragraph is to summarise the studies aimed at the evaluation and a subsequent mitigation of RS in PBF-LB/M AlSi10Mg alloys [33, 34, 42–46].

One of the parameters influencing the build-up of RS is the preheating temperature of the baseplate: a higher building platform temperature leads to lower RS magnitudes by reducing the severity of the process thermal gradients. It has been reported that maintaining the build platform at 200°C induces a negligible RS level [33, 43]. *Zhao et al.* [47] measured a strong reduction in the RS with increasing temperature: in samples manufactured with a building platform temperature of 35°C the measured RS range is about 90 MPa, while at 200°C the RS are reduced to below 15 MPa. This is reported to happen also in the bulk, since the authors applied the compliance method for the RS measurements. With this technique, a stress profile is measured on a plane at a selected height. Thus, the technique allows the analysis of bulk RS, but it is destructive to the part [48]. In addition, *Marola et al.* [46] investigated the influence of the baseplate temperature on RS combining the traditional XRD technique with Raman spectroscopy. The Raman spectroscopy allowed to measure the type II micro-stress acting on the fine

Si phase, showing that larger eutectic particles undergo lower stress with respect to nanometric precipitates. The macro-stress acting on the Al matrix was determined by XRD. It was observed that maintaining the building platform at 100 °C leads to a minor reduction in RS compared to 200 °C. Hence, in order to induce a meaningful mitigation of RS, the pre-heating of the baseplate needs to be set at least at 150°C.
Moreover, at a fixed preheating temperature, a chessboard strategy induces lower RS than a parallel stripe scanning strategy [45]. The length of individual scan lines is shorter during the chess-board scanning, reducing the build-up of RS [49]. This strategy is suggested in particular for large components.
Beevers et al. studied the influence of the so-called contour layer. Samples manufactured without contour exhibit larger compressive RS at the surface in the load direction. This, combined with the presence of smaller near-surface defects and a lower roughness after vibratory polishing, contribute to an improvement of the fatigue performances in specimens produced without contour [44].
In Table 2.1, the as-built RS magnitudes reported in literature for PBF-LB/M AlSi10Mg are summarised. The measured RS has a strong dependence on the component geometry, scan strategy, as well as-built platform temperature.

Almost the entirety of the authors measured the RS on AM AlSi10Mg by laboratory X-ray diffraction (XRD). On aluminium alloy, the penetration depth with this technique is about 10 μm beneath the surface, i.e., only surface RS are investigated.
Differently, *Salmi et al.* [52] performed hole drilling and investigated a stress depth profile up to 1 mm under the surface. This study focused on the effect of placing support structures between the sample and the platform. Tensile RS are observed in the thickness analysed in the two conditions. However, the sample produced with the supports shows higher RS magnitudes than those measured in the sample that was directly in contact with the platform, with values up to 100 MPa.

2.4.4. Mitigation of residual stress via heat treatments

Post-process heat treatments provide a strategy to tailor the RS state in order to improve the component resistance.
Nevertheless, not many studies address the effect of specific heat treatments on residual stresses. The T6 heat treatment is commonly ascribed to completely relieve the RSs [53]. The effect of low temperature heat treatments on RS is not yet fully understood. Some studies are published about the effect of HT on the surface RS [20, 50–52, 54]. The results from *Colombo et al.* [51] indicate that heat treatments above 245°C led to a relaxation and redistribution of surface RS. These results are supported by *Van Cauwenbergh* [54],

Table 2.1.: Summary of RS measurements on PBF-LB/M AlSi10Mg from literature.

Authors	$T_{platform}$ (°C)	Geometry	Scan strategy	Building direction	Surface condition	Method	RS range: max - min (MPa)
[44]	165	Stripes, rotation vector 67°	Hourglass	A	vibratory polishing, no contour	XRD	-140 ÷ -80 (Z direction)
					vibratory polishing, with contour		-50 ÷ -10 (Z direction)
[40]	80	Chessboard, rotation vector 67°	Prism	C	as-built	XRD	20 ÷ 120 (X direction)
		Stripes, rotation vector 67°					40 ÷ 140 (X direction)
	120	Chessboard, rotation vector 67°					0 ÷ 90 (X direction)
	160	Chessboard, rotation vector 67°					-5 ÷ 50 (X direction)
[48]	35	Stripes, rotation vector 67°	Prism	A	as-built	Compliance	-40 ÷ 50 (X direction)
	200						-7 ÷ 5 (X direction)
[50]	200	Chessboard, rotation vector 45°	Cylinder	A	as-built	XRD	-5 ÷ 25 (Z direction)
[51]	150		Prism	B	as-built	XRD	70 ÷ 120 (Z direction)
				A			50 ÷ 110 (X direction)

Building direction: (A) 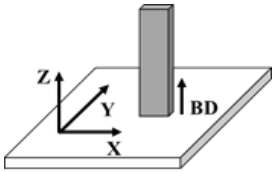

(B) 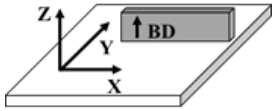

(C) 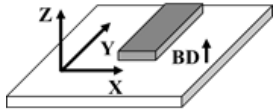

who reports a reduction in RS of 60-65% already after a direct ageing (170°C/6h). Heat treatments at higher temperatures (270°C/2h and 300°C/2h) do not provide a further stress relief. The value is obtained by the cantilever method, which gives a stress integrated on a plane in a cantilever beam-shaped sample. Another investigation from *Zhou et al.* [55] shows that a HT at 300°C for 2h is effective for removing RS. The stress-relief HT reduced the compressive RS at the surface to a 10% from an initial value of around 100 MPa. Moreover, some authors report that heat treatments at temperatures below 300°C may be more advantageous for the removal of RS, maintaining a relatively high strength thanks to the interconnected Si structure [4].
In conclusion, the bulk and near-surface RS state of PBF-LB AlSi10Mg after post-processing heat treatment are not currently addressed in detail in the open literature. A deeper investigation of the topic is in the aim of this work.

2.5. Mechanical properties of Al-Si-Mg alloys produced by Laser Powder Bed Fusion

2.5.1. Quasi-static mechanical properties of PBF-LB/M AlSi10Mg alloys

The metallurgy of Al-Si alloys produced by PBF-LB/M is characterised by the presence of the fine cellular eutectic network, which strongly influences the mechanical behaviour of the material. Static mechanical properties have been widely studied in the literature [12, 15, 27, 28, 31, 42, 56–77]. The unique as-built fine microstructure leads to high hardness, ultimate tensile strength ($R_{\mathbf{m}}$) and yield strength ($R_{\mathbf{p0.2}}$), generally higher than the cast alloy [16]. Nevertheless, the resulting mechanical behaviour is anisotropic: if the loading direction is parallel to the building direction, the elongation is comparable to that of the cast material, while, if perpendicular, the elongation at fracture is almost 2% higher [76]. In Figure 2.4, the quasi-static tensile properties of the material in different post-process conditions are summarised using the results obtained by *Van Cauwenbergh et al.* and *Li et al.* [54, 59]. When no baseplate preheating is applied during the production, a direct ageing heat treatment at 170°C for 6 hours increases the elastic moduli and the yield strength ($R_{\mathbf{p0.2}}$), whereas the $R_{\mathbf{m}}$ remains constant. The elongation at fracture is halved. After 2 hours at 270°C the elastic modulus is unchanged, but the material shows an important decrease in strength (-18%) for the benefit of an increased elongation at fracture (+50%). Heat treating at 300°C leads to an additional loss of strength (-33%) in favour of an improved elongation at fracture (+100%) (Figure 2.4b). A preheating temperature of 200°C is shown to significantly reduce the strength already in the as-build condition. The low temperature heat treatments are compared with a solution heat treatment (so-called

T5) at 550°C for 2 hours and with the conventional T6 heat treatment (2 hours at 550°C followed by ageing at 180°C for 12 hours). In this case the strength reduction is greater than 50% and the elongation at break increases by 150%.

The Si-rich continuous eutectic network is deemed to act as the main load-bearing

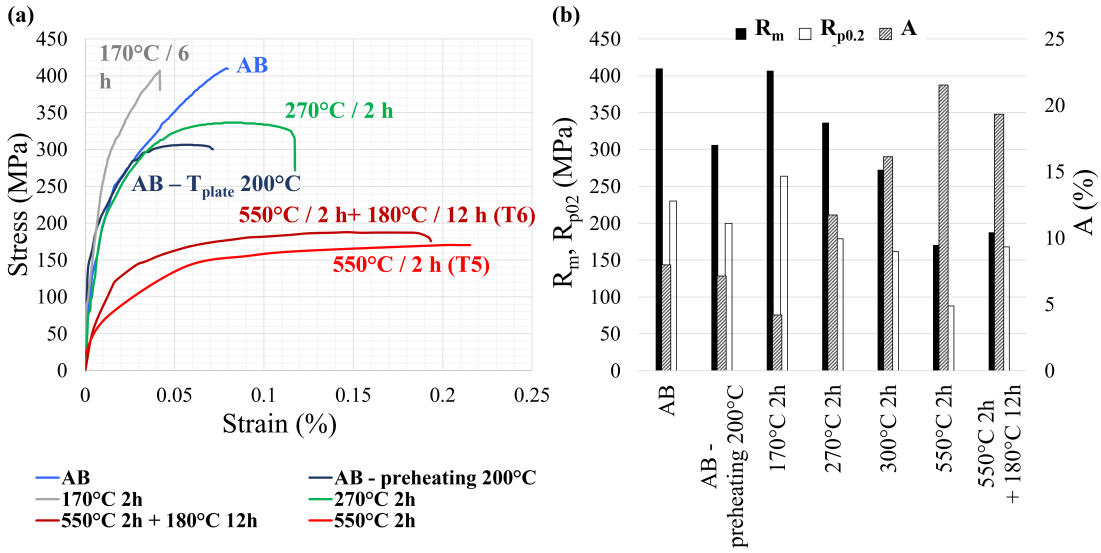

Figure 2.4.: Summary of quasi-static tensile properties of PBF-LB/M AlSi10Mg by *Van Cauwenbergh et al.* [54]

structure and being a barrier for dislocation movement [78]. Therefore, a significant strain hardening effect is observed for the conditions which exhibit a continuous Si-rich eutectic network. Moreover, the Si supersaturation in the as-built state contributes to a solid solution-strengthening effect.

It is reported that the Si phase morphology and size are the most impacting microstructural features affecting the mechanical properties [25, 59]. After the spheroidisation of the Si-rich eutectic network induced by HT, a significant strength loss and a notable increase in ductility is measured. Moreover, T5 causes more significant segregation of Si from the supersatured aluminium matrix and the formation of silicon particles with larger size which lead to the highest increase of the elongation at failure. The ductility increases with increasing temperature (i.e., increasing Si particles) at the expense of reducing yield strength and ultimate tensile strength [23, 24, 30]. Finally, mechanical features are no longer influenced by the building orientation as a result of the micro- and mesostructure

homogenization [21].
From this condition of enhanced ductility, a further ageing (T6) allows the mechanical strength to be improved.
Nonetheless, it must be noted that the best mechanical strength can be obtained (when the preheating temperature is kept under 150°C), with a direct ageing on the as-built microstructure [2, 33].

2.5.2. Fatigue properties of PBF-LB/M AlSi10Mg alloys

While the static mechanical properties have been widely investigated and optimised, fatigue design and assessment of AM metallic components is still a relevant open issue. The fatigue life of a component is heavily influenced by the microstructural features. The characteristic inhomogeneity of the material properties over the component volume, the presence of defects such as porosity and lack of fusion, a pronounced surface roughness in the as-built state and the already discussed high residual stress are challenging problems to assess, as their individual contribution to the results cannot be easily deconvoluted. [79].

High Cycle Fatigue (HCF)

The key parameter governing fatigue life is defects. Fracture analyses from tested specimens prove that cracks nucleate either from surface or subsurface defects. The defect position plays an important role: the surface or subsurface ones are far more detrimental than the internal ones [9, 80]. Surface polishing enables the enhancement of fatigue properties when avoiding the presence of subsurface defects continually emerging on the surface during the polishing process [81]. Moreover, if near-surface defects with a size comparable or larger than the peak-to-valley roughness are present, polishing will not lead to an improved fatigue response: the fatigue resistance will be comparable to the one of samples with as-manufactured surfaces [82, 83].
Process optimisation to achieve a lower defect content is the key to increasing fatigue life. To this end, many studies have been published on varying process parameters [9, 84, 85]. Notwithstanding, at the actual state of the technology, it is not possible to produce defect-free AM components. In fact, changing the laser parameters and adopting complex post-treatments (e.g., hot isostatic pressing) help reduce their number and size, although it is never possible to completely eliminate porosity [75, 77]. In addition, a post-processing usually loses the advantages of AM, as it requires additional expenditure of resources and time, thus the benefit of having a ready-to-use component immediately after production is lost. *Hirata et al.* [77] studied the increase in fatigue strength as relative density increases. A considerable improvement was found, in particular when the relative density exceeds

98.7%. From this level on, each increase in density significantly increases the fatigue resistance.
Post-process heat treatments introducing a modification of the Si structure have an effect on the fatigue performances. Many studies have been published, in particular on the T6 [28, 84–87], showing, for the most part, a beneficial effect of heat treatment [81, 83, 88, 89]. With regard to this aspect, it is noted that the influence of microstructure is likely to be limited: the main factor governing fatigue strength are defects depending on size, number and location. Moreover, if the defect size is larger than the grain size, especially in the case of ductile materials, which are typically less sensitive to impurities, the fatigue limit is not significantly affected by the microstructure [90]. In other words, the effect of the microstructure on the fatigue life is only visible in defect-free materials.
The build orientation of AM parts can generate anisotropic structural response. This is attributed to microstructure (i.e., grain morphology and crystallographic orientation) and defect directionality (i.e., distinct dimensions of the void in different planes) [90]. *Brandl et al.* [28] and *Domfang et al.* [85] proved higher fatigue strength for horizontal-built specimens.
The experimental results discussed above are summarised in a S-N diagram in Figure 2.5. The large scatter present results from different test conditions as well as the plethora of different process/post-process parameters and surface fishing. Some of the principal parameters, giving rise to the observed wide scatter, are listed in the following table (Table 2.2).

Fatigue crack propagation

Defects in AM materials such as porosity, lack of fusion and inclusions cause strain concentration and act as crack initiation sites [91]. In this, AM differs from flawless materials, in which fatigue damage starts with the accumulation of local plastic deformation. The crack nucleation stage is found to be short, even suppressed, and the major part of the lifetime is usually spent at the stages of micro and short crack growth [92]. In the first stage, the crack size is still of the order of microstructural features (e.g., grain size) and the plastic zone ahead of its tip is completely embedded within a single or a few grains. As consequence the role of local microstructure heavily influences the crack growth [90, 93]. These so called *microstructurally short cracks* arrest at microstructural barriers, e.g., grain boundaries.
If not arrested, the crack will grow to a length comparable to the extension of the plastic zone (hence denoted as *mechanically short crack*). When the crack extension Δa increases, another arrest mechanism is activated: the crack closure. By this stage the crack is defined

Table 2.2.: Details on the process and test parameters for the High and Very High Cycle Fatigue results from PBF-LB/M AlSi10Mg literature reported in Figure 2.5.

Authors [ref.]	Stress ratio, R	frequency, f (Hz)	Power Laser, P (W)	Plate temperature (°C)	Scanning speed (m/s)	Spot size (µm)	Hatch spacing (µm)	Layer thickness (µm)
Brandl et al. 2012 [28]	0.1 / axial	ca. 108	250	300	0.5	200	150	50
Maskery et al. 2015 [86]	0.1 / axial	30	200	180	0.57	70	130	25
Alboukhair et al. 2016 [87]	0.1 / axial	30	200	180	0.57	70	80	25
Nasab et al. 2019 [82]	0.1 / axial	30	340	160	1.3		200	30
Romano et al. 2017 [9]	-1 / axial	30	1000 W/1000 W/50 J/mm-1	200/200/165		90		60/60/30
Zhang et al. 2018 [88]	-1 / axial	15	490		2		100	40
Domfang et al. 2019 [29]	-1 / axial	80		150/200				
Tridello et al. 2019 [89]	-1 / axial	20k	350	150	1.15	80	170	50
Kempf et al. 2021 [30]	-1 / rotating bending	60	770/35/950	150/150/200	2.26/1.65/2.45		170/130/180	50/30/60
Hirata et al. 2022 [77]	-1 / rotating bending	52.5	300	35	1.2	100	150	30
Mower et al. 2016 [81]	-1 / rotating bending	20-25	100	200	0.93	100		50
Uzan et al. 2017 [83]	-1 / rotating bending	50	400	30	1	100-150	200	60

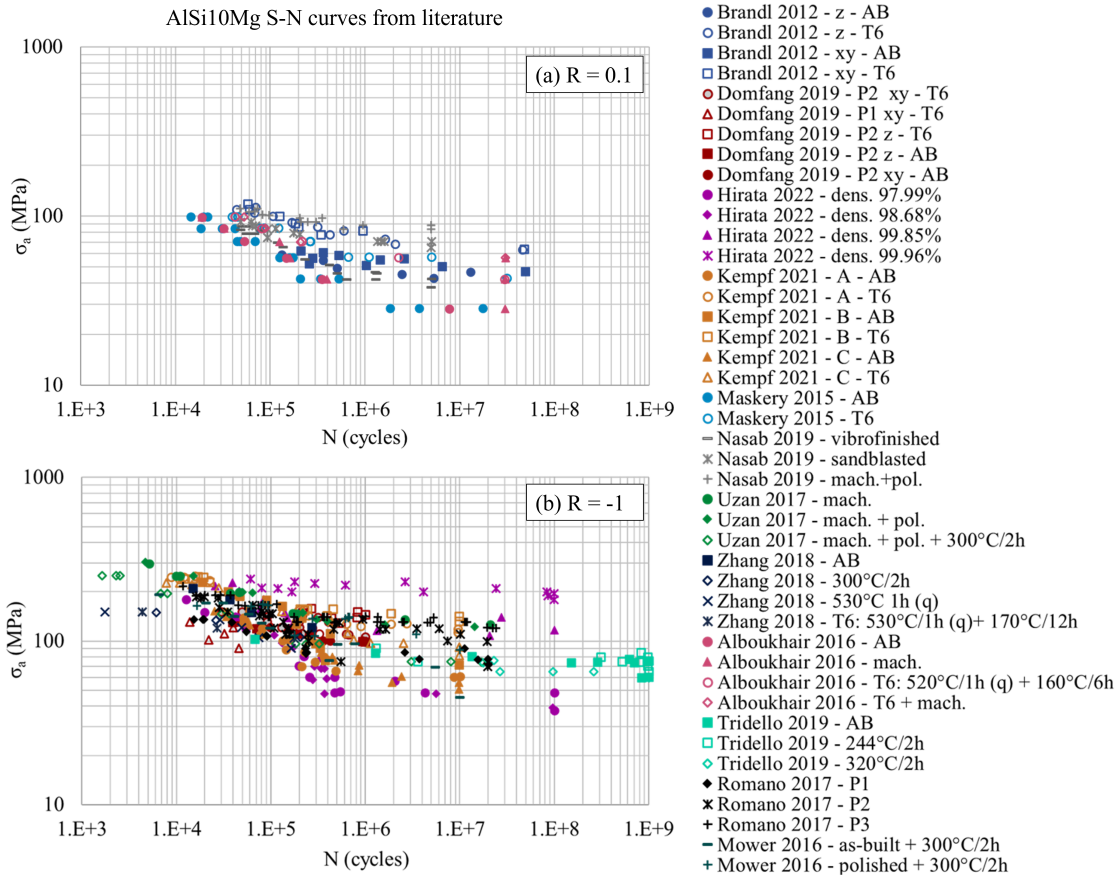

Figure 2.5.: S-N curves summary from the literature: experimental results of HCF and VHCF tests performed on PBF-LB/M AlSi10Mg at stress ratio R equal to (a) 0.1 [28, 82, 86, 87] and (b) -1 [9, 29, 30, 77, 81, 83, 88, 89].

as *physically short*.

Crack closure is a phenomenon whereby, even when an external opening load is applied, crack flanks remain in contact [94]. This premature contact is due to the presence of an obstacle such as might result from plastic deformation, asperities, oxide debris or metal particles [95, 96].

With increasing crack length the crack closure phenomenon builds up gradually to an extent where the crack closure effect stabilizes and a stationary, crack length independent state is reached: the *long crack* propagation stage [91, 93].

The fatigue crack growth threshold $\Delta K_{\mathbf{th}}$ is defined as the asymptotic value of the stress intensity factor range ΔK at which the fatigue crack growth rate da/dN approaches zero [97, 98]. When ΔK falls below the fatigue crack propagation threshold $\Delta K_{\mathbf{th}}$, crack arrest happens.
The fatigue crack propagation threshold $\Delta K_{\mathbf{th}}$, for physically short cracks is a function of the crack extension Δa [99]. The crack size dependency of $\Delta K_{\mathbf{th}}$ is designated as "cyclic R-curve" [96]. Following initiation, small cracks are observed to grow at stress intensities below the long-crack threshold; some propagate with decaying growth rates until arrest, while others propagate quite rapidly to merge with the long-crack behaviour [100]. Various mechanisms are responsible for the variation in the threshold. *Ritchie* [101] divided them in intrinsic mechanisms, that determine the inherent resistance of a material against fatigue crack propagation, and extrinsic mechanisms, that cause a reduction in crack driving force at the crack tip [102]. Therefore, in the threshold value ΔK_{th} two components can be distinguished: an intrinsic threshold, $\Delta K_{th,eff}$, that is a material parameter and a crack closure or extrinsic component, $\Delta K_{th,op}$, dependent on parameters such as the load ratio, the roughness of the crack faces and the crack length.

$$\Delta K_{\mathbf{th}} = \Delta K_{\mathbf{th,eff}} + \Delta K_{\mathbf{th,op}} \tag{2.1}$$

Influence of residual stress on the fatigue resistance Type I and II (macroscopic and intergranular) RS can also have an influence in the crack closure phenomena. RS can cause a shift in the mean stress (and stress ratio R) to higher (in the case of tensile) and lower (in the case of compressive) values. As a consequence, the extrinsic component $\Delta K_{\mathbf{th,op}}$ is shifted to greater or lower values, respectively. In other words: compressive residual stresses increase $\Delta K_{\mathbf{th}}$ because they can contribute to crack arrest [79]. The fatigue resistance can be improved by post-process heat treatments.

In PBF-LB/M AlSi10Mg, heat treatments significantly impact on the microstructure and residual stresses, starting already at low temperature. In the literature, the Si spheroidisation is reported to decelerate fatigue crack propagation [103–105]. The overall response is significantly more ductile due to a more homogeneous distribution of plastic strain in the alloy with a globular Si microstructure [104].
So far, the fatigue long crack growth behaviour of the AlSi10Mg aluminium alloy was studied by *Di Giovanni et al.* [106] and *Santos Macías et al.* [107]. The authors investigated the influence of different building and notch orientations and the beneficial effect of a 300°C and a T6 heat treatment. The results are summarised in Figure 2.6. In the AB condition, the response appears to be strongly dependent on the building orientation,

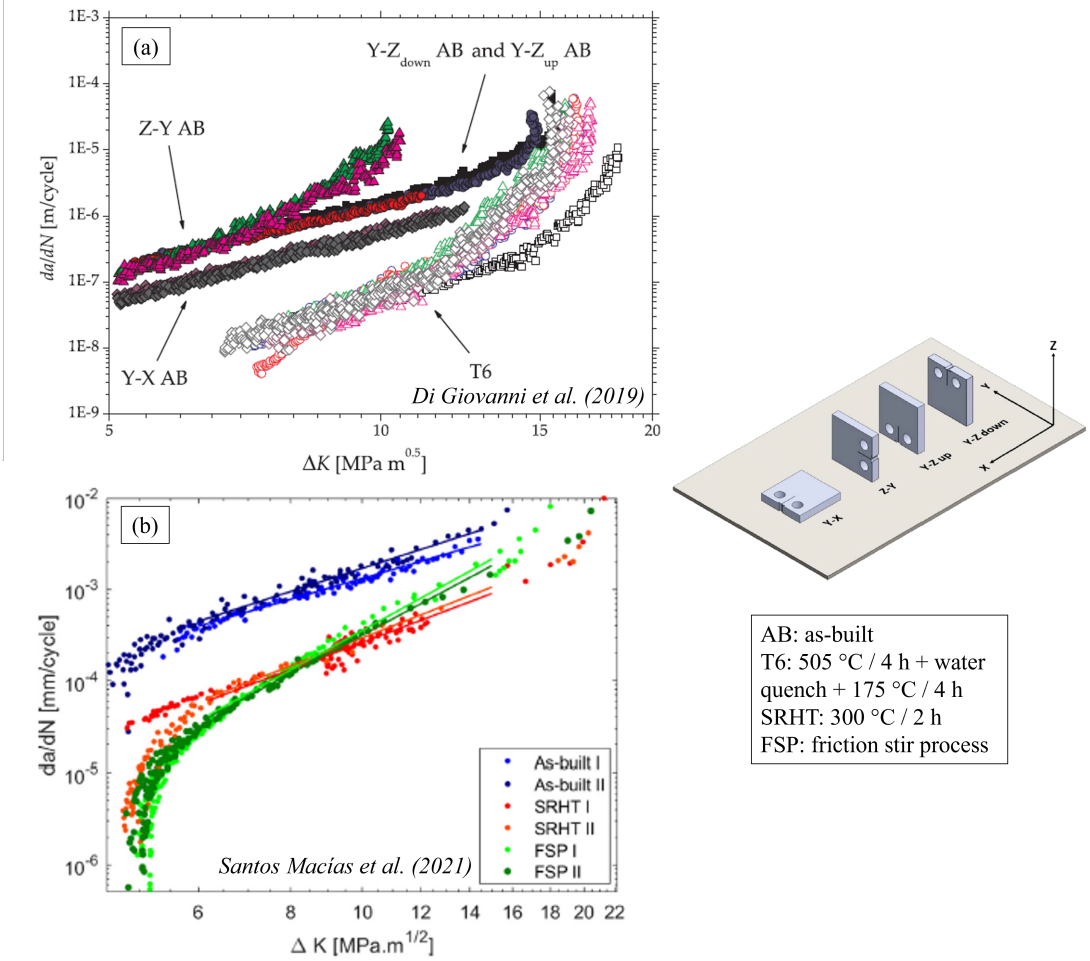

Figure 2.6.: Experimental da/dN-ΔK curves of PBF-LB/M AlSi10Mg specimens at R=0.1 (a) with different building directions and notch positions (Y-X, Z-Y, Y-Z_{down}, Y-Z_{up} planes) in the as-built and T6 conditions [106] (b) in a Z-Y orientation for the as-built, heat treated at 300°C for 2 hours (SRTH) and after friction stir process (FSP) [107].

with the best resistance for the Y-X condition, and the worst for the Z-Y condition. In the Z-Y oriented samples, cracks can easily propagate along the weakest link, namely the heat

affected zone (HAZ) along the interlayer boundary, whilst, in the Y-X, the crack has to cross more fatigue resistant intra-layer regions with an associated higher energy consumption. The HAZs between adjacent melt pools are the weakest link in the material as they present finely distributed Si particles around the α-Al grains which are the preferential site for crack initiation and propagation. Cracks propagating along planes oriented perpendicular to the layers therefore encounter more resistance than they do when propagating parallel to the layers, as in the latter case they can easily move along the weak HAZs. After a T6-heat treatment (solution at 505°C for 4h and ageing at 175°C for 4h), the homogenised microstructure minimizes the dependence of crack growth rate on crack orientation with respect to the building direction. The coarsening of the microstructure into larger homogeneously distributed particles enhances the fatigue resistance as the crack is forced to propagate across the pure α-Al regions strength by the Mg_2Si precipitation. [106]
The fatigue crack growth rate is decreased by an order of magnitude after the friction stir process and the heat treatment at 300°C for 2 hours. An increased crack branching is observed, which is deemed to reduce the crack growth rate. [107].

3. Materials and Methods

3.1. AlSi10Mg samples production by Laser Powder Bed Fusion

The investigated samples were produced using a Concept Laser M2 machine at the German Aerospace Research Center (Deutsches Zentrum für Luft- und Raumfahrt e.V., DLR), Germany. The samples were built in the shapes of prisms and cylinders (Figure 3.1b-c) in two batches using gas atomised AlSi10Mg powder under argon atmosphere. The scan strategy consisted of 5×5 mm^2 squares manufactured using a 45° rotating scan vectors, as shown in Figure 3.1d. The longest edge of the sample (height, 112 mm) is parallel to the building direction (BD). A laser power of 380 W with a scanning speed of 1500 mm/s was adopted. The layers had a 30 μm thickness and the hatching distance was 100 μm. The outer contours were scanned after the bulk with a standard contour strategy using a single scan with a laser power of 180 W and scanning velocity of 1600 mm/s. The samples were built on a platform which was kept at 200°C during the entire process.

In addition to the as-built (AB) condition, considering the analyses discussed in the

Table 3.1.: Summary of the process parameters.

PBF-LB/M machine	Power (W)	Hatch space (mm)	Scan speed (m/s)	Layer thickness (μm)	Building platform temperature (°C)	Atmosphere
Concept Laser M5	380	0.1	1.5	30	200	Argon

Chapter 2.2.1, two low-temperature heat treatment at 265°C for 1 hour (HT1) and at 300°C for 2 hours (HT2) were performed in a PEO-630 furnace, followed by air cooling with a cooling rate of 10°C /min. More details about the furnace are given in Appendix A. To avoid any distortion, the samples were machined to the final shape after HT.

High Cycle Fatigue (HCF) and Low Cycle Fatigue (LCF) specimens

According to the geometric tolerances in the standard for High (ASTM E466-15 [108] / ISO 1099 [109]) and Low (ISO 12106 [110] / ASTM E606 [111]) Cycle Fatigue, the

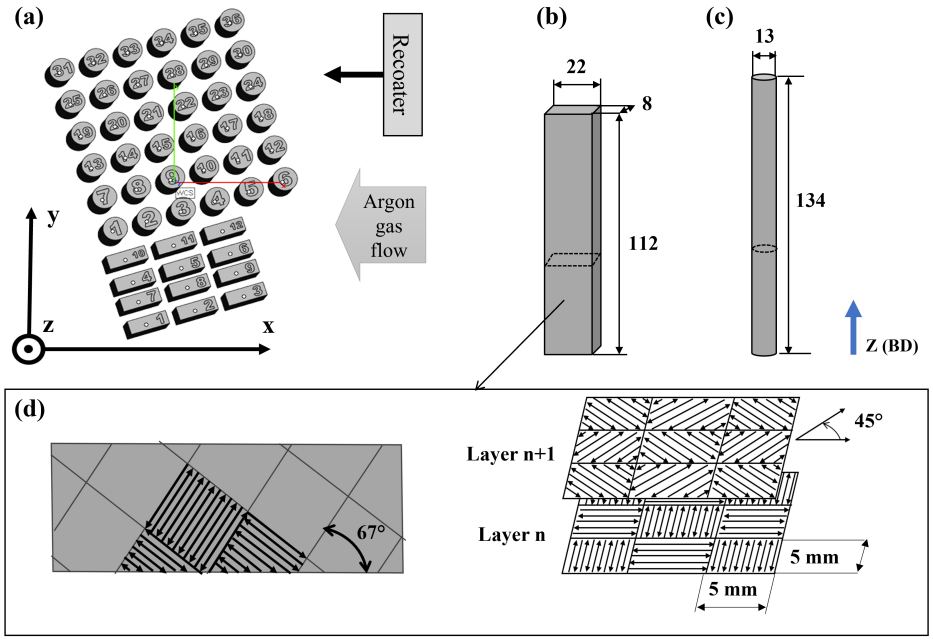

Figure 3.1.: Sample production: (a) Positioning on the platform within the PBF-LB/M chamber; schematic illustration of as-built AlSi10Mg (b) prism and (c) cylinder geometries shown in mm; and (d) scanning strategy.

cylindrical specimens were machined to the shape shown in Figure 3.2. The samples were produced in 2 different batches of 36 pieces each. Before HCF testing, the specimen gauge length was polished to a surface roughness R_z lower than 0.2 μm. The polishing was carried out adapting a lathe, where the mandrel is replaced by a pad on which abrasive diamond paste can be applied. The following procedure was adopted: 45μm-diamond paste for 30 min, 25μm-paste for 30 min and 12μm-paste for 45 min.

Crack propagation SENB specimens

Rectangular 22×8×112 mm^3 (width × thickness × height) prisms were printed and subsequently machined to a Single Edge Notch Bending (SENB) shape (Figure 3.3) according to ISO12108 [98]. All the measured and tested specimens were produced within a single batch (namely batch 1, 12 samples in total). A notch with a depth of 5 mm and a width of 0.2 mm was machined by electric discharge machining (EDM). The initial

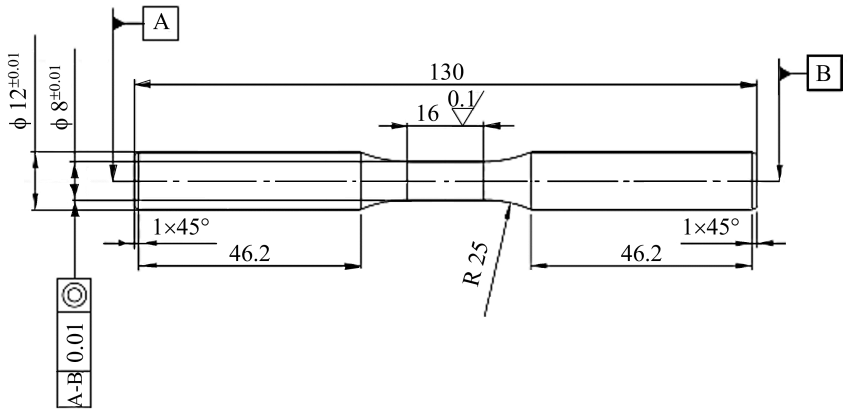

Figure 3.2.: Technical drawing of the High and Low Cycle Fatigue specimen

compression precracking has to be performed at the lowest possible value of the cyclic stress intensity factor ΔK to limit the extension of the cyclic plastic zone ahead of the crack-tip at the end of this stage. This condition allows reliable values to be obtained when determining the cyclic R-curves. For this, a very sharp notch root radius is required, which can be obtained by using a commercial razor blade made of stainless steel to further sharpen the EDM notch. An additional depth of $\approx$ 150µm is obtained with this process. Material abrasion is facilitated by interposing a 3μm-diamond polishing compound in a lubricating solution between the blade and the EDM notch. The notch tip radii provided with this procedure is in the range of 10 to 20 μm. An example of the obtained notch is provided in Figure 3.3.

3.2. Microstructure and mechanical properties characterization

The effects of the heat treatment on the microstructure were investigated using a Scanning Electron Microscope (FEG-SEM) LEO 1530VP (Zeiss, Germany), operated under an acceleration voltage of 20 kV and a probe current of 7-8 μA in high pressure mode. The secondary electron (SE) imaging mode was used.
Crystallographic information about the grain orientation and size was also acquired using Electron Backscattering Diffraction (EBSD). The EBSD data were acquired with an ESPRIT 1.94 (Bruker Nano) system using a Bruker e-FlashHR detector. Data analysis was performed using the Oxford Instruments HKL Channel 5 software [112], as well as the

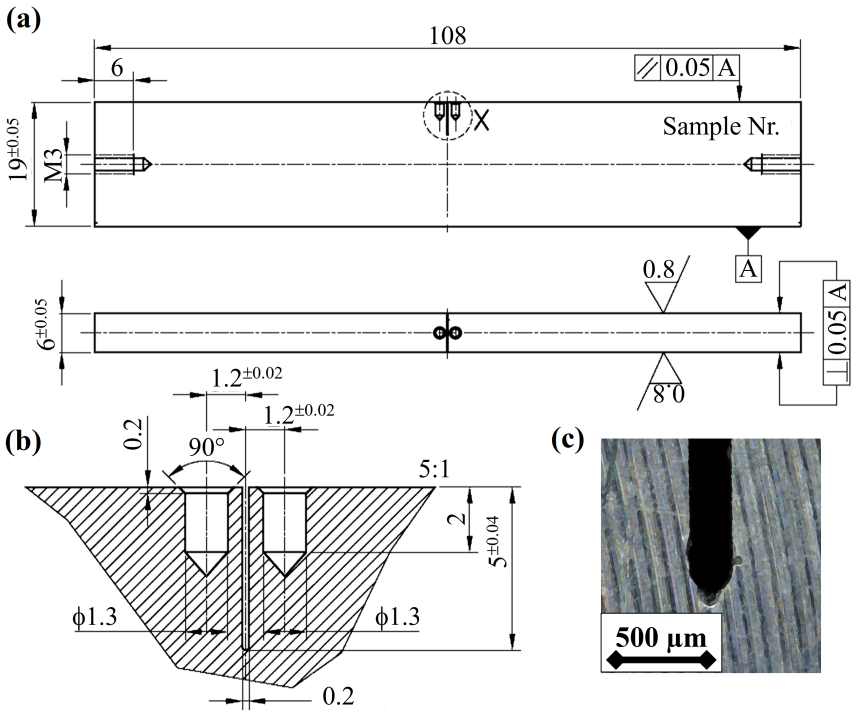

Figure 3.3.: (a) technical drawing of the Single Edge Notch Bending specimen, in mm; (b) detail of the notch; (c) optical microscope image of the sharp notch obtained with the razor blade.

MTEX Matlab toolkit [113].
A Keyence VHX-2000 digital microscope with a Z50 lens was used to acquire the fractograms of the fracture surfaces after testing.
The metallurgic preparation included three initial polishing steps with silicon carbide abrasive grinding papers (1200, 2400 and 4000 grit), followed by a 3 µm diamond slurry on a polishing cloth, and a final step with a 0.02 µm colloidal silica suspension. To increase the contrast between the aluminium matrix and the silicon network, a final etching step was carried out using a Dix & Keller solution (190 ml H_2O; 5 ml HNO_3; 10 ml HCl; 2 ml HF) for 15 min.

The defect distribution was investigated using micro computed tomography (μCT). The tomograph was developed in-house at the Bundesanstalt für Materialforschung und -

prüfung (BAM, Berlin, Germany); it features a Microfocus X-ray tube XWT-225-SE from X-Ray WorX GmbH (30827 Garbsen, Germany), with a focal spot of 6 μm and a maximum voltage of 225 kV, and a XRD1620 detector from PerkinElmer Inc. (Waltham, MA, USA) with a CsI scintillator of 2048$\times$2048-pixel. The source-detector distance was fixed to 1170 mm. The voxel size obtained for a 6 mm thick SENB specimen was (8 μm)^3. The software VGstudio MAX 3.0 from Volume Graphics, Heidelberg, Germany [114], was used to visualize and analyse the CT data.

Tensile tests were performed on three specimens per condition (AB, HT1 and HT2), tested in accordance with DIN EN ISO 6892-1 standard [115] at room temperature with a strain rate of 0.11 mm/s. Although for AM components it would be suggested to increase the number of specimens to a minimum of 6, the test of 3 specimens is sufficient for the purpose of this work, i.e. to give a qualitative evaluation of the effect of heat treatment on the quasi-static properties of the material.

The Vickers hardness was determined on one specimen per condition according to ISO 6507-1:2018 [116]. The samples were previously polished with SiC sandpaper up to 2500 grit. Furthermore, Keysight Nanoindentor G200 system equipped with a diamond Berkovich pyramid mounted into a XP measurement head was used for nanohardness measurements. An ExpressTest was performed: the hardness was mapped by 10000 indents on a 100$\times$100 µm array, with 1 μm pitch. The samples were previously grinded with a 1200 grit abrasive paper and polished.

The fracture surface roughness was measured by a μSurf expert Optical 3D microscope by NanoFocus AG, Oberhausen, Germany. The confocal microscope comprised an LED light source focused through a multi-pinhole disc, a rotating multi-pinhole disc, an objective 800XS lens with a piezo drive and a CCD camera. This lens allows a resolution of 8 nm in the vertical direction. Each acquired image is a horizontal slice through the topography of the sample. Capturing the images at different focal heights produces a stack of such images. The three-dimensional height image is reconstructed from the stack of confocal images by the software μsoft analysis premium 8.0.9173 [117].

3.3. Residual stress characterization by diffraction methods

Diffraction based measurements of residual stress (RS) are based on the constructive interference generated in the interaction of waves with a crystalline material. This condition

is mathematically described by the Bragg's law:

$$n\lambda = 2d_{hkl}\sin\theta \tag{3.1}$$

where λ is the wavelength of an incident beam, θ is the scattering angle, *n* the order of interference and d_{hkl} the lattice spacing of the analysed crystal. The Miller indices, *hkl*, denote the family of parallel lattice planes in the crystal lattice. If the wavelength of a monochromatic photon or neutron beam and its diffraction angle are measured, the lattice spacing can be determined by applying the Bragg's law.

The principle underlying RS determination through diffraction methods consists of the

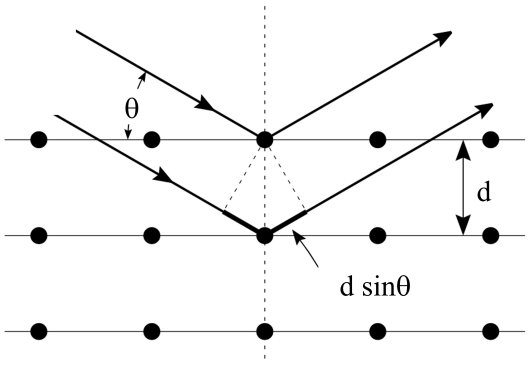

Figure 3.4.: Schematics of the Bragg's law. Incident waves on a crystal lattice at angle θ are partially reflected by successive parallel crystal planes of spacing . The superposed reflected waves interfere constructively if the Bragg condition is satisfied.

fact that, when a material undergoes a tensile or compressive stress, this results in a deformation of the crystal lattice or, in other words, in a change in d_{hkl}.

Both X-rays and neutrons can be used to study RS as they have wavelengths of the other of the interplanar spacing of the most common engineering materials. In this work, the residual stress state was investigated in a non-destructive manner by neutron diffraction (ND), laboratory (XRD) and synchrotron X-ray diffraction (SXRD).

Synchrotron X-rays, called "hard" X-rays, have energies in the range 10 to 120 keV. Because of their higher energies, hard X-rays penetrate deeper into matter than soft (laboratory) X-rays, those with energies below 10 keV. Therefore, laboratory X-rays are limited to measure the surface stresses (the penetration depth is about 10 μm in the case of aluminium alloys), while neutrons and synchrotron X-rays can reach the material bulk.

The wavelength of a photon is given by the equation:

$$\lambda = \frac{hc}{E} \tag{3.2}$$

where h is the Plank's constant, c the speed of light in vacuum and E is the energy of the photon. While the wavelength of the neutron follows the equation:

$$\lambda = \frac{h}{m_n \nu} \tag{3.3}$$

with m_n mass and ν velocity of the neutron.
When the interplanar spacing of the unstressed material $d_{hkl,0}$ is known, the strain on a measured component can be calculated using the relationship:

$$\varepsilon = \frac{d_{hkl} - d_{hkl,0}}{d_{hkl,0}} \tag{3.4}$$

Considering these equations, when using diffraction techniques, the strain can be calculated by keeping a fixed wavelength and determining the peak shift in terms of Bragg's angle θ (angle dispersive diffraction) or, at a fixed diffraction angle, by determining the peak shift in the photon energy spectrum (energy-dispersive diffraction).
Measuring the strain in three perpendicular directions, denoted by *i,j,k*, the stress can be calculated applying the Hooke's law:

$$\sigma_i = \frac{E}{1+\nu}\varepsilon_i + \frac{E\nu}{(1+\nu)(1-2\nu)}(\varepsilon_i + \varepsilon_j + \varepsilon_k) \tag{3.5}$$

The elastic constants, E and ν were calculated using the Kröner model for the Al {311} and Si {311} reflection [118]. The selection of Al {311} and Si {311} is based on the fact that this peak is least affected by intergranular strain (ISO-21432 [119]). The constants are summarised in Table 3.2. Two configurations, elucidated in Figure 3.5,

Table 3.2.: Summary of the elastic constants used for the stresses calculation of the Al {311} and the Si {220} and {311}.

Elastic property/Diffraction Peak	Al {311}	Si {220}	{311}
E (MPa)	69 390	167 350	159 160
ν(/)	0.35	0.22	0.23

were adopted for the measurements: (a) reflection and (b) transmission geometries. In

the reflection geometry the detector is arranged on the same side (with respect to the measured specimen) as the source and the beam penetrate a portion of material referred to in Figure 3.5a as $D_{\mathbf{refl}}$. In transmission mode the beam passes through the entire thickness of the specimen ($D_{\mathbf{trans}}$) and is detected by the detector on the opposite side.

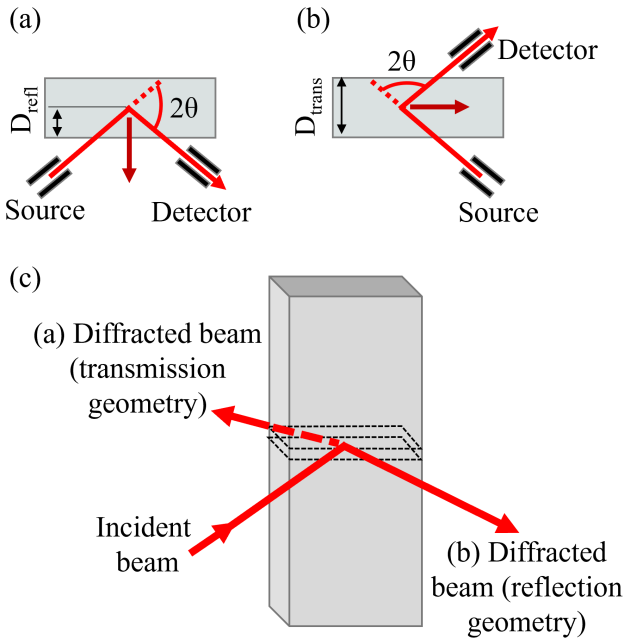

Figure 3.5.: Schematics of the (a) reflection and (b) transmission geometries used for the RS measurements.

3.3.1. Laboratory Energy Dispersive X-rays

The subsurface RS state was determined by energy-dispersive X-ray diffraction (EDXRD) at the X-ray Corelab, Helmholtz-Zentrum Berlin für Materialien und Energie (HZB), Berlin [120]. The X-ray Corelab laboratory is equipped with a liquid-metal-jet X-ray source, which allows a greater penetration depth compared to the common laboratory diffractometer, up to 500 μm in a lightweight aluminium alloy. Continuous polychromatic X-ray radiation of up to 160 keV is generated by Bremsstrahlung. In the reflection geometry, residual stress depth profiles in the near-surface region: up to some hundred micrometres can be obtained. The results shown in this study refer to the Al {311} peak, associated to

a penetration depth of about 350 μm. The measurements were performed with a 1 mm pinhole polycapillary and a constant diffraction angle of $2\theta = 16.6$. The measurement time per point was 5 min. For the energy dispersive case, Bragg's law can be rewritten using Equation 3.2. By substituting such relation in Equation 3.4 and Equation 3.1, the lattice spacing can be obtained from the energy as follows:

$$d_{hkl} = \frac{6.199}{\sin\theta}\frac{1}{E_{hkl}} \tag{3.6}$$

The $\sin^2\psi$ method was then utilized for RS determination, assuming a biaxial stress condition as RS are measured at the near surface (the stress component normal to the free surface is assumed to be negligible). The method is based on the linearity relation between the lattice spacing and the $\sin^2\psi$, where ψ defines the orientation of the sample surface. Precisely, ψ is the angle between the normal of the surface and the incident and diffracted beam bisector, which is also the angle between the normal to the diffracting lattice planes and the sample surface. The $\sin^2\psi$ method offers the advantage of not requiring a stress-free reference for strain calculations but can be used only in the reflection geometry.

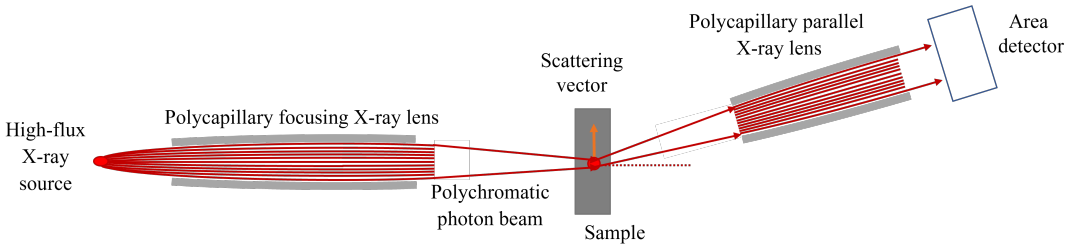

Figure 3.6.: Schematics of the X-ray Corelab set-up for EDXRD.

3.3.2. Neutron Diffraction

Bulk RS can be measured by means of neutron diffraction (ND). The measurements were performed at the Strain Analyser for Large Scale engineering Applications (SALSA) instrument at the Institute Laue-Langevin (ILL), France [121]. Schematics of the set-up are shown in Figure 3.7. The reflection and transmission geometries were used. The instrument uses a monochromatic beam and a Position Sensitive Detector (PSD) at a distance of 1 m from the sample. Using a neutron wavelength of approximately λ = 1.66 Å, the Al {311} diffraction peak (located at circa 2θ = 85.6°) was utilized for strain measurement. The counting time per point was 5 min.

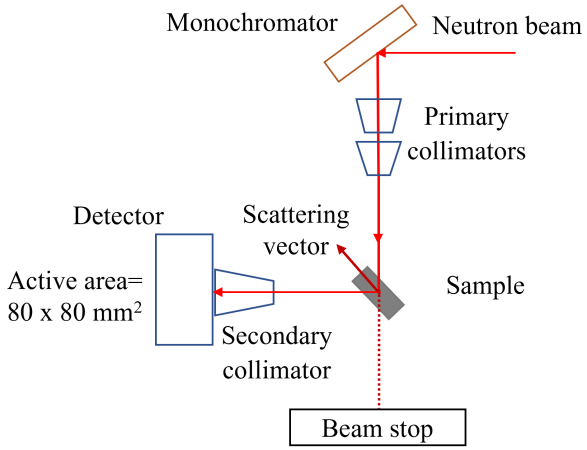

Figure 3.7.: Schematics of ILL-SALSA set-up for ND.

3.3.3. Synchrotron X-ray Diffraction

Synchrotron X-ray diffraction (SXRD) was performed at the high resolution powder diffraction beamline ID22 at the European Synchrotron Radiation Facility (ESRF), France [122]. Schematics of the set-up are shown in Figure 3.8. The experiment was performed with a monochromatic beam at 60 keV in transmission mode and with a single channel analyser crystal detector set-up. With a wavelength of about $\lambda = 0.207$ Å, in addition to the Al {311} diffraction peak (located at $\approx 2\theta = 9.7°$), the {220} and the {311} Si peaks (at $\approx 6.2°$ and 7.2°, respectively) were resolved. The Al {311} and Si {311} were selected for strains calculation, as these peaks are the least affected by intergranular strain [119]. An

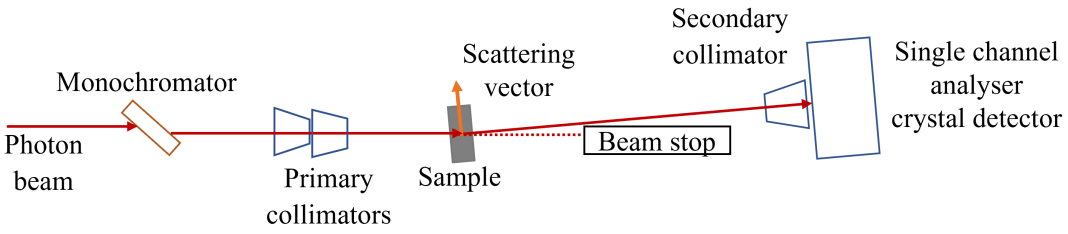

Figure 3.8.: Schematics of ESRF-ID22 set-up for SXRD.

approximation of the global stress σ_{TOT} is obtained applying the rule of mixture (ROM) considering the Al-Si alloy as a metal matrix composite:

$$\sigma_{\mathrm{TOT}} = f\sigma_f + (1-f)\sigma_m \tag{3.7}$$

where f is the Si volume fraction (≈10%), E_f is the Si elastic modulus and E_m the aluminium matrix elastic modulus.

3.3.4. Measured points and optics arrangement

The RS state was investigated at the subsurface and within the bulk of three SENB specimens, in the as-built, HT1 and HT2 conditions, respectively. The bulk RS were analysed by means of ND and SXRD, while the subsurface was investigated with laboratory EDXRD.

ND allowed to measure the strains in the three principal directions defined by the prism

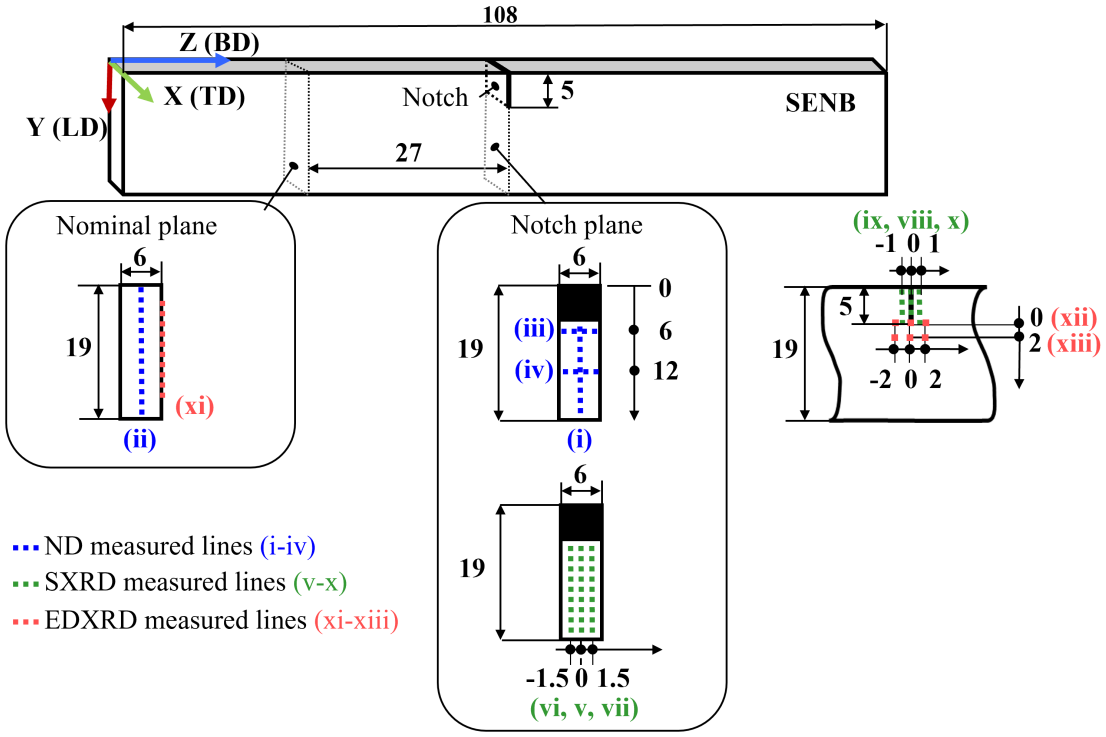

Figure 3.9.: Schematic of the measured lines on SENB specimens.

geometry: building direction (BD), transversal direction (TD) and longitudinal direction (LD) in the as-built and HT1 conditions. The lines scanned are shown in Figure 3.9 in blue: (i) a line at the notch plane, where the stress field is affected by the notch, and (ii) a line far from the influence of the notch, at a distance from the notch plane of 27 mm (namely nominal plane). The variation through the 6 mm thickness (corresponding to TD) was also investigated at the notch plane on two lines: (iii) 1 mm ahead of the notch tip, to consider the influence of the notch, and (iv) 7 mm ahead the notch tip, where the stress field is assumed to be unaffected by the notch and the free surface. Along lines (i) and (ii) (Figure 3.9a) strains were measured with pitches of 0.5 mm near the notch (for 1 mm length) and 1 mm over the remaining length. The counting time per point was 5 min. A clarifying scheme of the optics arrangement is provided in Figure 3.10. A gauge volume of $0.6\times2\times2$ mm^3 was used for the measurements of BD and the TD. To maintain the same spatial resolution, the optics were rotated by 90° (obtaining a gauge volume of $2\times0.6\times0.6$ mm^3) for the measurements along the longitudinal component (LD). The use of an elongated gauge volume in the BD was assumed appropriate as the residual stress is not expected to exhibit strong gradients along this direction over the measured length scale. The $2\times0.6\times0.6$ mm^3 gauge volume and a pitch of 1 mm was used for the through-thickness measurements, lines (iii) and (iv) (Figure 3.10b). In this configuration the gauge volume diagonal in the TD direction was approximately 0.85 mm.
Importantly, line (i) was measured also across the notch for the determination of a free-stress reference (see Section 3.3.5 below); in this case, the gauge volumes (A, B) included the notch and part of the material, as shown in the inset in Figure 3.10.
In SXRD the diffraction angles are usually considerably lower than for ND, e.g. for the Al {311} reflection 2θ is ≈10° for SXRD and ≈90° for ND. For this reason, the measurement of stresses in three directions is often hindered by the geometry of the specimen, i.e. in one direction the dimension of the object is sufficiently large to completely attenuate the beam. In the present case, due to the plate geometry of the SENB specimen (height=108 mm), the measurement of TD via SXRD is not practicable. Therefore, SXRD is limited to biaxal measurements. This implies the assumption of a plane stress condition ($\sigma_{TD} = 0$) to calculate the stresses from the measured strains. Considering the thin-walled geometry of the SENB specimens (6 mm thickness), this hypothesis is considered valid. The accuracy of this assumption can also be assessed with the results obtained by ND triaxial measurements.
The strains were measured by SXRD in the BD and LD along a central line (v) in the notch plane (note that (v) is coincident with line (i) measured by ND) and on two lines at 1.5 mm from the lateral surfaces: (vi) and (vii). The gauge volume is schematised in Figure 3.11. A 0.225×2 mm^2 beam is used, providing a though thickness gauge length of ∼3mm

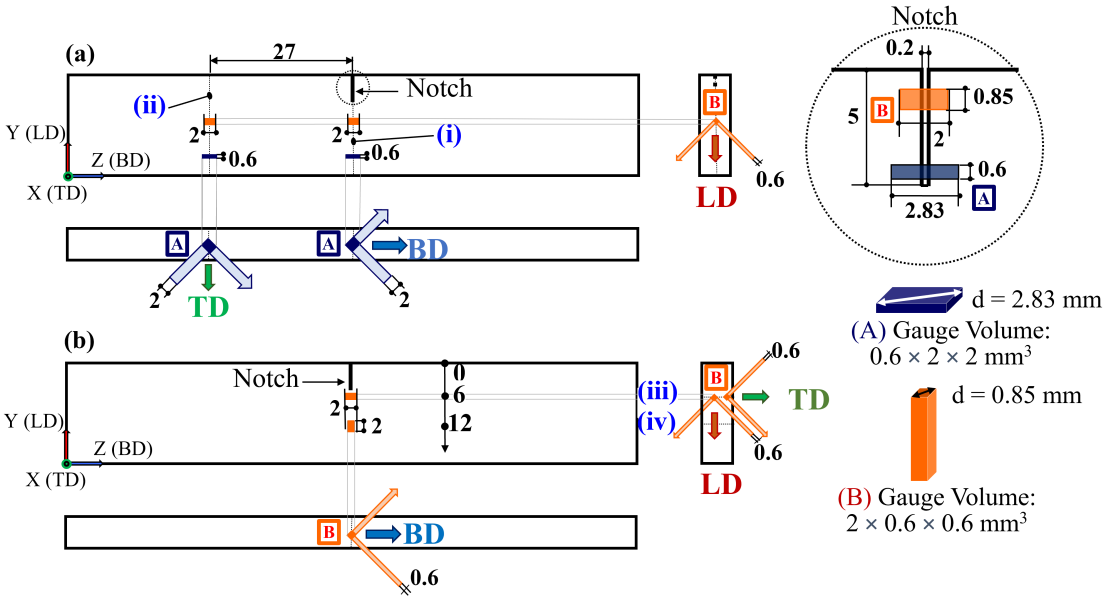

Figure 3.10.: Schematics of the two configurations adopted for the ND measurements on SENB specimens. Two different gauge volumes were used: (A) $0.6 \times 2 \times 2$ mm^3 and (B) $2 \times 0.6 \times 0.6$ mm^3. (a) For scan lines (i) and (ii) the gauge volume (A) was used for the BD and TD, afterwards the primary optic was rotated by 90° (gauge volume (B)) to measure LD. Line (i) was measured also across the notch for the determination of the free-stress reference (the gauge volumes (A, B) included the notch and part of material as shown in the inset). (b) For lines (iii) and (iv) the gauge volume (B) was used for all three directions.

As in the case of ND, a line (viii) (shown in Figure 3.10) was measured across the notch for the determination of the free-stress reference. The gauge volume shape in the two measured directions, BD and LD, is shown in a simplified representation in the detail (A) in Figure 3.11. To assess the stress variation within the gauge volume, which extends ≈2 mm in the BD when the LD component is measured (see again Figure 3.11, detail (A)), two lines, above (x) and below (ix) the notch were measured.

Finally, the near-surface RS were investigated by EDXRD on the lateral surface of the specimens around the notch tip on six points (line (xii) and (xiii)) and on a line (xi) at 27 mm from the notch plane.

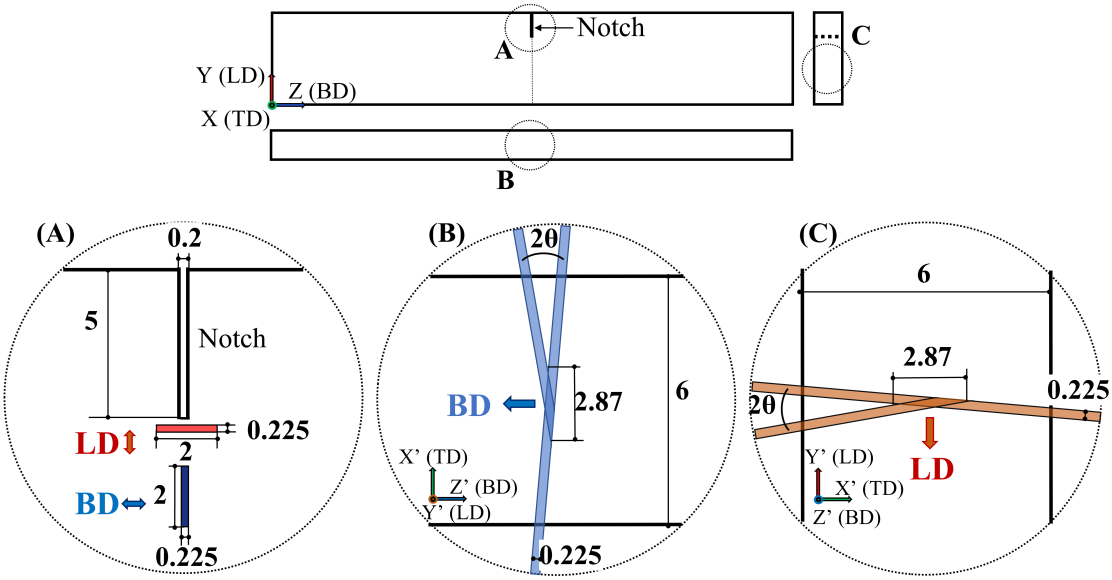

Figure 3.11.: Schematics of the configuration adopted for the SXRD measurements on SENB specimens. (A) Simplified representation of the beam size; (B) detail of the gauge length through the thickness for the BD measurements and (C) detail of the gauge length through the thickness for the LD measurements

3.3.5. Stress-free reference (d_0) determination

When the bulk lattice spacing of the material is probed, a stress-free reference must be used for the strain calculation (see Equation 3.4). Two different strategies were adopted for the ND and SXRD stress-free reference (d_0) determination.
Firstly, a 2 mm thick slice was extracted from the central part of a sister as-built SENB sample (see Figure 3.12a). Using electrical discharge machining, EDM, small $2\times2\times2$ mm^3 interconnected coupons were cut according to the pattern shown in Figure 3.12b. This strategy ensures relief of macro-stresses.
First, ND was performed on this grid, using a $2\times0.6\times0.6$ mm^3 gauge volume, to analyse the as-built condition and detect local variations of d_0 arising from compositional or microstructural gradients. This provide a d_0 for the as-built condition.
Subsequently the grid was cut in three parts and heat treated as shown in Figure 3.12c, to investigate the d_0 variation after heat treatment. SXRD was performed on the coupons in red in Figure 3.12c with a beam size of 2×2 mm^2, to maximise the peak intensity

measured and the volume over which the average value is taken.
A d_0 reference for the silicon was obtained by deep etching of the Al phase with a 80% HCl + 20% H_2O solution, in order to remove all the interphase stresses resulting from the interaction between silicon and aluminium. The Si deposits were measured in glass capillaries with a diameter of 1 mm by powder diffraction.

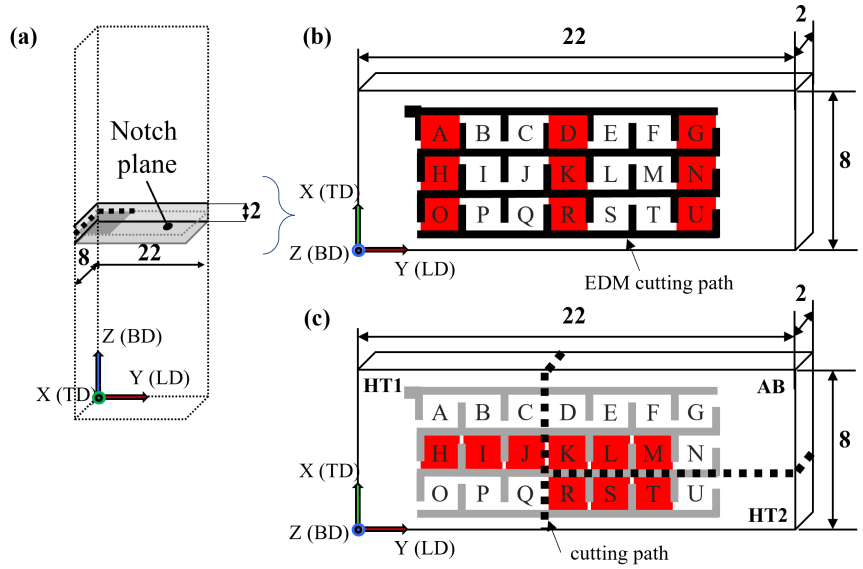

Figure 3.12.: Grid of interconnected coupons for the determination of the stress-free reference d_0: (a) location of the extracted material in a sister specimen, (b) geometry and coupons measured by ND (in red) and (c) cutting path for heat treatment (dashed line) and measured coupons by SXRD (in red).

Secondly, the plane-stress boundary condition which can be assumed at the notch faces was exploited to calculate d_0. At the two free surfaces inside the notch, the component perpendicular to the surface, namely BD, is assumed to be negligible. Therefore, $\sigma_{\mathbf{BD}}$ can be approximated to zero at this location.
For ND the three lattice spacing measurements in the principal geometrical directions are available, namely $d_{\mathbf{BD}}$, $d_{\mathbf{TD}}$, $d_{\mathbf{LD}}$. By replacing the strain component in Equation 3.5 as in the expression in Equation 3.4 a stress component σ_i can be written as follows:

$$\sigma_i = \frac{E}{1+\nu}\left(\frac{d_i}{d_0} - 1\right) + \frac{E\nu}{(1+\nu)(1-2\nu)}\left(\frac{d_i}{d_0} - 1 + \frac{d_j}{d_0} - 1 + \frac{d_k}{d_0} - 1\right) \tag{3.8}$$

By exploiting the condition $\sigma_{\mathbf{BD}} = 0$, d_0 can be calculated from the lattice spacing measured within the notch in the three directions: $d_{\mathbf{0,BD}}$, $d_{\mathbf{0,TD}}$, $d_{\mathbf{0,LD}}$ [123, 124]:

$$\sigma_{\mathbf{BD}} = \frac{E}{1+\nu}\left[\frac{d_{\mathbf{0,BD}}}{d_0} - 1 + \frac{\nu}{(1-2\nu)}\left(\frac{d_{\mathbf{0,BD}}}{d_0} - 1 + \frac{d_{\mathbf{0,TD}}}{d_0} - 1 + \frac{d_{\mathbf{0,LD}}}{d_0} - 1\right)\right] = 0 \quad (3.9)$$

$$d_0 = \frac{1-2\nu}{1+\nu}\left[d_{\mathbf{0,BD}} + \frac{\nu}{(1-2\nu)}(d_{\mathbf{0,BD}} + d_{\mathbf{0,TD}} + d_{\mathbf{0,LD}})\right] \quad (3.10)$$

For SXRD, two components were measured, namely $d_{\mathbf{BD}}$ and $d_{\mathbf{LD}}$. As additional condition $\sigma_{\mathbf{TD}} = 0$ also applies. Therefore, in a state of uniaxial stress, $\varepsilon_{\mathbf{TD}} = \varepsilon_{BD}$ and consequently the relation $d_{\mathbf{BD}} = d_{\mathbf{TD}}$ can be exploited in the Equation 3.10.
The second strategy was applied to both the as-built and the heat-treated specimens.

3.4. Fatigue behaviour of Al-Si-Mg alloys produced by Laser Powder Bed Fusion

3.4.1. Fatigue crack propagation

The fatigue crack propagation tests were performed using a RUMUL resonant fatigue testing machine with 20 kN load capacity. The specimens are subjected to cyclic loading under eight-point bending at a frequency of ~ 108 Hz. The direct current potential drop (DCPD) method was used to measure indirectly the crack length with an input current of 20 A. The set-up is shown in Figure 3.13a.
The specimens were tested at stress ratios $R = \frac{\sigma_{\mathbf{min}}}{\sigma_{\mathbf{max}}} = -1,\ 0.1,\ 0.8$ in the as-built, HT1 and HT2 conditions.

Short crack growth regime

For the cyclic R curve determination, no test guideline is available to date. The threshold and the crack growth rates in the near threshold regime are usually measured according to ASTM E647 [97] or ISO 12108:2012 [125]. However, this test procedure only provides the threshold of a long crack $\Delta K_{\text{th,LC}}$, but not the length dependence of the threshold. The procedure generally used in the literature was developed by Tabernig, Pippan et al. [126, 127]. This procedure was adopted in this study and is described below. A modification was adopted to be able to determine the upper part of the cyclic R-curve.
Before determining the cyclic R-curve, a precrack was generated by precracking. A

compressive load at ΔK=8 MPa$\sqrt{\text{m}}$ and $R = 20$ was applied. This method gives the advantage of an open precrack when the specimen is unloaded at the beginning of the cyclic R-curve test and the residual cyclic plastic zone ahead of the precrack is vanishingly small [126–129].

A stepwise increasing load amplitude crack growth test followed. A schematic is shown in Figure 3.13b. At the chosen stress ratio R, the load was stepwise increased, with the stress intensity factor range ΔK being in between the intrinsic (closure-free) $\Delta K_{\text{th,eff}}$ and the long crack $\Delta K_{\text{th,LC}}$ value (with fully developed crack closure effects). No crack advance occurs as long as ΔK is lower than $\Delta K_{\text{th,eff}}$. For $\Delta K_{\text{th,eff}} < \Delta K < \Delta K_{\text{th,LC}}$ the crack will initially grow, but after some propagation, it will arrest due to the gradual build-up of closure. Since aluminium alloys do not exhibit a fatigue limit, the crack does not arrest

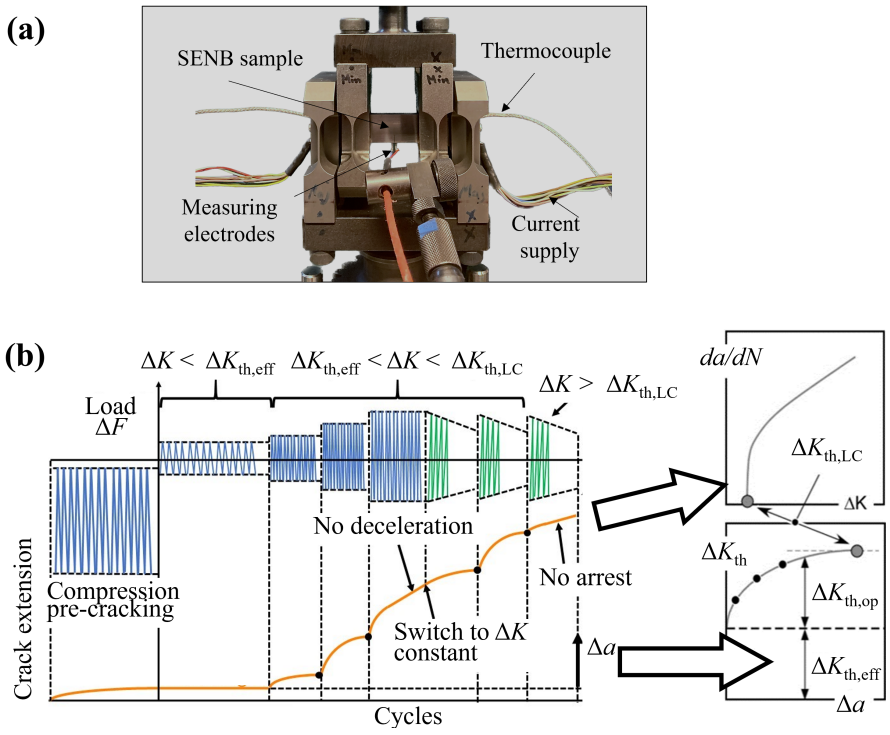

Figure 3.13.: (a) RUMUL resonant fatigue testing machine set-up and (b) description of the stepwise increasing load method for the determination of the cyclic R-curve.

completely (Figure 3.14). Therefore, the arrest condition was technically defined as the

drop in the propagation rate below a certain limit which was set equal to 10^{-8} mm/cycle, according to the standard ISO 12108:2012(E) [98, 125]. During the stepwise increasing

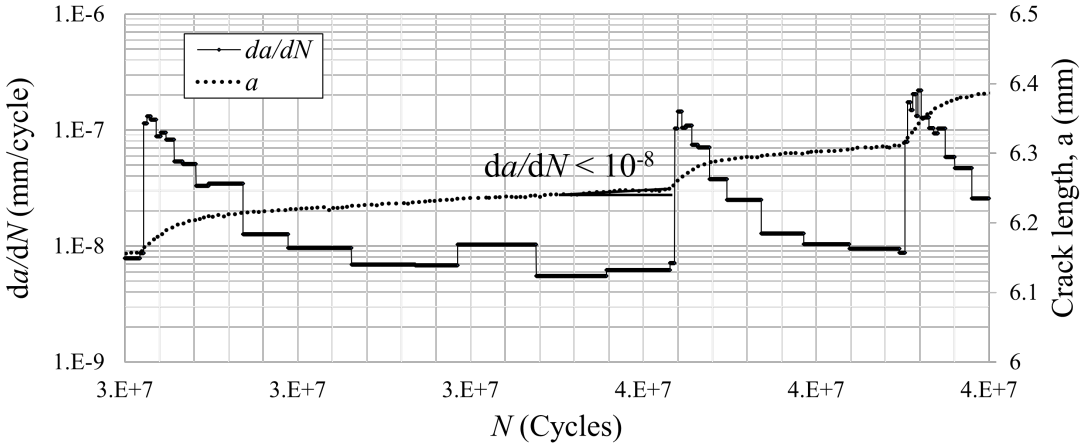

Figure 3.14.: Technical definition of the crack arrest: da/dN < 10^{-8} mm/cycle.

ΔF testing, as shown in Figure 3.13b, at a certain load level the crack tends to propagate without arresting. Here, switching to a ΔK constant testing mode, allows further arrest points to be observed and, thus, the upper part of the curve can be obtained.
Finally, when $\Delta K > \Delta K_{\text{th,LC}}$, the long crack threshold is exceeded, and the crack enters the Paris regime and will propagate until failure. The cyclic R-curve was finally generated by connecting the points $(\Delta a, \Delta K)$ of the consecutive arrest events.
Two models were fitted to the experimental data. First, a simple power law model proposed by *Zerbst et al.* [130] in a modified version with the crack extension Δa normalised with respect to $\Delta a_{\mathbf{LC}}$, the crack extension upon reaching the long crack threshold $\Delta K_{\text{th,LC}}$:

$$\Delta K_{\mathbf{th}}(\Delta a) = \begin{cases} A \cdot \left(\dfrac{\Delta a}{\Delta a_{\mathbf{LC}}}\right)^{b} + \Delta K_{\text{th,eff}} & \textbf{for} \quad \Delta a < \Delta a_{\mathbf{LC}} \\ \Delta K_{\text{th,LC}} & \textbf{for} \quad \Delta a > \Delta a_{\mathbf{LC}} \end{cases} \tag{3.11}$$

And secondly, the equation proposed by *Maierhofer et al.* [131] for short crack behaviour below the threshold for long crack growth was used to fit the data.

$$\Delta K_{\mathbf{th}}(\Delta a) = \Delta K_{\text{th,eff}} + (\Delta K_{\text{th,LC}} - \Delta K_{\text{th,eff}}) \left[1 - \sum_{i=1}^{n} \nu_i \cdot e^{-\frac{\Delta a}{l_i}}\right] \tag{3.12}$$

with the constrain condition

$$\sum_{i=1}^{n} \nu_i = 1 \tag{3.13}$$

The l_i can be interpreted as fictitious length scales for the formation of crack closure effects and can be determined in conjunction with the ν_i by fitting of the experimentally obtained crack growth resistance curve.

Long crack growth regime

At stress ratios $R = -1$ and 0.1, after determining the cyclic-R curve, when the long crack threshold was exceeded, a constant force amplitude (ΔF-constant) test procedure was applied on the residual ligament to obtain the $\mathrm{d}a/\mathrm{d}N - \Delta K$ curves [125].
The $\mathrm{d}a/\mathrm{d}N - \Delta K$ curves at $R = 0.8$ were determined according to ISO 12108 with a standard *K*-decreasing procedure, starting from ΔK = 1.5 MPa$\sqrt{\mathrm{m}}$. When the threshold was reached, the remaining ligament was used to continue the test by applying the constant-force procedure from ΔK = 1.3 MPa$\sqrt{\mathrm{m}}$ to obtain the upper branch of the curve (Paris' regime).
The modified NASGRO equation was fitted to the data[132]. The high propagation rate regime was not measured; therefore the term for the fracture toughness regime is neglected. The fitting equation is used in the form:

$$\frac{da}{dN} = C\left[\left(\frac{1-f}{1-R}\right)\Delta K\right]^{n}\left[1-\frac{\Delta K_{\mathbf{th}}}{\Delta K}\right]^{p} \tag{3.14}$$

where R is the stress ratio, f is the Newman crack closure function [133], ΔK is the stress intensity range, C is the Paris' constant, and n is the Paris' exponent. The Newman crack closure function is determined by the equation:

$$f = \begin{cases} \mathbf{max}(R; A_0 + A_1 R + A_2 R^2 + A_3 R^3) & \text{for } R \geq 0, \\ A_0 + A_1 R & \text{for } -2 \leq R \leq 0, \\ A_0 + 2A_1 & \text{for } R \leq -2 \end{cases} \tag{3.15}$$

with the A_i coefficients calculated as:

$$\begin{aligned} A_0 &= (0.825 - 0.34\alpha + 0.05\alpha^2)cos\left(\frac{\pi \cdot \sigma_{\mathbf{max}}}{2\sigma_0}\right)^{(1/\alpha)} \\ A_1 &= (0.415 - 0.071\alpha)\frac{\sigma_{\mathbf{max}}}{\sigma_0} \\ A_3 &= 2A_0 + A_1 - 1 \\ A_2 &= 1 - A_0 - A_1 - A_3 \end{aligned} \tag{3.16}$$

the constrain factor α accounts for three-dimensional constraint effects for tensile yielding and depends on crack geometry and remote loading conditions. When the plastic zone is small compared to the material thickness, nearly plane strain conditions are applicable. Therefore, $\alpha = 3$ was assigned for approximate plane strain condition [134]. $\sigma_{\mathbf{max}}/\sigma_0 =$

0.3 was assigned assuming a largely elastic crack behaviour [131]. $\Delta K_{\mathbf{th}}$ is the threshold stress intensity range at the stress ratio R under consideration and p is the exponent that determine the curvature of the growth rate curve in the near-threshold regime. The term $(1-f)/(1-R)$ in Equation 3.14 is referred to as U and represents a crack closure correction, based on the function of Newman, which takes into account the plasticity-induced component of closure. Hence, an effective stress intensity factor range can be defined as $\Delta K_{\mathbf{eff}} = U \cdot \Delta K$. The Newman crack closure function f and crack closure ratio U, calculated for the tested stress ratios ($R = -1,\ 0.1,\ 0.8$), are reported in Table 3.3.

Table 3.3.: Summary of the Newman crack closure function f and crack closure ratio U for the stress ratios used for the testing.

R	f	U
-1	0.18	0.41
0.1	0.26	0.82
0.8	0.80	1.00

3.4.2. High Cycle Fatigue

High cycle fatigue (HCF) tests were performed using a uniaxial servohydraulic Schenck 25kN testing machine at a load ratio $R = 0.1$ and a frequency of 30 Hz in force-control mode. A stress range between 35 and 105 MPa was investigated, which corresponds to a fatigue life range between $10^3 - 10^7$ cycles. The tests, in the event that the failure did not occur, are interrupted at 10^7 cycles. The runout specimens were retested at the highest stress level, at a load which give a failure in the range of $10^3 - 10^4$ cycles, to minimise the influence of accumulated damage (assumed to be negligible). The specimens tested were produced in two different batches (batch 1 and 2), each containing 30 specimens. In each batch, ≈10 specimens were tested for each heat treated conditions (AB, HT1 and HT2). The Basquin model was fitted to the data. The statistical analysis was performed according to ISO 12107:2012 [135].

3.4.3. Cyclic stress-strain response

The cyclic stress-strain response of the material was investigated performing axial strain-controlled incremental-step tests (IST) on a Schenck 25kN servohydraulic machine, with a strain rate of $0.05\ \%/s$. Six sample in total from batch 1 were tested, two for each

heat treated condition. In the IST method, a single specimen is subjected to repeated blocks of incrementally increasing and decreasing strain amplitudes between 0.3% and 0.9% (Figure 3.15a). After few blocks the response stabilises. The stabilised cycle is selected from the central block of the test (total number of blocks divided by 2), excluding from the count the final blocks where a reduction in the maximum force applied during the test of more than 10% is observed (see example in Figure 3.15b). A stress ratio

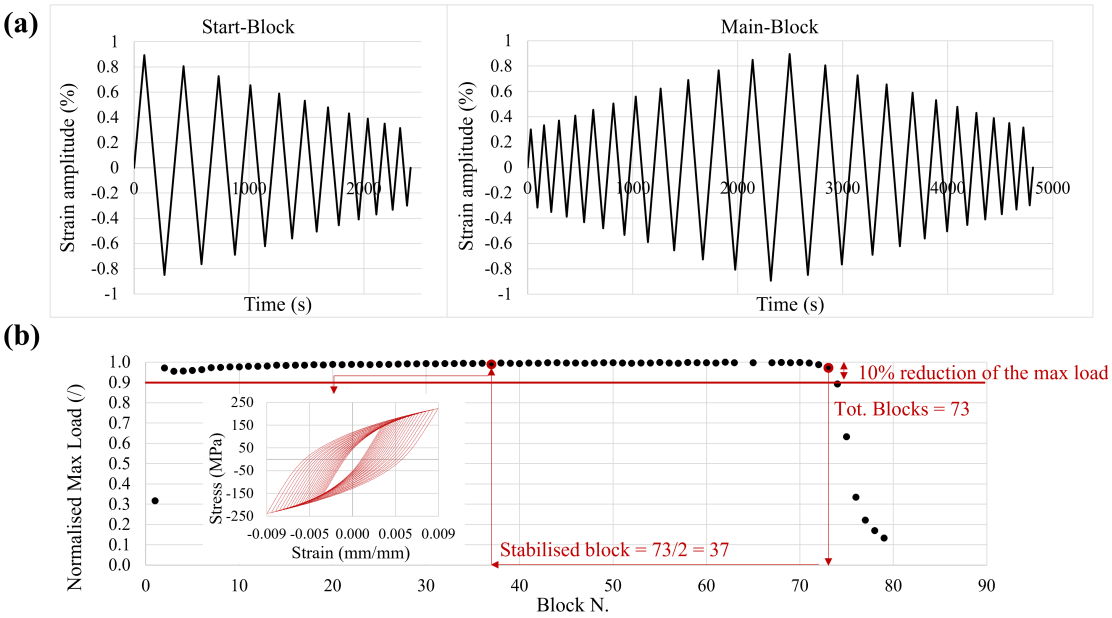

Figure 3.15.: Incremental-step testing method (IST) for investigating the cyclic stress-strain response. (a) Applied strain amplitude and (b) selection of the stabilised block.

$R = -1$ was applied and the strain was measured using a clip-on gauge extensometer. The stabilised hysteresis loops for various deformation levels were then collected and a Ramberg-Osgood [136, 137] equation was fitted to these data:

$$\varepsilon = \frac{\sigma}{E} + \left(\frac{\sigma}{K'}\right)^{\frac{1}{n'}} \tag{3.17}$$

where ε is the strain, σ the stress, E the elastic modulus, K' the cyclic strength coefficient and n' the cyclic strain-hardening exponent. The average value of the two performed tests

in the same condition was taken for σ, E, K' and n'. The Masing's hypothesis was verified for all the HT conditions, more details are provided in Appendix D.

3.4.4. Modelling of fatigue resistance

The scatter of the fatigue strength can be reduced if data are correlated to the defect size at failure origin (killer defect) [138]. Various models proposed in the literature have been studied and compared in an attempt to reduce this scatter.
The model commonly used in the literature to describe stress-defect interactions was proposed by *Murakami* [139]. Small defects are approximated as elliptical cracks which exhibit stress intensity factors ΔK at the tip of the defects calculated as:

$$\Delta K = F \cdot \Delta\sigma \cdot \sqrt{\pi\sqrt{area}} \tag{3.18}$$

where $\Delta\sigma$ is the remote stress range applied to the component, $\sqrt{area}$ is the root area of the defect projected into the loading plane perpendicular to the applied stress and F is a geometry factor, which takes into account the crack or defect position and configuration. For surface defects $F = 0.65$ and for internal voids $F = 0.5$.
El-Haddad, Smith and *Topper* [140, 141] proposed a correction to include the short crack effect, whereby short cracks exhibit a higher crack propagation rate, as compared to long cracks subjected to the same linear elastic ΔK. The *short crack-corrected* stress intensity factor range for the killer defects, including in the formulation the shape factor F, can be calculated as:

$$\Delta K_{\mathbf{corr}} = \Delta\sigma \cdot \sqrt{\pi(F^2\sqrt{area} + \sqrt{area}_0)} \tag{3.19}$$

where $\sqrt{area}_0$ is a material parameter, dependent on the fatigue long cracks threshold $\Delta K_{\text{th,LC}}$ and on the fatigue limit of the flawless material $\Delta\sigma_{\mathbf{e}}$:

$$\sqrt{area}_0 = \frac{1}{\pi}\left(\frac{\Delta K_{\text{th,LC}}}{\Delta\sigma_{\mathbf{e}}}\right)^2 \tag{3.20}$$

Kitagawa-Takahashi diagram A widespread concept to assess the effect of defects on fatigue resistance was introduced by *Kitagawa and Takahashi* [142]. The fatigue crack growth threshold ($\Delta K_{\text{th,LC}}$) and the fatigue endurance limit ($\Delta\sigma_{\mathbf{e}}$) can be combined into a single plot by the Kitagawa-Takahashi (KT) diagram, which defines the area of non-propagating cracks (leading to infinite fatigue life). Thereby, the HCF strength $\Delta\sigma_{\mathbf{th}}$ can be estimated as a function of the crack or equivalent defect size $\sqrt{area}$ as:

$$\Delta\sigma_{\mathbf{th}} = \frac{\Delta K_{\text{th,LC}}}{F \cdot \sqrt{\pi\sqrt{area}}} \tag{3.21}$$

However, it was observed that the experimental data follow a gradual transition from the fatigue limit of the smooth specimens to that of components weakened by a long crack. Therefore, an alternative formulation of the KT diagram was proposed by *El-Haddad, Topper and Smith* [140, 141], who suggest a polynomial transition from the intrinsic fatigue strength to the defect-affected region:

$$\Delta\sigma_{\mathbf{th}} = \frac{\Delta K_{\text{th,LC}}}{F \cdot \sqrt{\pi(\sqrt{area} + \sqrt{area}_{0,F})}} = \Delta\sigma_{\mathbf{e}} \sqrt{\frac{\sqrt{area}_{0,F}}{\sqrt{area} + \sqrt{area}_{0,F}}} \tag{3.22}$$

Here, $\sqrt{area}_{0,F}$ takes into account the defect position and configuration and is calculated considering, in addition to the $\Delta K_{\text{th,LC}}$ and the fatigue limit of the flawless material $\Delta\sigma_e$, the shape factor F:

$$\sqrt{area}_{0,F} = \frac{1}{\pi} \cdot \left(\frac{\Delta K_{\text{th,LC}}}{F \cdot \Delta\sigma_{\mathbf{e}}} \right)^2 \tag{3.23}$$

Equation 3.22 can be rewritten in terms of stress intensity factor threshold $\Delta K_{\mathbf{th}}$ as follows:

$$\Delta K_{\mathbf{th}} = \Delta K_{\text{th,LC}} \sqrt{\frac{\sqrt{area}}{\sqrt{area} + \sqrt{area}_{0,F}}} \tag{3.24}$$

An alternative model to describe the fatigue limit of a specimen containing small defects was proposed by Murakami [139, 143]. With this model, the influence of the microstructure on the fatigue threshold is taken into account by simply using the Vickers hardness (HV) according to the following equation:

$$\Delta\sigma_{\mathbf{th}} = \frac{C(HV + 120)}{(\sqrt{area})^{1/6}} \tag{3.25}$$

with C=1.43 for surface defects and C=1.56 for interior defects. The equation is rewritten in terms of $\Delta K_{\mathbf{th}}$ as follows:

$$\Delta K_{\mathbf{th}} = G(HV + 120) \cdot (\sqrt{area})^{1/3} \tag{3.26}$$

where G=3.3$\times 10^{-3}$ for surface defects and G=2.77$\times 10^{-3}$ for interior defects. It should be noted, however, that Equations 3.25 and 3.26 are only valid for fully reversed load. A more general expression for R$\neq$-1 was provided:

$$\Delta\sigma_{\mathbf{th}} = \frac{C(HV + 120)}{(\sqrt{area})^{1/6}} \cdot \left[\frac{1 - R}{2} \right]^{\alpha} \tag{3.27}$$

where $\alpha = 0.226 + HV \cdot 10^{-4}$. However, this correction for the mean stress has not been validated for aluminium alloys.
A schematic of the KT diagram, summarising the aforementioned models, is shown in Figure 3.16.

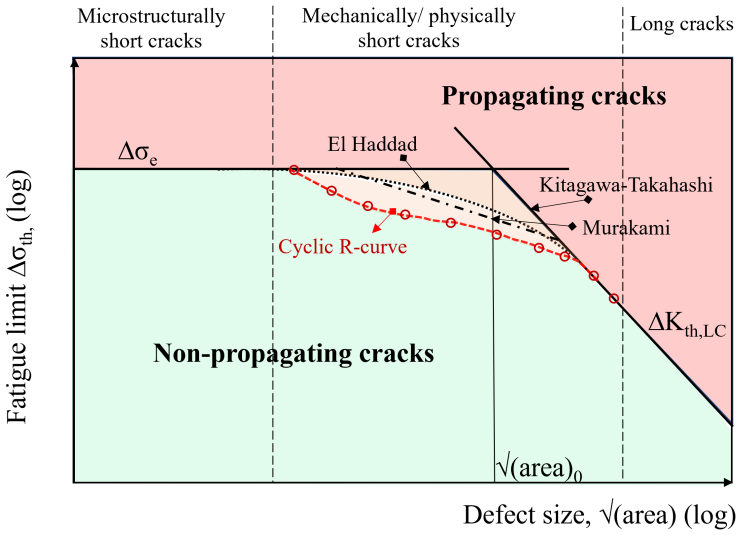

Figure 3.16.: Schematic of the Kitagawa-Takahashi diagram: comparison between the El Haddad formulation and the cyclic R-curve analyses approach.

Atzori et al. [144] interpreted Equation 3.22 in a new fashion, in order to keep $\sqrt{area}_0$ as a solely material dependent parameter, which defines the material sensitivity to defects, as originally defined by *El Haddad et al.* and reported in Equation 3.20. For this purpose, an effective defect size $\sqrt{area}_{\mathbf{eff}}$ is introduced:

$$\sqrt{area}_{\mathbf{eff}} = F^2 \sqrt{area} \tag{3.28}$$

The Equations 3.22 can be therefore rewritten as follow:

$$\Delta\sigma_{\mathbf{th}} = \frac{\Delta K_{\text{th,LC}}}{\sqrt{\pi(\sqrt{area}_{\mathbf{eff}} + \sqrt{area}_0)}} = \Delta\sigma_{\mathbf{e}} \sqrt{\frac{\sqrt{area}_0}{\sqrt{area}_{\mathbf{eff}} + \sqrt{area}_0}} \tag{3.29}$$

or alternatively, in terms of SIF:

$$\Delta K_{\mathbf{th}} = \frac{\Delta K_{\text{th,LC}}}{\sqrt{\frac{\sqrt{area}_{\mathbf{eff}}}{\sqrt{area}_{\mathbf{eff}} + \sqrt{area}_0}}} \tag{3.30}$$

where $\sqrt{area}_0$ is defined by Equation 3.20.

Cyclic resistance curve method (cyclic R-curve analysis) The cyclic R-curve can be used for the prediction of crack arrest in components. The concept is illustrated in Figure 3.17. Generally, in the case of AM materials, a defect is at the origin of crack nucleation. The nucleated crack, whose initial length can be estimated as $a_i = \sqrt{area}$, is assumed to be closure-free, i.e. the crack is fully open and its propagation threshold is $\Delta K_{\text{th,eff}}$. a_i sets the origin of the cyclic R-curve, as it is the point from which the crack closure starts developing. The resistance curve analysis can be carried out by combining in the same graph the cyclic R-curve which starts at the level of $\Delta K_{\text{th,eff}}$ and at the initial crack size a_i with the crack driving force curves of the component, associated to a growing crack for a given constant applied stress amplitude $\Delta\sigma$. The crack driving force curve which tangentially touches the cyclic R-curve defines the crack propagation/arrest limit.

When the initial defect sizes are in the range of the mechanically short cracks, the short crack size is in the same order of magnitude of the size of the plastic zone ahead of the crack tip. Therefore, calculating the crack driving force, the plasticity-induced effects must be taken into account and the linear elastic fracture mechanics can not be used. In contrast to microstructurally short cracks, for which the crack driving force cannot be calculated by means of fracture mechanics concepts, in case of mechanically short cracks it is possible to use fracture mechanics, adopting elastic-plastic concept as the cyclic *J*-integral ΔJ [145]. ΔJ was obtained from the analytical equation by *Dowling* [146] for a semi-circular surface crack:

$$\Delta J = a \left[1.24 \frac{(\Delta\sigma)^2}{E} + \frac{1.02}{\sqrt{n'}} \Delta\sigma \Delta\varepsilon_{\mathbf{p}} \right] \tag{3.31}$$

with *n'* being the cyclic strain hardening exponent as defined by the Ramberg-Osgood expression (Equation 3.17), *a* is the crack depth, $\Delta\sigma = \sigma_{\mathbf{max}} - \sigma_{\mathbf{min}}$ is the applied stress and the plastic strain $\Delta\varepsilon_{\mathbf{p}} = \Delta\sigma - \Delta\sigma/E$. The expression is valid if the material exhibits Masing's hypothesis. ΔJ is formally transferred to a "plasticity-corrected" $\Delta K_{\mathbf{p}}$ by:

$$\Delta K_{\mathbf{p}} = \sqrt{\Delta J \cdot E'} \tag{3.32}$$

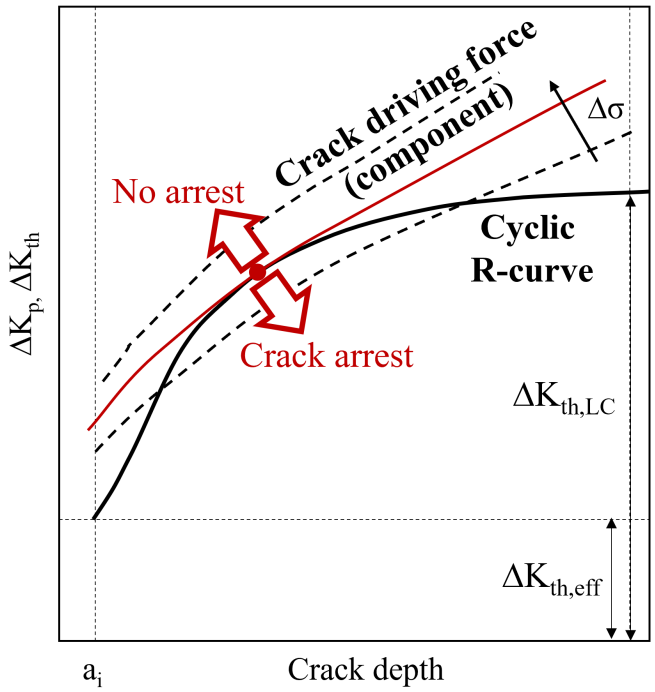

Figure 3.17.: Schematic of the resistance curve method. Given an initial crack depth ai and the corresponding cyclic R-curve, the lower stress limit to crack propagation is determined by the tangency of the crack driving force curve to the resistance curve.

where E' is the Young's modulus, modified for plane strain:

$$E' = \frac{E}{(1-\nu^2)} \tag{3.33}$$

where E is the Young's modulus and ν the Poisson's ratio.

4. Microstructure, Mechanical Properties and Residual Stress Characterisation

When an external load is applied to an Al-Si alloy component, the key parameters governing the fatigue properties have been reported to be the porosity content, the morphology of the silicon phase, residual stress (RS), the tensile strength and ductility. The porosity content is determined by the processing parameters and is barely unchanged by post-processing. On the contrary, as introduced in Chapter 2.2, AlSi10Mg microstructure, mechanical properties and RS state can be greatly modified by applying heat treatments. The heat treatments performed in this study were selected on the basis of a review of the state of the art and further microstructure analyses reported and discussed in this chapter. Special attention is dedicated herein to the evaluation of the RS state, as the literature review evidenced a lack of knowledge regarding the RS-microstructure relationship as a function of heat treatment.

4.1. PBF-LB/M AlSi10Mg microstructure

4.1.1. Scanning electron microscopy (SEM)

The evolution of the microstructure after heat treatments was evaluated mainly by scanning electron microscopy (SEM) on the batch 1 material.
The selection of the temperatures for the heat treatments performed and investigated in this study is based on the differential scanning calorimetry (DSC) studies discussed in Chapter 2.2.1. Nevertheless, additional preliminary tests were performed to verify the evolution of the microstructure over time at temperatures highlighted as significant by DSC records. SEM micrographs were taken after different holding times at 300°C: 15 min, 30 min, 1 h and 2 h. The results are shown in Figure 4.1 and prove that a spheroidised Si particles dispersion is achieved after 2 hours at 300°C.
Moreover, the velocity with which the microstructure evolves at a fixed temperature was assessed through Synchrotron X-ray refraction during in-situ heat treatments [26]. With this technique the changes in the Si-phase morphology upon heating were detected,

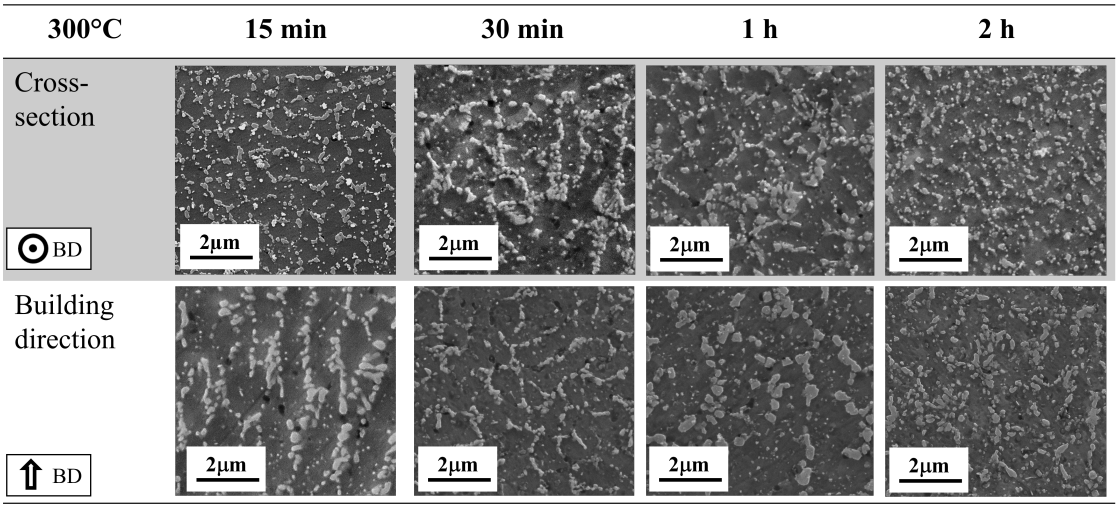

Figure 4.1.: PBF-LB/M AlSi10Mg SEM-SE micrographs in the cross-section and building direction after 15 min, 30 min, 1 hour and 2 hours at 300°C.

further confirming the results in the literature and providing an initial reference for the soaking time during heating.
After the above evaluations, the most relevant heat treatment schemes were decided to be 1 hour at 265°C for HT1 and 2 hours at 300°C for HT2.

SEM micrographs were taken in the as-built and heat-treated conditions in the cross-section. The modifications reported in the literature are also observed in the micrographs shown in Figure 4.2 and can be summarised in what follows:

- in the as-built state (Figure 4.2a) the aluminium matrix (in dark grey) is enclosed in a submicrometric Si network. The as-built aluminium cells contain very fine entrapped eutectic Si particles with a diameter generally smaller than 20 nm.
- after 1 hour at 265°C (Figure 4.2b) the precipitation of solid solution silicon from the matrix results in a coarsening of the aluminium cells and of the eutectic network.
- at 300°C (Figure 4.2c) the breakdown of the eutectic Si networks by interdiffusion is triggered, leading to a homogeneous distribution of submicrometric particles after 2 hours .

The EBSD orientation map in Figure 4.2d distinctively shows the melt pool boundaries, as well as a gradual coarsening of the grain size from the melt pool boundary towards

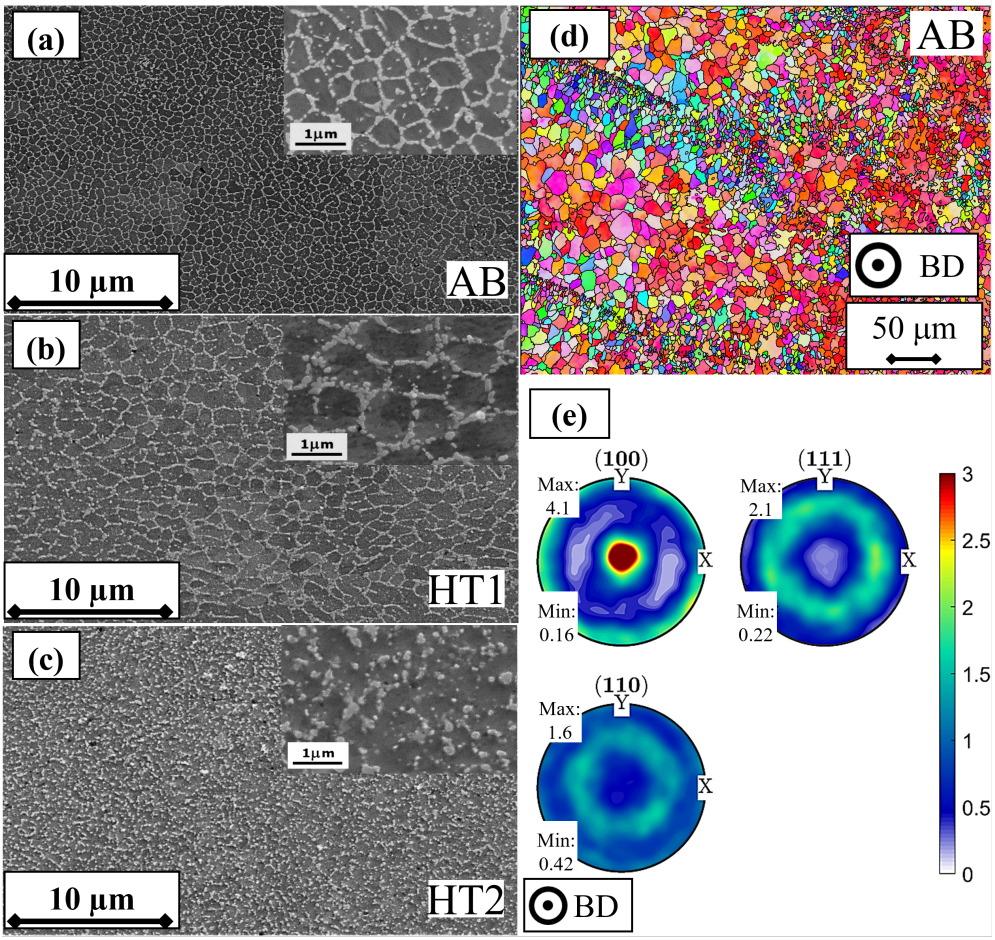

Figure 4.2.: PBF-LB/M AlSi10Mg SEM-SE micrographs at different magnifications in the cross-section for the (a) as-built, (b) after 1 hours at 265°C and (c) after 2 hours at 300°C. (d) EBSD orientation map on the cross-section in the as-built condition, with (e) the respective (100), (110) and (111) pole figures.

its centre. A moderately strong $\langle 100 \rangle$ // BD fibre texture is indicated by the pole figures (Figure 4.2e). Such texture is predominant near the melt-pool centre, where the growth direction is more closely aligned with the overall heat flow direction [147].

4.1.2. X-ray microtomography (μCT)

The HCF specimens were produced in two batches of 30 samples with the geometry and the process parameters described in Chapter 3.1, before (batch 1) and after (batch 2) maintenance of the Concept M2 machine. The second batch was printed after adjustments in the laser optics of the machine. μCT evaluations evidenced a reproducibility issue by showing significant differences in the defect content of the two batches. The void distribution is shown in Figure 4.3. The first batch of samples (Figure 4.3b,d) contains a

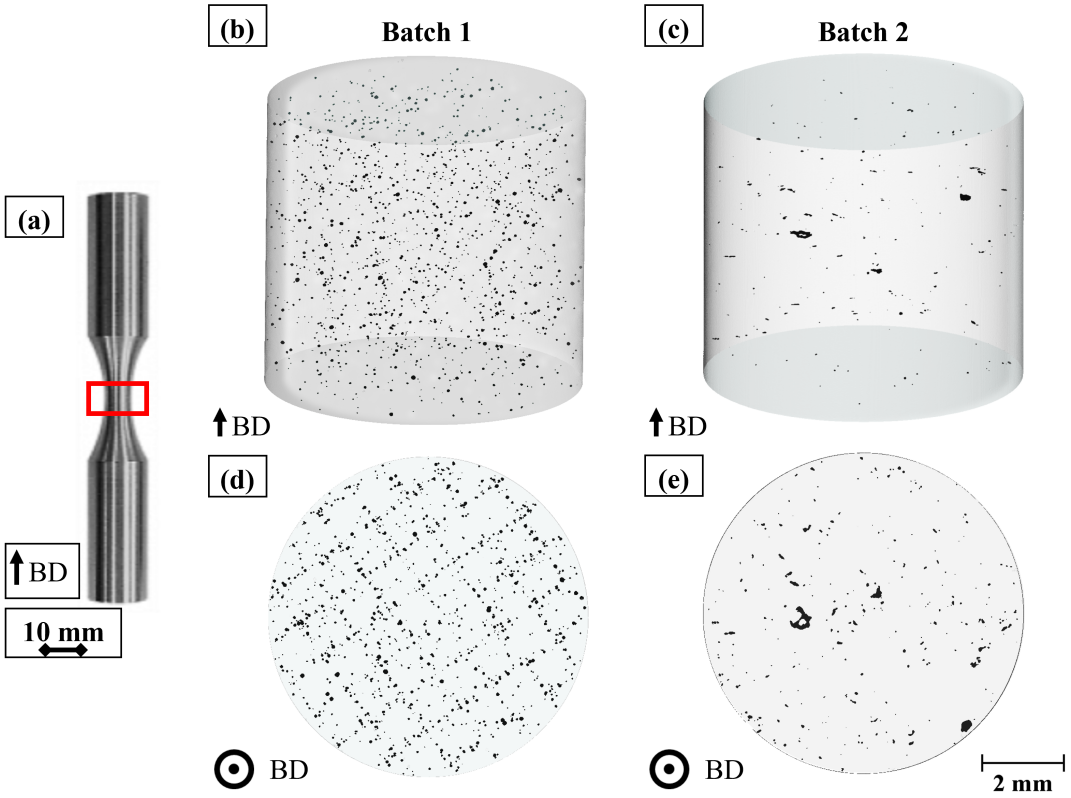

Figure 4.3.: μCT 3D rendering of the gauge volume of two HCF samples (the region of interest location is shown in (a)): (b,d) volume representative of batch 1 and (c,e) volume representative of batch 2.

greater amount of defects, almost entirely gas pores, with an average size of 50μm. The

porosity is preferentially distributed along the boundaries between adjacent islands of the chessboard scanning pattern. These pores can be associated to an excessive volumetric energy density during the printing process [148]. Three different samples were scanned and showed similar defect patterns. Thus, the pore distribution, in terms of size and position, was proved to be uniform along the entire building platform and, for sake of brevity, one specimen is considered representative of the entire batch. On the contrary, in the second batch, fewer defects with a different geometry are observed (Figure 4.3c,e). Defects are mainly lack of fusion, with a size up to 225 μm. In this batch, the distribution of defects is very inhomogeneous, therefore four specimens were analysed to ensure a better statistical coverage.
The fatigue limit is the non propagating condition for the larger single defect [139, 149]. To this purpose, an extreme value statistics method, suitable to describe the upper tail of a defect distribution, was adopted: the Peak-Over-Threshold (POT). The main concept of the POT is to fix a threshold u to seclude values considered extreme (the biggest defects of each distribution) and model these exceedances, which show asymptotic properties, with an extreme value distribution such as the generalized Pareto distribution (GPD). An appropriate threshold u was found to be 49μm by plotting the mean excess (see Appendix B for more details). In Figure 4.4 the two batches are compared by means of the probability papers and the porosity sphericity. Since the negative exponential probability plot $((x-u), -LN(1-F))$, in Figure 4.4a, shows a linear trend, the tails of the defect size distribution can be approximated to an exponential distribution. Consequently, the shape parameter ε of the GPD approaches 0, and the cumulative density function of the generalized Pareto distribution becomes a two-parameter exponential distribution:

$$F(x) = 1 - e^{-\frac{x-u}{\sigma}} \tag{4.1}$$

and the maximum likelihood method was applied to estimate the scale parameter σ.
Batch 1 shows the highest defects density (number per volume unit), but with a regular round-shape, while the second batch presents fewer defects globally, but of bigger size and irregular shape, where the sphericity decreases with increasing size, reaching a minimum of 0.3. Even if the overall density in the batch 2 is larger than for the batch 1, the lower number of large defects results in a much smaller maximum defect size: 95 μm against 225 μm in the second batch. The scale parameter σ is equal to 10 for batch 1 and falls between 22 and 33 for the batch 2. Importantly, a previous study proved that the porosity size is not affected by heat treatments in the temperature range studied [26].

Table 4.1.: Comparison between batch 1 and 2.

		Batch 1	Batch 2
Defect type	Lack of fusion	∼6%	∼91%
	Gas porosity	∼94%	∼9%
Density	$1 - \frac{Vol_{\text{voids}}}{Vol_{\text{tot}}}$	99.95%	99.98%
Max defect size	$\sqrt{area}$	95 μm	225 μm

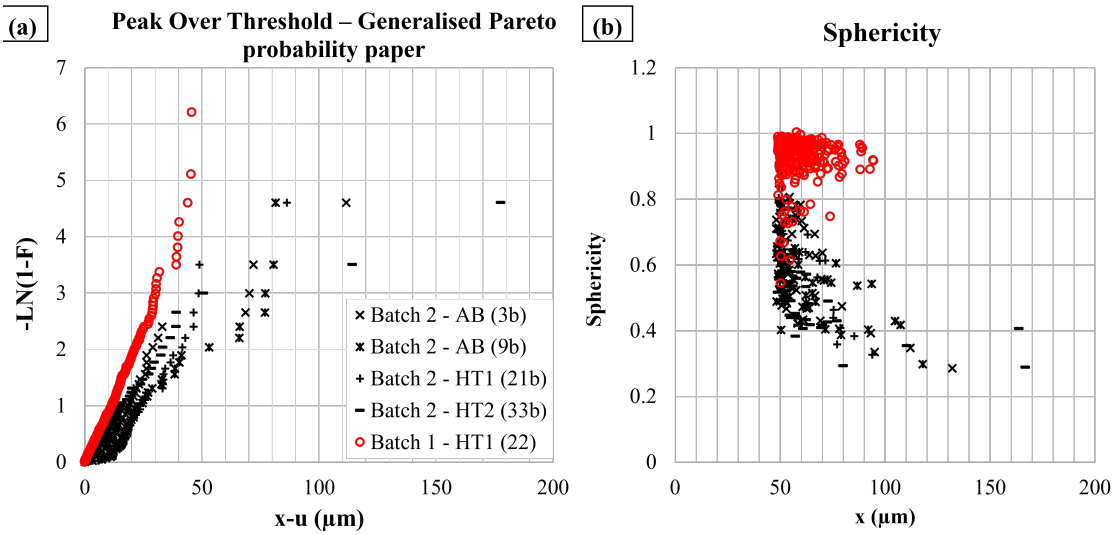

Figure 4.4.: Comparison between batch 1 and 2: (a) probability plot (negative exponential) and (b) sphericity of the distributions analysed. The samples measured for batch 1 are well summarised by HT1-22. For batch 2 four different samples are shown to account for the great variability within the batch: AB-3b, AB-9b, HT1-21b and HT2-33b.

4.2. PBF-LB/M AlSi10Mg quasi-static mechanical properties

The stress-strain curves of the PBF-LB/M AlSi10Mg for the AB, HT1 and HT2 conditions are shown in Figure 4.5. The tests were performed on the batch 2. The mechanical properties are reported in Table 4.2. The results are in agreement with the studies in the literature

summarised in Chapter 2.5.1 and provide an indication of the increased ductility of the alloy after heat treatment. The elongation at break doubled after HT1 and tripled after HT2, at the expense of a decrease of the tensile strength of 12% and 36%, respectively. The Vickers hardness (HV) as a function of the heat treatment is also reported in Table 4.2.

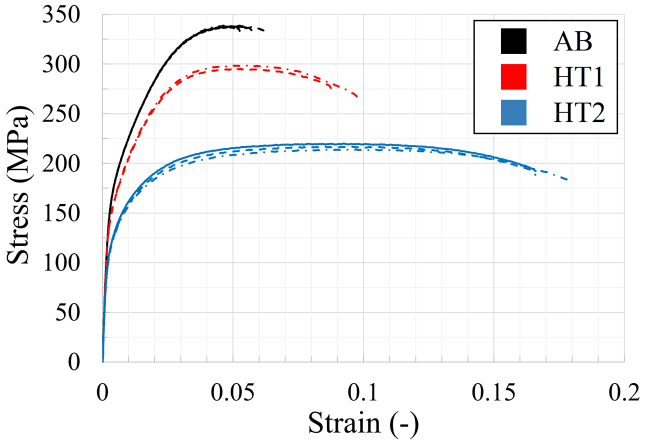

Figure 4.5.: Stress-strain curves of the PBF-LB/M AlSi10Mg in the as-built and heat-treated conditions. Three specimens were tested at each condition.

Table 4.2.: Mechanical properties of the PBF-LB/M AlSi10Mg as-built and heat-treated

Condition	Yield strength $R_{p0,2}$ (MPa)	Tensile strength R_m (MPa)	Uniform extension A_g (%)	Elongation at break A (%)	Vickers hardness HV
AB	178	338	5	6	86
HT1	158	297	5	10	80
HT2	123	217	9	18	69

The measurements were performed on both the batches yielding the same results. Thus, it is assumed that the tensile strength (R_m) is also comparable between the two batches. In addition, in Figure 4.6, the results of the nanoindentation measurements are plotted in terms of minimum, maximum and average values measured in the ExpressTest map (see Chapter 3.2). At the bottom of the figure, a schematic where the surface probed by the indenter during the test is depicted in orange is presented. This sketch shows that the microstructure features are small compared to the indenter head, thus the contribution

to the hardness measurement of the silicon cannot be fully separated from that of the aluminium matrix. Consequently, the measured minimum hardness can only provide a qualitative description of the hardness evolution in the matrix after heat treatment. In the as-built state, the α-aluminium is supersaturated with silicon atoms resulting in a less compliant matrix. The contact area of the indenter is larger than the aluminium cells. After HT1, a softening of the matrix is observed due to the silicon precipitation. At 300°C the breakdown of the silicon networks occurs. The resulting microstructure is a fine and homogeneous distribution of Si particles. This leads to a fictitious increase in the matrix hardness, since the contact area always includes some silicon particles. Moreover, the hardness was measured after 1 and 5 hours of heat treatment at 300°C. No noteworthy changes are observed after 5 h, thus the same hardness can also be assumed for a soaking time of 2 hours.

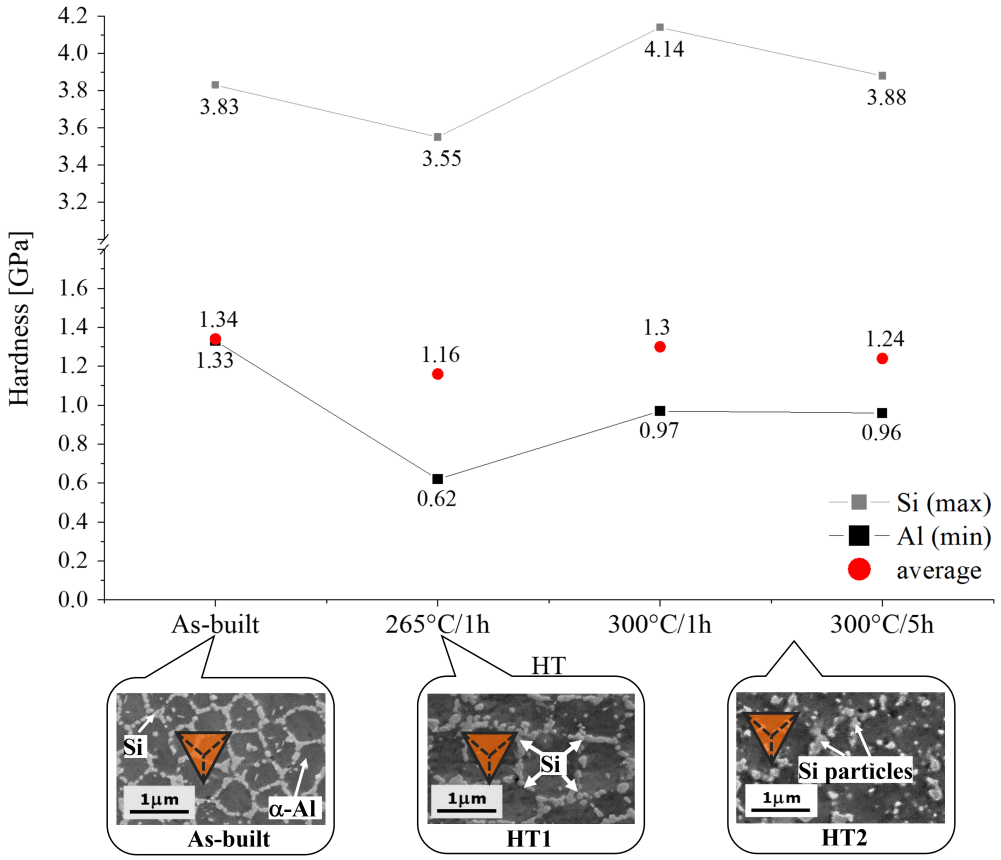

Figure 4.6.: Nanohardness evolution through heat treatment. Minimum, maximum and average hardness values are obtained from an ExpressTest where the hardness was mapped by 10000 indents on a 100×100 μ array, with 1 μ pitch. The penetration depth of the indenter is ca. 100 nm.

4.3. Residual stress state in PBF-LB/M AlSi10Mg SENB samples

The stress state was investigated in three fatigue crack propagation SENB specimens that underwent different post-processing: in the as-built, HT1 and HT2 conditions respectively. A complete evaluation of the stress state is provided, from the near-surface, investigated with laboratory EDXRD, to the bulk of the specimen, analysed by means of ND and SXRD. Moreover, SXRD is also used in order to elucidate the role and magnitude of the Al/Si interphase strains and stresses, as this technique allows resolving the Si diffraction peaks. It is thereby possible to evaluate the stress repartition between the aluminium and the silicon phase.

4.3.1. Laboratory Energy Dispersive X-rays

The subsurface RS determined in the as-built condition and after heat treatments (HT1 and HT2) are compared in Figure 4.7 and 4.8. The RS were measured by Energy-Dispersive X-rays diffraction in the BD and LD, along a line (xi) at 27 mm from the notch plane (Figure 4.7) and on some points surrounding the notch (lines (xii) and (xiii), in Figure 4.8). The front and back surfaces of the specimen where measured and comparable values were found, thus only the RS profile on one side is reported.
The near-surface region exhibits compressive RS in both the BD and the LD in all the conditions, with an average value of $\sim$-70 MPa in the BD and $\sim$-80 MPa in the LD. A fluctuating trend is observed in the profile that will be discussed in more detail in the following section.
The near-surface stress state (at a depth of 350 μm) is not affected by heat treatment. This is also confirmed by the calculated stress ranges, namely the difference between the maximum and minimum values in the profiles of Figure 4.7, shown in Figure 4.9. This similarity observed is surprising as the results presented below point out a change, induced by heat treatment, in the magnitudes of the bulk RS. It can be assumed that the measured near-surface RS state, is still affected by the surface machining and grinding performed to obtain the final SENB geometry from the raw plates. Nevertheless, the assessment of the influence of machining in the RS state is beyond the scope of this work.

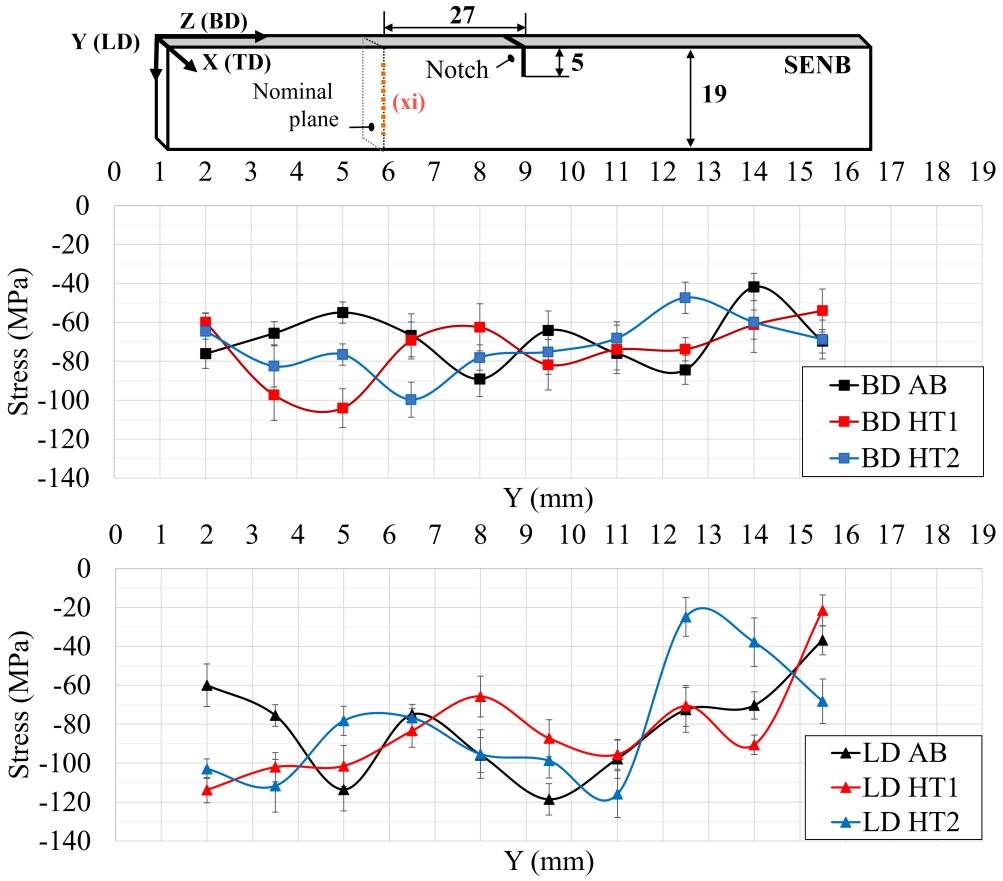

Figure 4.7.: Near-surface RS before and after heat treatment (HT1: 265°C for 1 h and HT2: 300°C for 2 h) along a line (xi) at 27 mm from the notch plane in the BD (top) and LD (bottom).

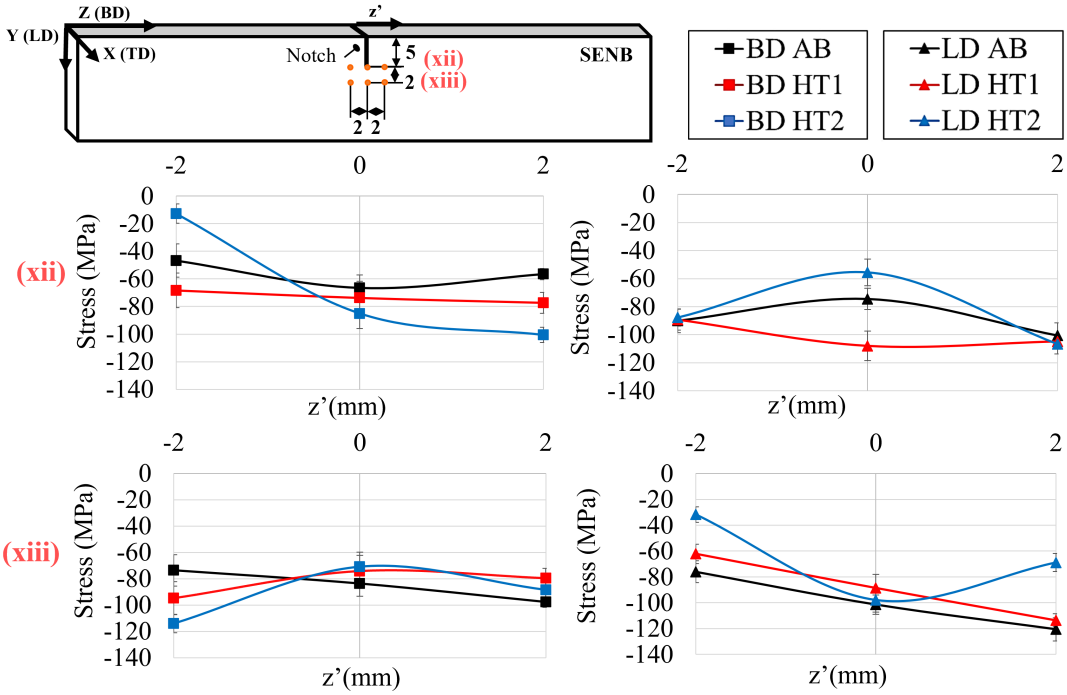

Figure 4.8.: Near-surface RS before and after heat treatment on some points ahead of the notch tip (lines (xii) and (xiii)) in the BD (top) and LD (bottom).

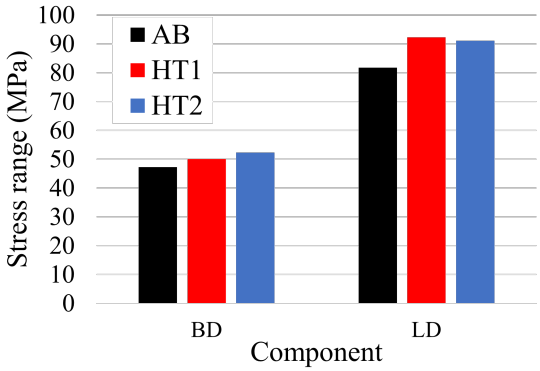

Figure 4.9.: Near-surface RS ranges before and after heat treatment: difference between maximum and minimum value measured in the profiles in Figure 4.7.

4.3.2. Stress-free reference d_0

When the bulk RS of the material is probed, as in case of ND and SXRD, a stress-free reference must be used for the strain calculation. Obtaining a reliable measure of d_0 is, however, often not trivial, and the calculated RS are sensitive to this parameter.

Neutron diffraction d_0

The stress-free reference variation over the cross-section in the as-built condition was measured using nine coupons of the grid described in Chapter 3.3.5, namely A-D-G-H-K-N-O-R-U. The LD component was measured only in three coupons (H-K-N). The spatial variation of d_0-spacing along LD in the BD, TD and LD components is shown in Figure 4.10. A slight anisotropy between the BD and the other two components is observed: the average d_0 in the BD is equal to 1.21386 $\pm$ 0.00006 Å, higher than the value measured in the TD and LD (1.213376 $\pm$ 0.00006 Å and 1.213396 $\pm$ 0.00006 Å, respectively, and therefore considered equal). As shown in Figure 4.2e, the grain growth is preferentially aligned with the BD, resulting in a <100> // BD fibre texture. This morphological and crystallographic anisotropy in the BD is reflected in the lattice spacing: the magnitude of the BD component is higher compared to LD and TD. As the difference between the components in percentage is negligible, lower than 0.05%, d_0 is calculated as the arithmetic average of the three orthogonal directions [150–153]. The d_0-spacing obtained averaging all the measurements in all three main directions is d_0 = 1.2135 $\pm$ 0.0005 Å. The d_0 variability on the cross-section corresponds to a maximum stress variation of about $\pm$20 MPa.
The variability on the cross-section for the TD component is represented in a contour plot in Figure 4.11b. Interestingly, if the pattern is compared with the distribution of pores (see Figure 4.11c), a correlation can be observed. The density of defects is higher close to the contour layer, on the top part of the grid (coupons A-D-G) and, more markedly, at the bottom (coupons O-R-U), where the d_0-spacing is also smaller compared to the central line (H-K-N). Thus, a higher content of porosity, in addition to a composition spatial variation, are suspected to jointly affect the d_0 values. The effects of porosity cannot be decoupled from the chemical variations in the cross-section. The complex PBF-LB/M process can likely lead to local variations of the chemical composition within the same component (e.g., light elements like Mg that are susceptible to evaporation [153, 154]). The cooling rates are dependent on the position toward the centre of the melt pool, the distance from the building platform and from the edges of the part [39], as well as the direction in which the inert gas flows during the building process [155]. This leads to an inhomogeneous material solidification. More in detail regarding Al-Si alloys, the supersaturation of the Si atoms in the Al-matrix depends on the cooling rates: faster cooling rates retain a higher percentage

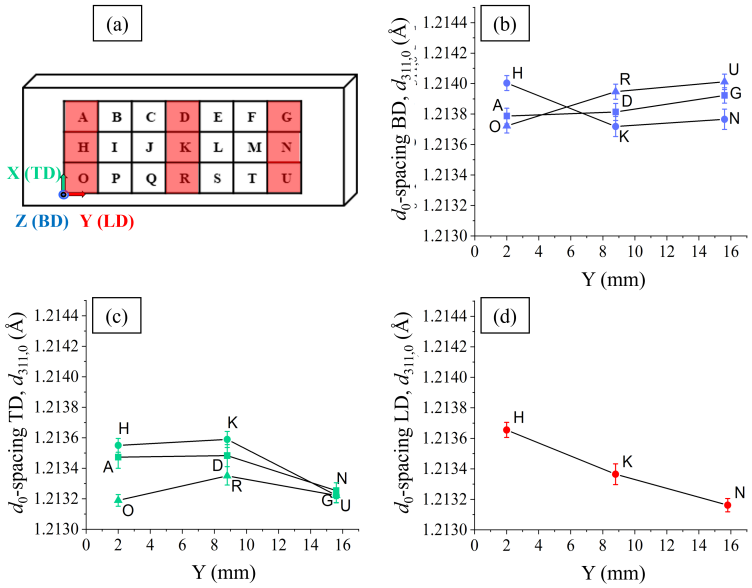

Figure 4.10.: d_0-spacing against the position along the Y-axis for the (a) measured coupons, highlighted in red. The measurements are performed in the (b) BD, (c) TD and (d) LD in the as-built condition.

of alloying elements in solid solution [20]. A difference in the content of Si atoms in the matrix can modify the lattice spacing leading to local differences of d_{hkl}. An additional redistribution of the silicon content is generated during re-melting and re-heating of previously solidified layers. Furthermore, while the long range macrostresses (type I) are relieved by mechanical sectioning, grain-scale and sub-grain scale intergranular stresses (type II type III) are retained [156]. For a multi-phase material as in the case of AlSi10Mg, an inhomogeneous strain partitioning between the phases due to the constraining effect of the stiffer Si phase on the more compliant Al matrix leads to interphase stresses. Thus, in addition to possible chemical variations and porosity effects, these micro-residual stresses can also contribute to the observed scatter.
Secondarily, d_0 was obtained by applying boundary conditions at the notch: a line containing the notch (5 points measured along the line) was measured and the weighted average according to Equation 3.10 was considered as stress-free reference. Using this method d_0 was calculated for the as-built and HT1 conditions: 1.2132 $\pm$ 0.0002 Å and 1.2134 $\pm$ 0.0007 Å respectively. The values of d_0 for ND measurements obtained with the two strategies (coupons and boundary condition) are compared in Table 4.3. The relative

error between the two estimated values is negligible, lower than 0.03%. Interestingly, HT1 seems to have a marginal effect on d_0.

Other boundary conditions can be exploited in order to arbitrate on the most reliable d_0

Table 4.3.: Results of stress-free reference d_0 measured with ND for the AB and HT1 conditions.

Condition	d_0 strategy	d_0-spacing (Å)			Mean d_0-spacing value (Å)
		BD	TD	LD	
AB	Coupons	1.21386 ± 0.00006	1.21337 ± 0.00006	1.21339 ± 0.00006	1.2135 ± 0.0005
	Notch	1.21327 ± 0.00006	1.21309 ± 0.00006	1.21330 ± 0.00006	1.2132 ± 0.0002
HT1	Notch	1.21346 ± 0.00006	1.21285 ± 0.00006	1.21365 ± 0.00006	1.2134 ± 0.0007

value. Given the thin-plate geometry of the SENB specimens with a 6 mm thickness, it is assumed that the stress state approach an overall plane stress condition [123], therefore the TD stress should be of small magnitude [157]. This condition must be fulfilled and was therefore used to evaluate the soundness of the calculation and refine the final d_0 value. Considering this condition, a variation of up to 15 MPa from the profiles initially calculated with the measured d_0 is observed. This confirms the soundness of the obtained d_0 values, as the deviation of the results from the boundary conditions was small.

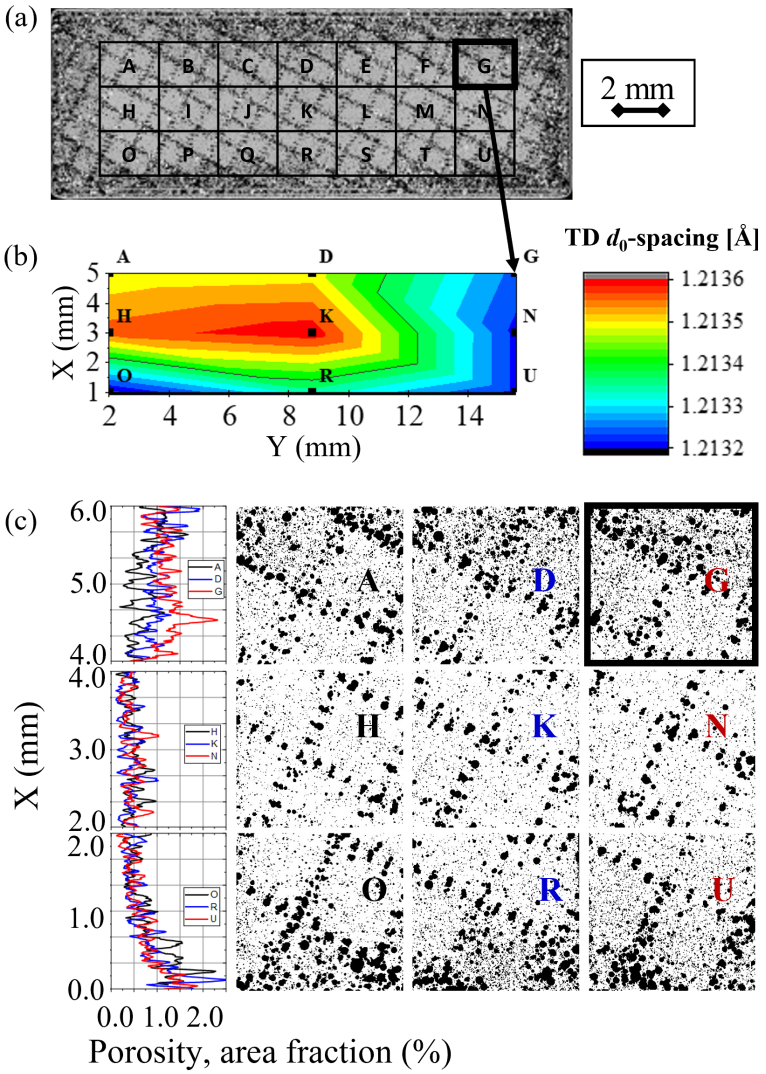

Figure 4.11.: (a) μCT projection along BD of the pores contained in the 2 mm thick coupon grid. (b) Contour plot of the d_0-spacing in the cross-section in the TD measured by ND in the as-built condition. The average error is $\pm$ 0.00006 Å. (c) Enlargement of (a) for the nine measured coupons with the respective porosity area fraction (left, in graph).

Synchrotron X-ray diffraction d_0

The methods described for ND (coupons and boundary condition at the notch faces) were also adopted for the evaluation of the stress-free reference d_0 for the aluminium {311} diffraction peak measurements performed by SXRD.
Considering the negligible spatial variations of d_0 in the cross-section measured by ND, in this later experiment, as described in Chapter 3.3.5, the grid of coupons was split and investigated in different heat treated conditions.
The contour plot in Figure 4.12 shows the spatial variation in the cross-section of the TD component after performing the different HTs. In this figure the coupons K-L-M are in the AB condition, H-I-J underwent HT1 and R-S-T HT2. As can be seen, the d-spacing values are uniform in the region of the grid subjected to the same heat treatment: the influence of porosity and chemical variation in these measurements is negligible compared to the lattice parameter changes induced by HT. Nevertheless, although appreciable in the figure, this HT-induced variation is very low in percentage.
Secondarily, 4 points on a line containing the notch were measured in all the three

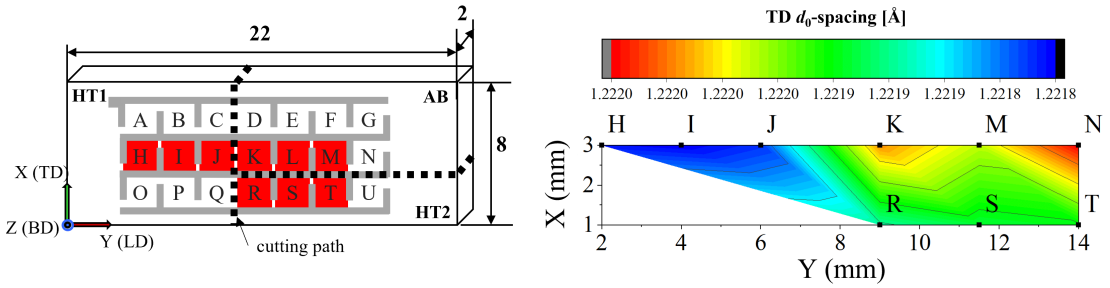

Figure 4.12.: Contour plot of the d_0-spacing in the cross-section measured by SXRD in the TD. The coupons underwent different heat treatments as shown on the left scheme: coupons K-L-M are in the AB condition, H-I-J underwent HT1 and R-S-T HT2.

conditions and the stress-free reference was calculated as a weighted average according to Equation 3.10. The results obtained with the two different strategies are shown in Table 4.4 for comparison. Again, the values obtained with the two strategies are in agreement (the maximum difference is lower than 0.04%) and a negligible change in d_0 is observed after heat treatment.
In parallel to the Al {311}, to investigate the Al/Si interphase stress, a stress-free reference for the Si {311} was necessary. The resulting values of d_0 obtained by powder diffraction

are reported in Table 4.4 and compared with the values measure from the coupons (where the interphase stress can still be retained).

Also for SXRD measurements, the d_0 resulting from the notch boundary condition was

Table 4.4.: Results of stress-free reference d_0 measured with SXRD for the AB, HT1 and HT2 conditions.

	Al {311} d_0-spacing (Å)		Si {311} d_0-spacing (Å)	
	Coupons	Notch	Powder	Coupons
AB	1.22189 $\pm$ 0.00001	1.22221 $\pm$ 0.00001	1.6417 $\pm$ 0.0001	1.6388 $\pm$ 0.0003
HT1	1.22182 $\pm$ 0.00001	1.22227 $\pm$ 0.00001	1.63894 $\pm$ 0.00008	1.6386 $\pm$ 0.0002
HT2	1.22192 $\pm$ 0.00001	1.22209 $\pm$ 0.00001	1.6383 $\pm$ 0.0001	1.63703 $\pm$ 0.00009

used. Also in this case, other boundary conditions can be exploited in order to reliably set the d_0 value. At the specimen surfaces a plane stress condition must be met, therefore the global LD component (calculated with equation 3.7) should tend to zero as it approaches the free lateral surface. This boundary condition was exploited to adjust the final results leading to a shift in the profiles of up to 10 MPa from the initial profiles obtained with the calculated d_0. This confirms the soundness of the obtained d_0 values.

4.3.3. Neutron Diffraction

The profiles of all the stress components along lines (i)-within the notch plane and (ii)-in the nominal plane (see Figure 3.9) for the as-built and HT1 conditions are given in Figure 4.13. In spite of some marked fluctuations (e.g., BD component at Y = 15 mm), the RS in the as-built condition tends to be tensile, with magnitudes close to 25 MPa in the notch field and close to 20 MPa in the nominal field. HT1 mainly results in a shift to lower values of the stresses reaching a compression state in the centre of the plane (-20 MPa at Y = 10-12 mm). In the HT condition, the influence of the notch is more pronounced: in the vicinity of the notch the stresses are tensile and become compressive moving away from it. On the contrary, for the AB condition, the stresses remain tensile across the whole notch field.
In accordance with the literature concerning specimens produced with a chessboard scanning strategy, contour layer and high temperature (200 °C) of the building platform [33, 43, 45], the calculated as-built ND RS are low (maximum values of 60 MPa).

Although differences in the profiles of all stress components before and after heat treatment can be observed, the stress ranges (Figure 4.14) are not significantly affected by the heat treatment. However, the very fluctuating nature of the results makes interpretation difficult: the large scatter observed along the profiles is also one of the reasons why such high values of stress ranges are obtained. This could therefore give rise to a biased interpretation of the results. The TD component can be considered as an indicator of the impact of the measured scatter on the stress range calculation: in this component the RS should be around zero and constant along the entire profile, but instead shows fluctuations that generate a stress range up to 80 MPa.

The measurements through the thickness of the specimens (line (iii) and (iv)) shown in Figure 4.15 also exhibit large scatter, which makes their interpretation challenging. Although a bathtub curve profile is expected, constant in the bulk and approaching zero at the free-surface, a large variation is observed from the stress range measurements, with differences between the maximum and minimum value up to 70 MPa (see Figure 4.14).

In this regard, these fluctuations, which, albeit to a lesser extent, are also found in the results obtained by EDXRD (see Figure 4.7 and 4.8), have a periodicity that it is considered not compatible with the nanoscale (e.g., compositional variation affecting d_0 spacing typically occur as a spatial gradient rather than as a scatter), the microscale (e.g., silicon network arm spacing ≈100 nm and aluminium cells ≈1 μm) or mesoscale (e.g., melting pool width ≈100 μm) features.
Additionally, this scatter found in the as-built condition is retained after heat treatment.

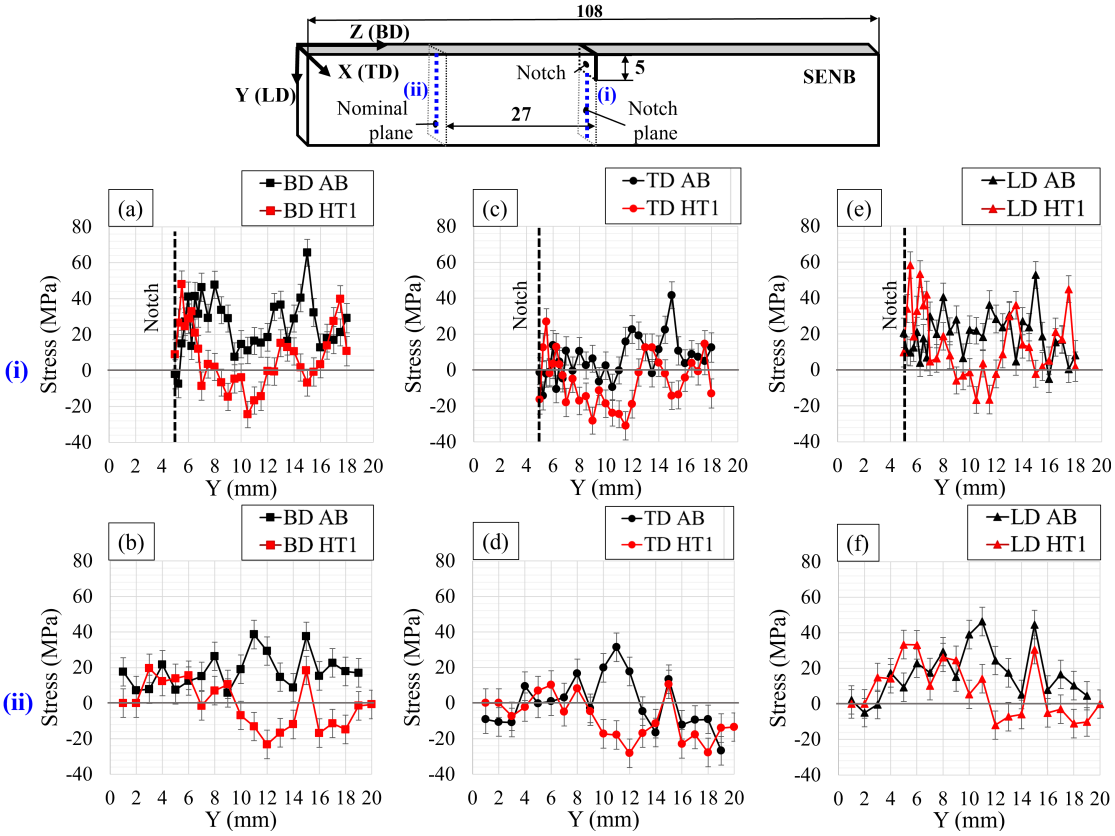

Figure 4.13.: Bulk three-axial RS profiles before and after heat treatment (HT1) in the notch plane for the (a) BD, (c) TD and (e) LD and in a plane at 27 mm from the notch (defined as nominal plane) for the (b) BD, (d) TD and (f) LD.

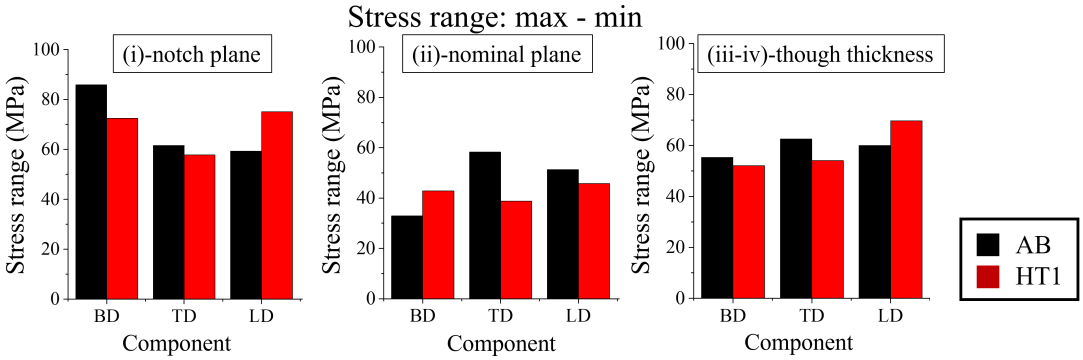

Figure 4.14.: Bulk RS ranges before and after HT1: difference between maximum and minimum value measured in the profiles in Figure 4.13 and 4.15.

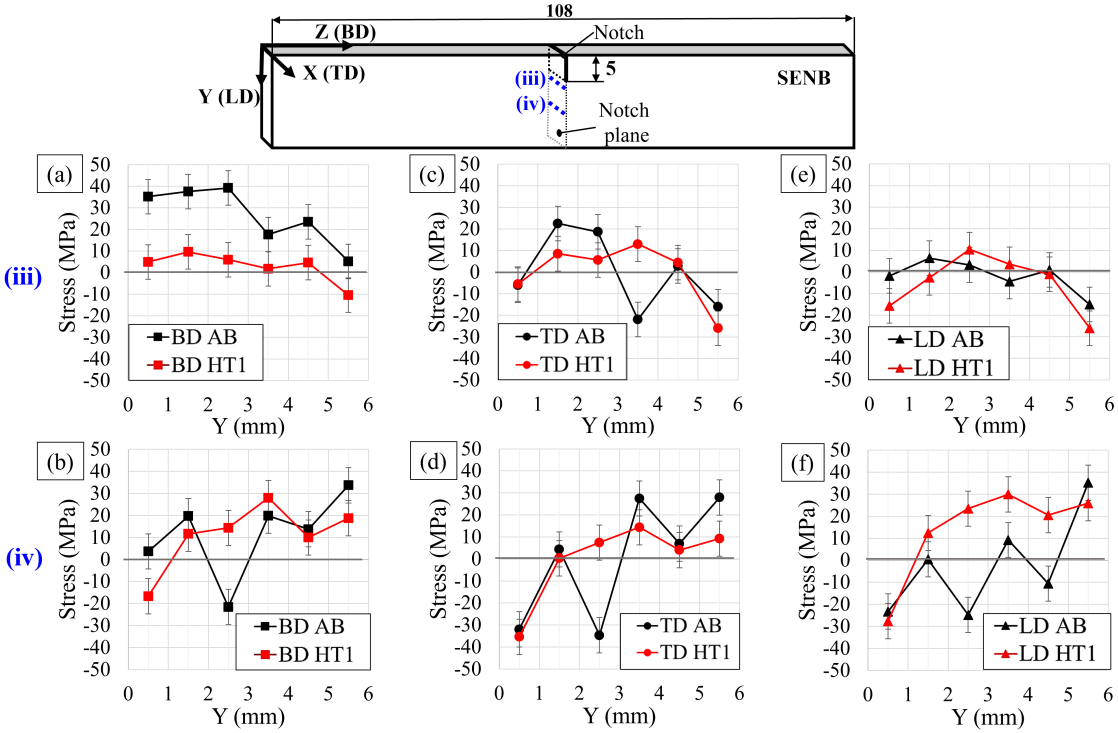

Figure 4.15.: Bulk three-axial RS profiles before and after heat treatment (HT1) in the notch plane along the thickness of the SENB specimen at 1 mm for the (a) BD, (c) TD and (e) LD and 7 mm from the notch tip for the (b) BD, (d) TD and (f) LD.

4.3.4. Synchrotron X-ray Diffraction

The measurements performed by ND in a central line in the notch plane (i) were repeated by means of SXRD (line referred to as line (v) in Figure 3.9). The results are shown in Figure 4.16 for the Al {311} and the Si {311} diffraction in the AB (black), HT1 (red) and HT2 (blue) conditions. The two lines in the notch plane at 1.5 mm from the surface, (vi) and (vii), show a similar trend and are reported in Appendix C.
The Si {220} was also measured but, as referred to be affected by the intergranular stress was not used for the calculation. The results are shown in Appendix E.
Moving away from the zone affected by the notch (Y>8 mm), the stress profiles are flat with an average value in the BD of 53 MPa in the AB condition, 23 MPa after HT1, and 40 MPa after HT2. The measurements confirm a shift to lower values of the aluminium matrix after HT1, although in this case the entire stress profile is found to be tensile. No marked fluctuations as previously observed with ND are present, which facilitates the interpretation of the results.
The silicon phase shows a similar trend with a reverse sign: away from the notch and the free-surface, where the stresses tend to zero, the stress profiles are flat with an average value for the BD of -495 MPa in the AB condition, -255 MPa after HT1, and -315 MPa after HT2. Interestingly HT2, which leads to the eutectic network breakdown and spheroidisation, appears to induce a higher state of compression on silicon particles and tension on the aluminium matrix compared to HT1. A similar evolution is found for the LD: relatively low tensile values for the Al matrix and high compressive for the Si, where the HT2 induces a higher compression of the Si phase than the HT1.
Note that an inclusion or a defect in the material is thought to cause the sharp peak observed in the AB specimen at Y≈10 mm, which also shows a high error in the measurement.

To better understand the effect of the heat treatments on the RS state, in Figure 4.17 and 4.18 the stress profiles and ranges are reported for the different heat treatments and compared with the results previously found by ND. Comparing the stress profiles in the BD (Figure 4.17a), a shift between the ND and SXRD profiles of approximately 20 MPa can be observed, whereas for LD (Figure 4.17b), the flat profiles measured by SXRD are approximately the average of the fluctuating values obtained by ND. Considering both the ND and SXRD profiles and the SXRD stress ranges, devoid of the scatter found in those of ND, it can be concluded that the two heat treatments lead to a global reduction of the stresses. The heat treatment at 265°C (HT1), with the consequent rejection of the silicon from the supersaturated aluminium matrix, brings to a relaxation of the stresses in the aluminium matrix (≈-60%) and in the retained eutectic silicon network (≈-50%). The breakdown of the Si networks with a resulting uniform distribution of micrometric Si

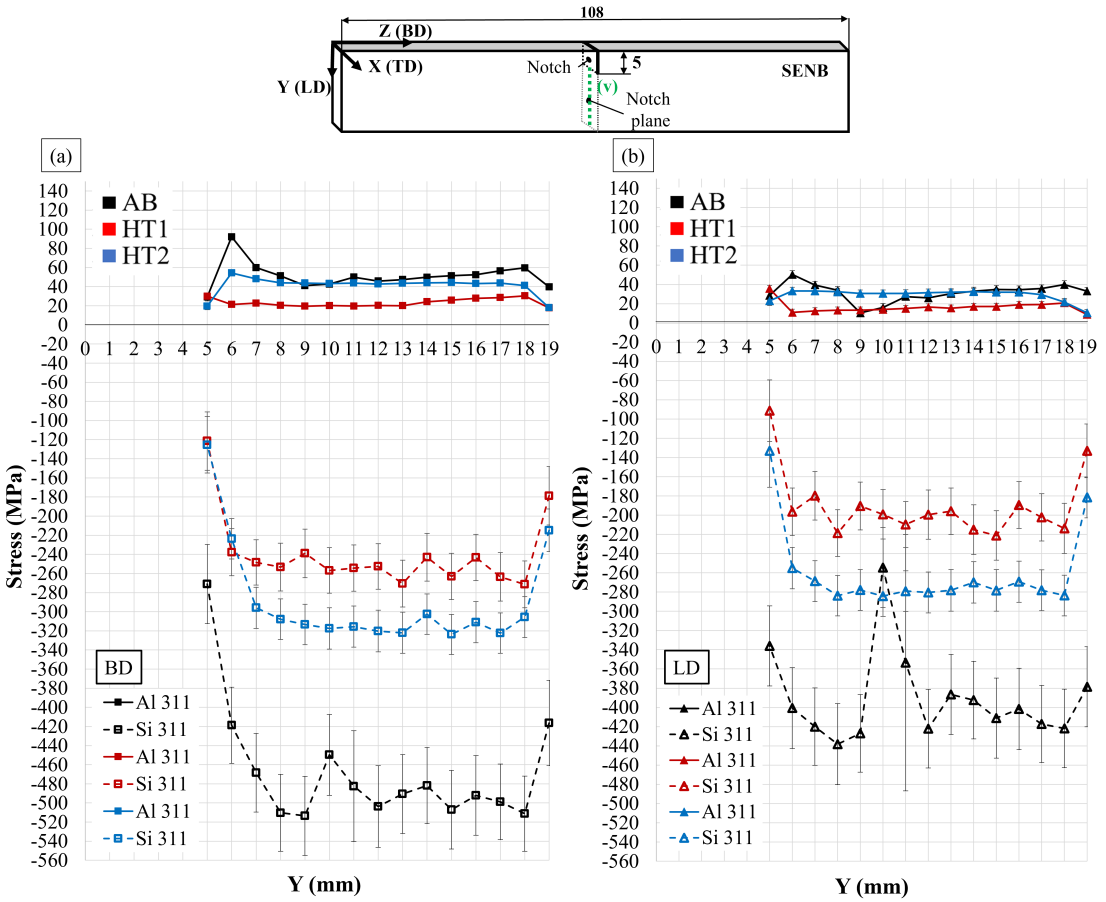

Figure 4.16.: Bulk RS profiles before and after heat treatment in the notch plane for the (a) BD and (b) LD. The results are reported for the Al {311} and the Si {311} peaks in the AB (black), HT1 (red) and HT2 (blue) conditions.

particles, which occurs with the heat treatment at 300°C (HT2), appears to result in a return to higher stresses, particularly on the matrix. In fact, after HT2 a reduction of the RS with respect to the as-built condition of ≈-25% in the matrix and ≈-35% in the silicon phase is measured. Modifications in the Si phase morphology therefore induce changes in the RS state. It is considered that the investigated heat treatment causes a repartition of the stresses between silicon and aluminium, that would occur concurrently with the relaxation of Type I RS.

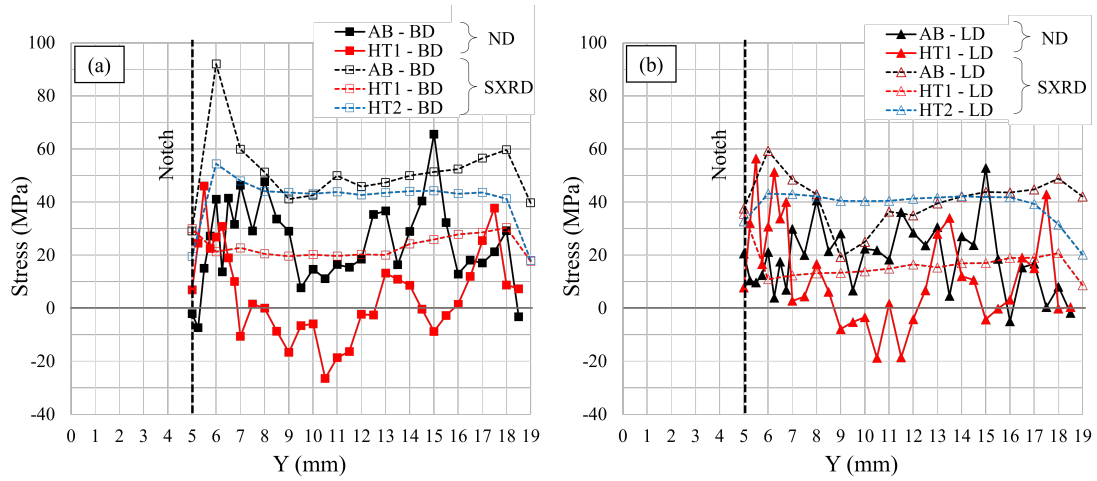

Figure 4.17.: Comparison between the ND (solid lines) and SXRD (dashed lines) profiles measured in the notch plane. The profiles are shown in the AB (black), HT1 (red) and (HT2) conditions for the BD (on the left) and the LD (on the right).

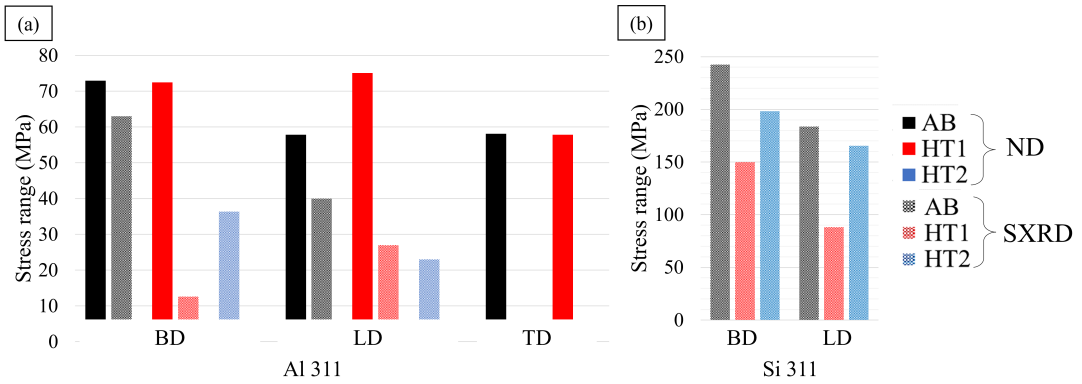

Figure 4.18.: (a) RS ranges before and after HT: difference between maximum and minimum value measured in the profiles in Figure 4.13 for the aluminium matrix and the silicon. (b) minimum, maximum and average stress value for the BD and LD components before and after HT.

4.3.5. The effect of internal voids on residual stress measurements

The fatigue crack propagation SENB specimens measured by diffraction methods, were machined from samples produced in the batch 1. The void distribution analysed by μCT in one of the tested specimens, in as-built condition, is shown in Figure 4.19. The evaluation focuses on the defects in the regions probed by the beam during diffraction RS measurements. As presented in Chapter 3.3.4, in the ND measurements the gauge volume covers an area of $\sim 2 \times 2$ mm^2 in the BD-TD plane. The ND probed region is shown in light blue in Figure 4.19b-c and the gauge volume projection is represented with a blue rectangle. Differently, for SXRD, two different volumes were probed for the BD and the LD measurements, respectively. Consequently, as shown in Figure 4.19f in light green, a different portion of volume is measured in the BD-LD plane, while a constant gauge length ($\sim$2.8 mm) in the TD is obtained (Figure 4.19e). As characteristic of synchrotron measurements, the gauge volume has a very elongated shape, whereas for neutron diffraction, a near-rectangular gauge is obtained.
Hence, the defect content in a volume similar to the one probed by the beam is projected on a 2D plane using the thick slab option provided by VGSTUDIO (Figure 4.19b-e). In this way, defects clusters are revealed (porosity is shown in black). When considering the volume probed by the beam during ND, the projection of pores in the BD (top view in Figure 4.19b) and TD (front view in Figure 4.19c) highlights a preferential zone of pore formation: the defects are aligned in $\sim$0.5 mm wide lines recurring approximately every 1 mm. This is not observed for SXRD measurements, where the volumes under investigation are shown not to coincide with regions with a high defect content (Figure 4.19e-f). It is therefore assumed that the large scatter observed is related to the presence of these pore clusters overlapping the measured volume.
Laboratory x-rays measurements are also moderately subject to fluctuations (see Figure 4.7). In this case the beam size is $\approx$ 1 mm and could partially interfere with the porosity arrangement (Figure 4.19d).

4.4. Final remarks and conclusion

The take-home-message of this investigation is that diffraction-based RS measurements are sensitive to porosity when forming clusters: variations in the defect distribution within the volume probed by the neutron beam influences the average of lattice spacing at the measured point. This can be a reason for deviations and scatter in the measurements. It is therefore important to take this effect into account when deciding upon the technique to perform RS measurements, in particular in case of AM materials, which is always

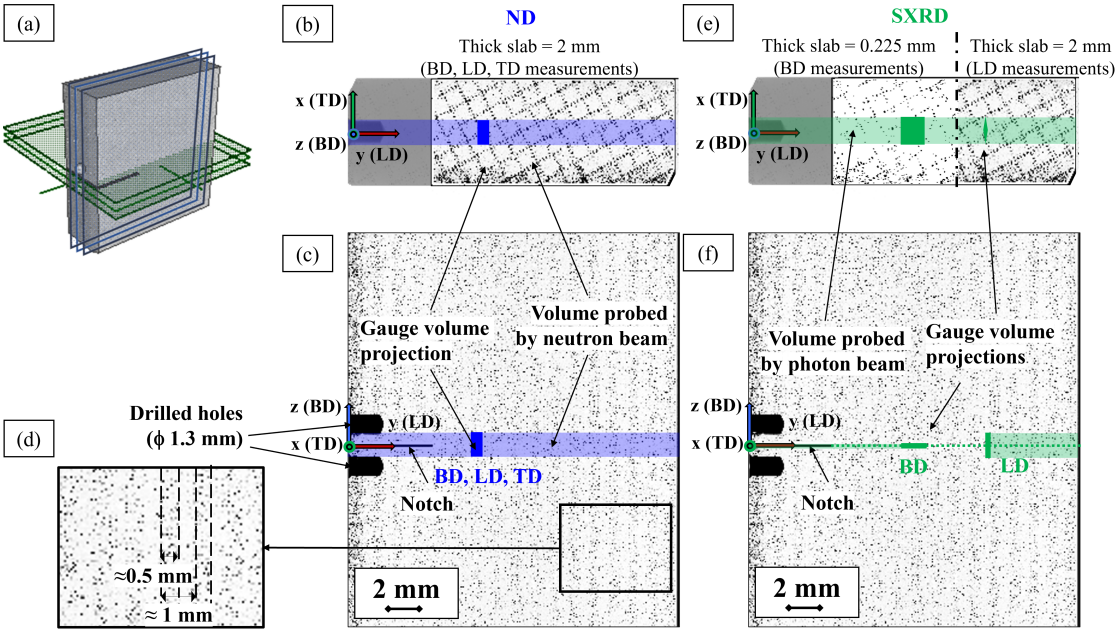

Figure 4.19.: (a) 3D rendering and orthographic projections in the BD (b,e) and TD (c,f) of a μCT reconstruction of a SENB specimen. The defect content in the volume probed by (b,c) ND and (e,f) SXRD is represented in a stack. ND: in the front view (c) all the defects in the vertical plane contained within a $\pm$1.4 mm depth from the central plane (blue planes in (a)) are projected along TD. In the top view (b) the defect content in a region of a depth $\pm$1 mm from the notch plane is projected along BD (area enclosed between the green planes in (a)). SXRD: similarly, in the front view (f) all the defects in the vertical plane contained within a $\pm$1.4 mm depth from the central plane are projected along TD. In the top view (e), since two distinguished gauge volumes were used in the measurements, the defect content in a region of a depth $\pm$1 mm (LD measurements) and of $\pm$0.112 mm from the notch plane are projected along BD.

accompanied by a high porosity content.
In this case, the SXRD, due to the shape of the gauge volume, proved to be the most suitable and reliable technique for measuring RS.
According to the results shown in this chapter, it can be concluded that the heat treatments performed have an effect in attenuating the RS. Surprisingly, HT1, which preserves the

silicon networks, has the major effect.
Secondly, the choice of a suitable d_0 for the aluminium phase is very challenging for this alloy. Possible chemical variations induced by the high content of silicon atoms in solid solution in the matrix, Al/Si interphase stresses retained after mechanical sectioning and porosity clustering complicate the stress-free reference determination. In this study, various techniques are applied and compared. In conclusion, both procedures adopted to obtain a reference value, i.e. the coupon measurements and the use of boundary conditions at the notch, proved to be sound strategies, showing good agreement with each other and with the boundary conditions. In this regard, a less laborious technique such as measuring a few points in the notch, which does not require extraction and preparation prior to measurement, proved to be an equally valid option for determining a d_0. Nevertheless, it proved important to be able to use approaches such as stress balance conditions to verify and, if needed, correct the resulting RS profiles.

5. Fatigue Crack Propagation Behaviour

Changes in microstructure, mechanical properties and residual stress (RS) state can affect the fatigue crack propagation behaviour. Herein, the influence of these modifications, discussed in the previous chapter, is investigated.
The chapter focuses on the effects in the threshold regime, as a lack of information is found in the literature for PBF-LB/M Al-Si-Mg alloys. The modifications induced by the two heat treatments (at 265°C for 1 hour (HT1) and at 300°C for 2 hours (HT2)) are investigated for the fatigue short (cyclic R-curve) and long ($\mathrm{d}a/\mathrm{d}N - \Delta K$ curve) crack growth behaviour.

5.1. Short crack growth regime

The cyclic R-curves are reported in Figure 5.1 for stress ratios equal to (a,c) -1 and (b,d) 0.1. The two models introduced in Chapter 3.4.1 are compared: the fitting curves with the model proposed by *Maierhofer et al.* [131] are shown in Figure 5.1a-b and the model by *Zerbst et at.* [130] in Figure 5.1c-d; the fitting parameters are reported in Table 5.1. The figure and the coefficient of determination R^2 shows that the curves can be described with good accuracy also by the simplified power law model. The long crack fatigue threshold $\Delta K_{\mathrm{th,LC}}$, shown in figure, was determined as the last arrest point acquired during the cyclic R-curve determination. This provides lower, and consequently conservative, estimates compared to standard K-decreasing test [158]. For AB, HT1 and HT2, respectively, the obtained values are equal to 1.4, 1.6 and 2.4 MPa$\sqrt{\mathrm{m}}$ for stress ratios R= 0.1 and to 1.7, 2.8 and 3.8 MPa$\sqrt{\mathrm{m}}$ for stress ratios R= -1. The experimentally determined intrinsic fatigue threshold value $\Delta K_{\mathrm{th,eff}}$ is between 0.9 and 1.1 MPa$\sqrt{\mathrm{m}}$.

5.2. Long crack growth regime

The $\mathrm{d}a/\mathrm{d}N - \Delta K$ curves obtained for stress ratio -1, 0.1 and 0.8 in the three different HT conditions (AB in black, HT1 in red and HT2 in blue) are shown in Figure 5.2.
As described in Chapter 3.4.1, the curves at R= -1 and 0.1 were obtained after exceeding

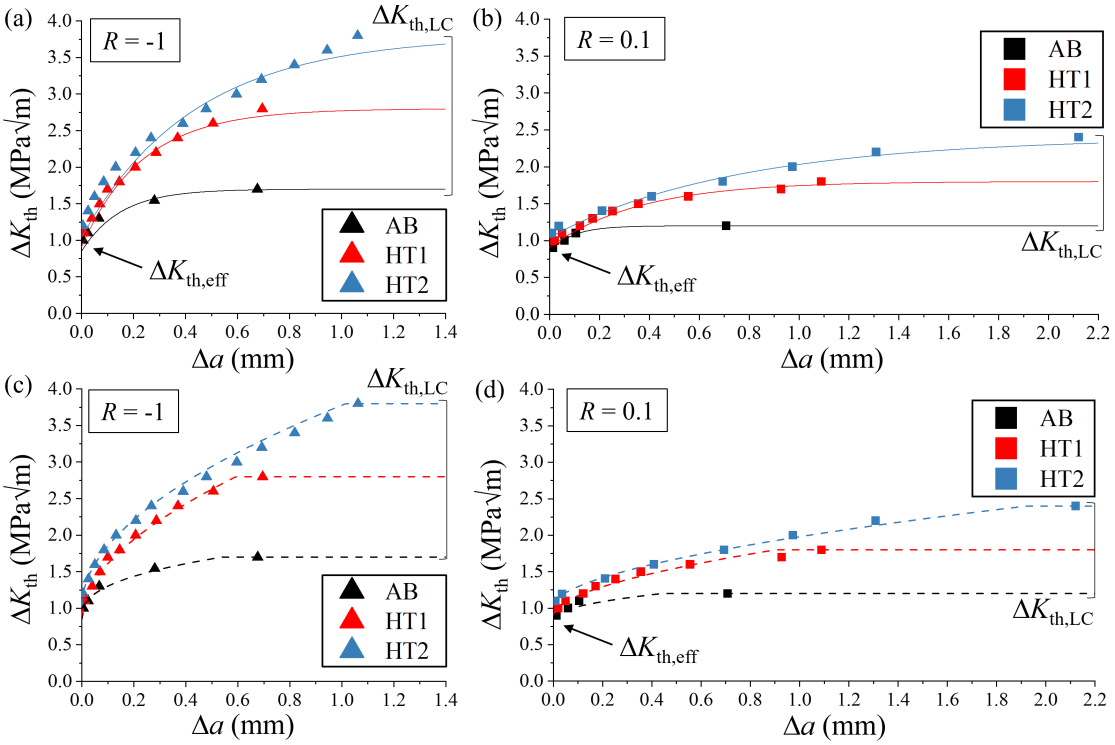

Figure 5.1.: Cyclic R-curves at stress ratio (a,c) R = -1 and (b,d) R = 0.1. Two models are used to fit the data: (a,b) the model proposed by *Maierhofer et al.* [131] and (c,d) the model proposed by *Zerbst et at.* [130].

the long crack threshold in the procedure for the cyclic R-curve determination, applying a constant force amplitude. Therefore, for clarity, the short crack propagation region is omitted from the representation, i.e., the curves start from crack growth rate of about 10^{-7} mm/cycles.

The NASGRO model introduced in Chapter 3.4.1 in Equation 3.14 was fitted to the data. The fitting parameters are reported in Table 5.2. The curves describe the near-threshold stage of the propagation, up to a crack growth rate of 10^{-5} mm/cycles. As can be observed in the upper tail of the cyclic R-curves in Figure 5.1, after heat treatment, the transition region between short and long crack, at stress ratios -1 and 0.1 is very extended. Particularly after HT2, the curves are quite steep and it seems that the long crack plateau has not yet been reached at the last point of the R-curve. Therefore, the $\mathrm{d}a/\mathrm{d}N - \Delta K$ curve is likely to be interrupted in the transition region or at the beginning of the linear

Table 5.1.: Cyclic R-curve fitting parameters.

Fitting model		*Zerbst et al.* [130]				*Maierhofer et al.* [131]				
Stress ratio, R	Condition	A	b	Δa_{LC}	R^2	l_1	l_2	ν_1	ν_2	R^2
-1	AB	0.93	0.37	0.68	0.98	0.15	0.15	0.91	0.09	0.85
	HT1	2.07	0.56	0.70	0.99	0.24	0.12	0.96	0.04	0.98
	HT2	2.73	0.53	1.00	1.00	0.45	0.22	0.95	0.05	0.96
0.1	AB	0.44	0.48	0.71	0.88	0.09	0.55	1.00	0.00	0.99
	HT1	0.99	0.56	1.09	0.98	0.36	0.36	0.96	0.04	0.97
	HT2	1.44	0.57	2.12	1.00	0.78	0.17	0.97	0.03	0.96

region (Paris' region). For this reason the n exponents obtained from the fit, may be not fully reliable to describe the Paris' region. It is noted, however, that the HT2 treatment seems to result in a steeper slope of the curve, in concurrence with the vanishing of the melting pool boundaries as observed by Santos Macías [107].

According to the standard ISO 12108:2012(E) [98, 125] the following $\Delta K_{\mathrm{th,eff}}$ were calculated at stress ratio R=0.8: 0.85 MPa$\sqrt{\mathrm{m}}$ for the AB condition, 0.91 MPa$\sqrt{\mathrm{m}}$ for HT1 and 1.04 MPa$\sqrt{\mathrm{m}}$ for HT2.

The fracture surfaces observed on post-mortem specimens, are shown in Figure 5.3 for the three conditions: (a) AB, (b) HT1 and (c) HT2. As indicated also by *Van Cauwenbergh et al.* [2] the mesostructure underwent an increased homogenisation after thermal treatment at 300°C, i.e., in Figure 5.3c, upon HT2, the melting pools are less pronounced than in the as-built condition (Figure 5.3b). As expected, HT1 does not affect the melting pool structure and a very similar morphology to as-built is preserved.

The 3D surface texture of the fracture surface is shown in Figure 5.4 for the three conditions. It is observed that in the as-built and HT1 conditions, where the Si eutectic network structure is retained, the crack mainly propagates at the melt pool boundaries. In an interconnected microstructure, the preferential path of propagation is provided by the heat affected zone (HAZ) along the boundaries between the melt pools, which are proved to be the weakest link. As already shown in the literature, the crack propagates essentially between two layers [106, 107]. After HT2, the simultaneous spheroidization of the Si network and the ripening of fine precipitates result in a more homogeneous

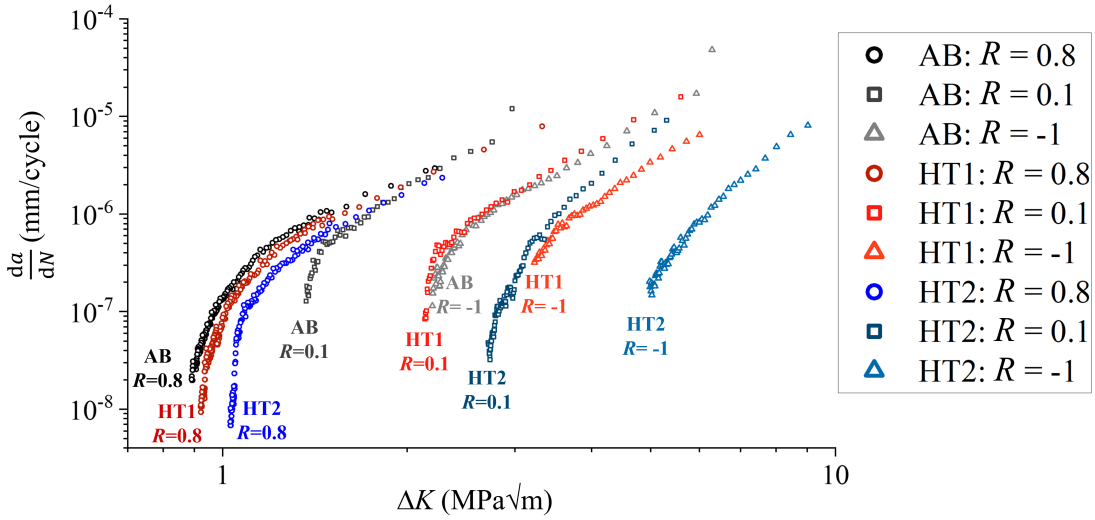

Figure 5.2.: Comparison between the $da/dN - \Delta K$ curves at stress ratio R = 0.8, 0.1 and -1 after the different heat treatments.

particle distribution, confirming a partial homogenisation of the mesostructure at 300°C. However, HT2 does not lead to a full homogenisation and crack propagation over the melt pool boundary can partially occur (Figure 5.4c).

The respective area roughness parameters are summarised in Table 5.3. A slight increase in all the areal roughness parameters is observed after heat treatment, with maximum values obtained after HT2.

Table 5.2.: Fitting parameters of the da / d$N - \Delta K$ curve (*Maierhofer et al.* [159]). For the fitting da / d$N - \Delta K$ expressed in mm/cycle and ΔK in MPa$\sqrt{\mathrm{m}}$.

Condition	R	C	n	p
AB	-1	7.8E-07	3.70	0.15
	0.1	4.4E-07	3.42	0.24
	0.8	2.0E-06	1.34	1.40
HT1	-1	2.7E-07	3.79	0.18
	0.1	8.8E-08	3.58	0.23
	0.8	9.2E-07	1.99	0.90
HT1	-1	2.7E-08	4.65	0.37
	0.1	9.1E-08	3.63	1.00
	0.8	3.7E-07	2.64	0.44

Table 5.3.: Roughness parameters of the fracture surfaces in as-built and heat-treated conditions. The measurement error is $\pm$0.01 µm.

	Sa (μm)	Sq (μm)	Sz (μm)
AB	1.74	2.34	33.49
HT1	2.08	2.80	40.84
HT2	2.37	3.09	41.68

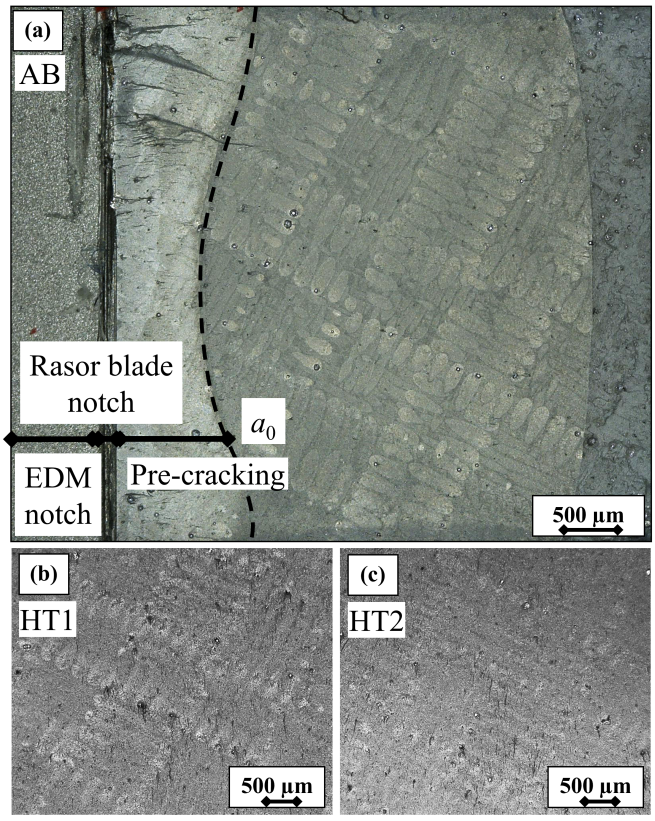

Figure 5.3.: Fracture surfaces in as-built (a) and heat-treated conditions (b) HT1 (265 °C for 1 hour) and (c) HT2 (300 °C for 2 hours) respectively. a_0 is the precrack length. Examples from tests performed for the determination of the cyclic R-curve at $R = 0.1$.

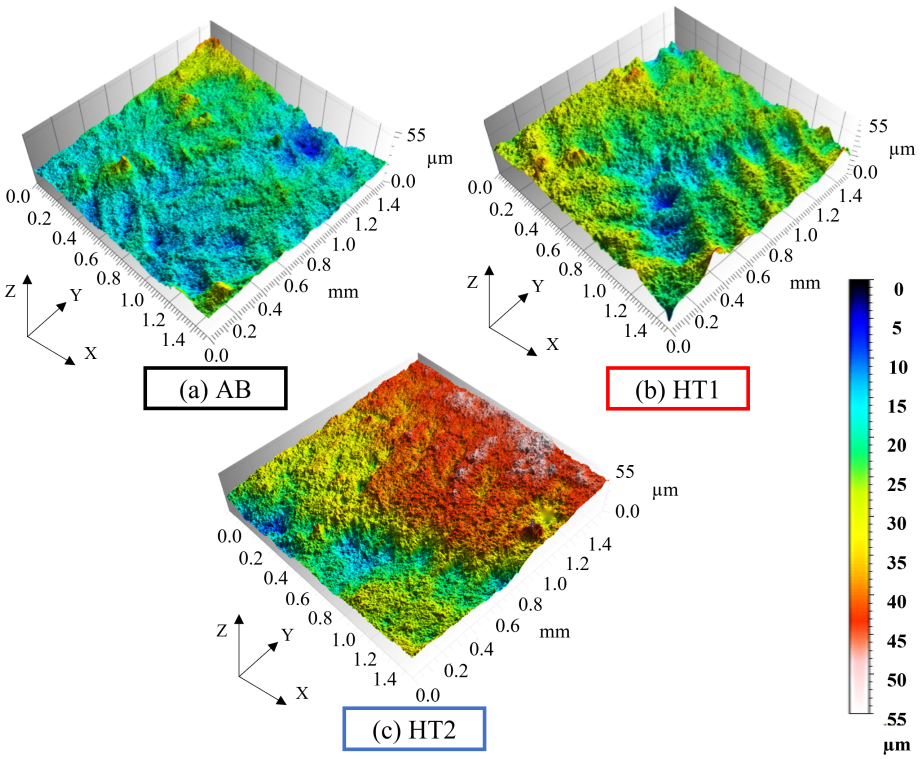

Figure 5.4.: Comparison of the 3D fracture surface roughness (a) in the as-built condition, (b) after a 265°C heat treatment for 1 hour and (c) after a 300°C heat treatment for 2 hours.

5.3. Effect of the HTs on fatigue crack propagation resistance

A significant improvement in the fatigue short and long crack propagation resistance is induced by the post-process heat treatments. This implies that the applied HTs have a significant impact on the development of the shielding extrinsic mechanisms, such as closure phenomena.
At stress ratio -1, where the closure effects are more pronounced, $\Delta K_{\text{th,LC}}$ increases by more than 60% and 120% after HT1 and HT2, respectively. At stress ratio R=0.8, the effects of the closure are very small and consequently the difference between the $\mathrm{d}a/\mathrm{d}N - \Delta K$ curves in the different conditions is minimised as $\Delta K_{\text{th,LC}} \approx \Delta K_{\text{th,eff}}$, the material dependent intrinsic threshold. Since $\Delta K_{\text{th,eff}}$ has been proven to be unaffected by the microstructure and yield strength modifications, these differences could still be due to a minimal effect of the contact shielding, as also observed, even at stress ratios higher than 0.7, by *Schmidt and Paris* [160], *Pippan* [102], *Lee* [102] and *Lados* [161]. In this regard, Table 5.4, which summarised the experimental $\Delta K_{\text{th,eff}}$ values, shows a slight increase in the threshold as the incidence of closure phenomena increases (decrease in R and heat treatment temperature).

Table 5.4.: Summary of the experimentally determined effective threshold of fatigue crack propagation $\Delta K_{\text{th,eff}}$ for all the performed tests.

HT condition	Stress ratio, R		
	0.8	0.1	-1
AB	0.85	0.90	1.00
HT1	0.91	1.00	1.10
HT2	1.04	1.10	1.20

To better understand the nature of closure phenomena, the $\mathrm{d}a/\mathrm{d}N - \Delta K$ curves of Figure 5.2 can be redrawn considering a crack closure-corrected effective stress intensity factor range $\Delta K_{\mathbf{eff}}$, as presented in Chapter 3.4.1, which takes into account the plasticity-induced component of closure. The effective stress intensity factor was calculated as $\Delta K_{\mathbf{eff}} = U \cdot \Delta K$, using the U values reported in Table 3.3. The resulting $\mathrm{d}a/\mathrm{d}N - \Delta K_{\mathbf{eff}}$ curves are plotted in Figure 5.5. As can be seen, the curves tend to move closer in the Paris regime, where plasticity-induced crack closure is prevalent, without, however, an overlapping. In the threshold regime, the data shows the greatest fanning, due to additional closure phenomena (e.g., roughness-induced) not considered in the correction.

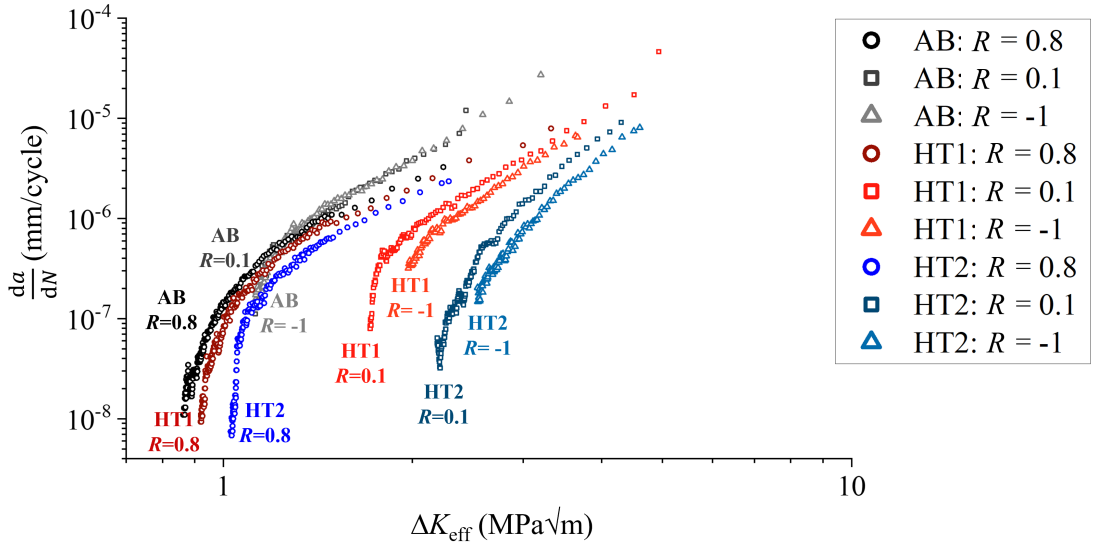

Figure 5.5.: Comparison between the $da/dN - \Delta K_{\mathbf{eff}}$ curves at stress ratio R = 0.8, 0.1 and -1 after the different heat treatments.

Key mechanisms, which could induce an increase in the crack propagation resistance under the conditions studied, are considered to be plasticity-, roughness- and RS-induced crack closure.
The contribution of the oxide-induced crack closure is neglected, as a negligible build-up of oxide debris was observed on the fracture surface. In addition, no differences on the fracture surface are found among the various HTs. Cracks can also interact with the porosity, which provides a favourable path for crack growth. Nevertheless, the interaction is more significant at high ΔK, where the large plastic zone can more likely embed these microstructure features. Furthermore the porosity content in the tested samples is analogous, thus its contribution is considered equivalent in all the examined conditions. As stated above, the discussion is restricted to the threshold region, as the data obtained in this study are not adequate to appropriately describe the linear (Paris) region of the $da/dN - \Delta K$ curves. The contribution of the aforementioned mechanisms, deemed responsible for the observed improvement in resistance, are schematically depicted in Figure 5.6 and further discussed in what follows.

Plasticity-induced crack closure The major contribution to the crack shielding is likely to be plasticity-induced crack closure. As can also be seen in Figure 5.5, by applying a plas-

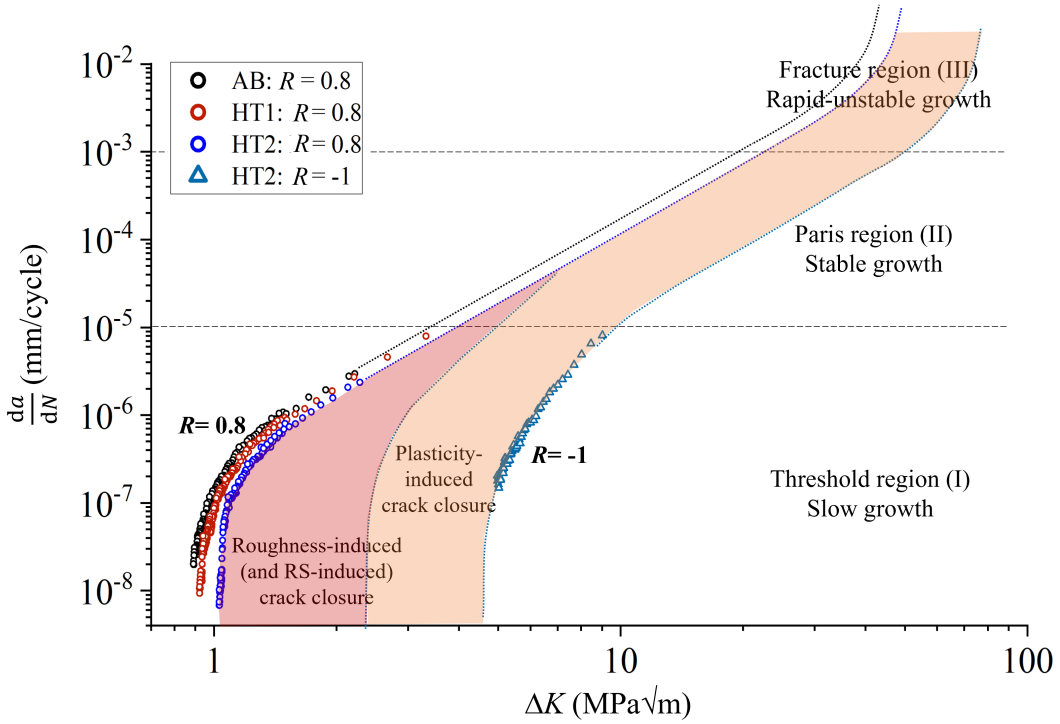

Figure 5.6.: Schematic of the contribution of the plasticity- and roughness-induced shielding mechanisms as a function of ΔK. As an example, the curves at R=0.8 (negligible closure effects) and R=-1 (maximum closure effect) for HT2 are compared.

ticity correction, the gap between the curves are considerably reduced. The phenomenon originates from the plastically stretched material that remains at the crack surfaces in the wake of the crack during the propagation [162]. The plastic deformation causes a geometrical mismatch, thus opposite crack surfaces do not fit precisely. As a consequence, just a fraction of the applied ΔK contributes to fatigue crack propagation.
As confirmed by hardness and nanohardness measurements, the heat treatments increase the ductility of the aluminium matrix. A reduction of the 8 and 20% in the hardness is observed after HT1 and HT2, respectively. The enhanced ductility is observed also comparing the stress-strain curves in Chapter 4.2: the elongation at break doubled after HT1 and tripled after HT2. Thus, the HT1 and, particularly, the HT2 material is expected

to lead to higher plasticity-induced crack closure.

Roughness-induced crack closure The asymmetric in-plane and out-of-plane displacements of the crack flanks induced by asymmetric deformation of the plastic wake and the premature contact of the fracture surfaces caused by the misfit of the rough fracture surfaces are denoted as roughness-induced crack closure [128, 163]. This mechanism takes place mainly at near-threshold levels at low stress ratios, as schematized in Figure 5.6, when the size-scale of the fracture roughness is comparable with the crack tip opening displacement and in presence of Mode II displacements [164]. This phenomenon contributes to the threshold fanning observed in Figure 5.5.
The 3D roughness measurements reported in Table 5.3 show a slight increase of the area roughness parameters after HT, ≈+20% for HT1 and ≈+30% for HT2. An increased average (Sa) and mean roughness depth (Sz) entails a higher deviation of the surface from a mean plane. This leads to a premature contact of the fatigue fracture surfaces during the crack propagation. Higher values of the root mean square roughness (Sq) indicates a more irregular and rough surfaces. Therefore, the interference between the crack surfaces and mixed-mode loading phenomena will be the greatest for HT2.
Furthermore a higher roughness can be an indicator of the formation of branching cracks that consume energy and delay the fatigue crack growth. The phenomenon was observed by *Santos Macías et al.* after a 300°C heat treatment for 2 hours [107].

Residual stress-induced crack closure When high RS are involved, the near-threshold regime is mainly controlled by the residual stress closure phenomena (zone shielding), which override the effects of microstructure and roughness [161].
In the material studied, the selection of the process parameters, such as a 300°C preheating and a chessboard strategy, results in moderate RS levels. The residual stress state in the loading direction (BD) in the aluminium matrix of the tested specimens, assessed in Chapter 4.3, is summarised in the contour plots of Figure 5.7. The graph combines the near-surface measurement by laboratory energy-dispersive x-rays (lines at X=0 and 6 mm) with the bulk synchrotron x-rays measurements (lines at X=1.5, 3 and 4.5 mm). The RS measured on the crack plane before testing are, in all the investigated conditions, compressive at the surface and tensile in the bulk. The RS at the notch tip is tensile and similar for all the conditions. Therefore the stress the material experiences at the crack tip will be higher than the applied stress, causing the crack to grow faster. In the AB condition the stresses at the notch are slightly higher (≈40 MPa at Y=5 mm) compared to the HT1 and HT2 condition (≈30 MPa). Given the similar stress state immediately

ahead of the notch, the contribution of residual stresses to the fatigue crack propagation for the different HT conditions is comparable.
1 mm ahead of the notch, the RS increase for the AB (up to 90 MPa) and the HT2 (up to 55 MPa), while the profile remains constant (about 20 MPa) for HT1. However, the crack growth results in a redistribution of the RS, which leads to a reduction in the stress ranges (the difference between the maximum and minimum values in the profiles) that will mitigate these differences between HTs.
In addition, although HT1 gives the greatest RS relaxation, it is HT2 that performs better. This suggests that the contribution of residual stresses is marginal.

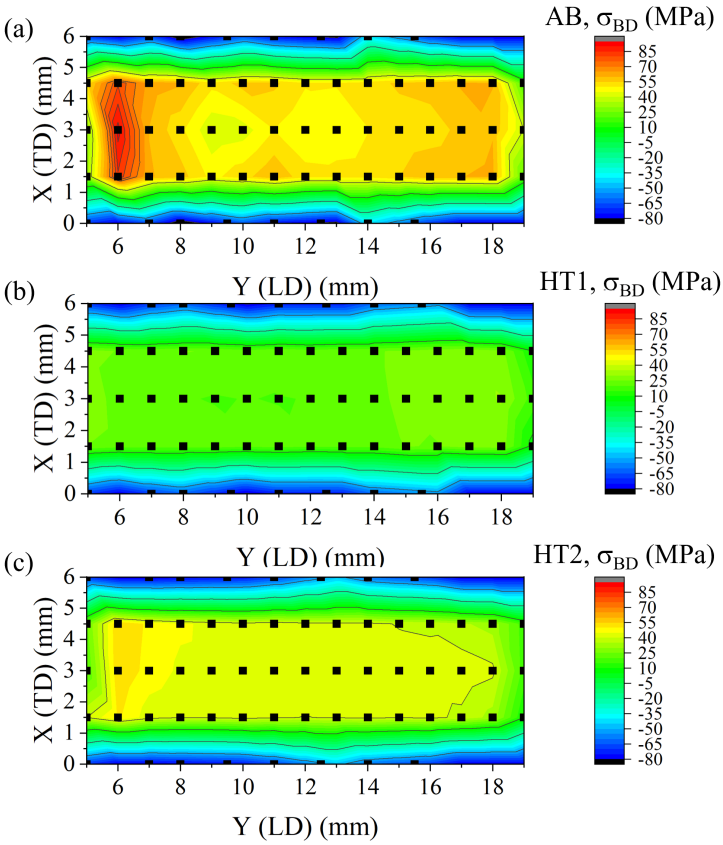

Figure 5.7.: Contour plots of the stress state in the crack plane in the loading direction (BD) before testing. The graph summarises the results from synchrotron and laboratory x-ray diffraction of Chapter 4.3 for the three studied conditions: (a) AB, (b) HT1 and (c) HT2.

5.4. Conclusion

Low temperature post-process heat treatments have been found to affect the fatigue crack propagation resistance of a PBF-LB/M AlSi10Mg alloy. The two performed heat treatments showed a significant beneficial effect on the crack growth resistance in the threshold regime. The improvement in the fatigue long crack threshold is up to 60% after HT1 and 120% after HT2. The improvement was attributed to a higher development of crack closure phenomena during crack propagation. After HT1, the aluminium matrix showed a more ductile response due to lower silicon atoms content. Nevertheless, the most ductile response was achieved with HT2, due to a fine and nearly uniform distribution of eutectic silicon particles in a soft aluminium matrix. The crack surfaces exhibited increasing roughness after HT1 and HT2 which is believed to promote premature contact and, therefore, a greater resistance to fatigue crack propagation.
In the AB and HT1 conditions, where the melting pool structure is preserved, in the case of a loading direction parallel to the building direction, the crack preferentially propagates between layers. After HT2, a gradual homogenisation of the mesostructure leads to a change in the propagation pattern: the crack follows a more tortuous path, influenced only partially by the melting pools HAZ.
The residual stresses developed at the crack tip can play a central role in the fatigue crack growth. However, in all the conditions studied, these are very similar and moderate. Therefore, RSs are not considered a determining factor in the observed differences in the crack growth.
Finally, this study integrates, adding information about the threshold (I) region, the works published by *Santos Macías et al.* [107] and *Di Giovanni* [106] on the II-III region of the fatigue crack growth curves for the PBF-LB/M AlSi10Mg. These results (at a stress ratio R=0.1) are summarised in Figure 5.8. Comparing the results obtained for HT2 (red circles) with the published data for the T6 heat treatment (black triangles) a similar performance improvement is observed.

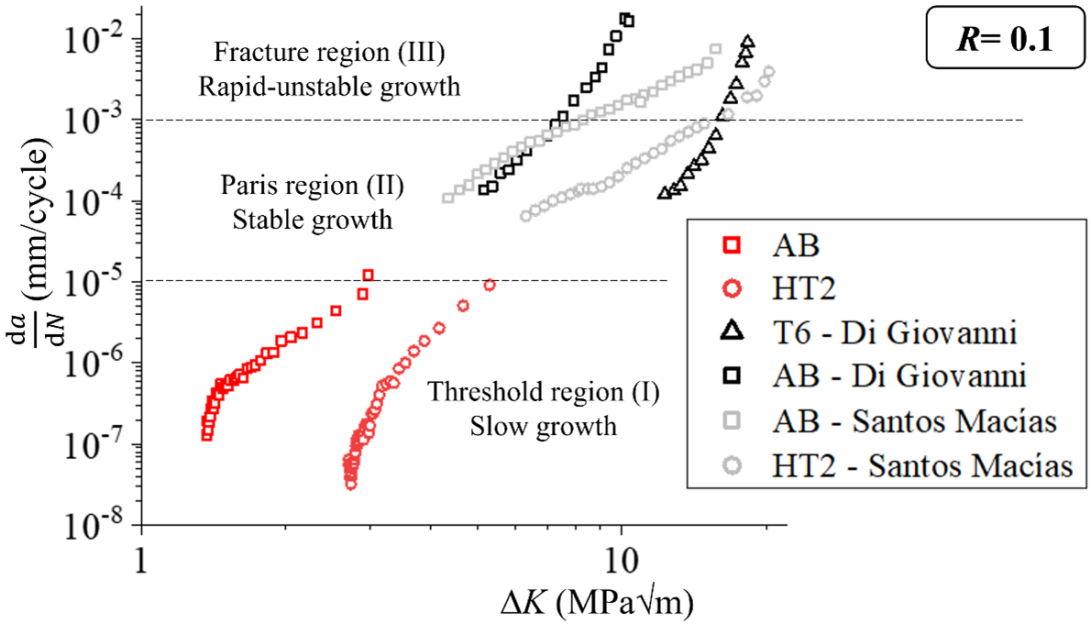

Figure 5.8.: Comparison and integration of the $\mathrm{d}a \nearrow \mathrm{d}N - \Delta K$ curves obtained at $R = 0.1$ for the AB and HT2 conditions (red squares and circles, respectively) with the data published in the literature. In black the results from *Di Giovanni* [106] for the AB (squares) and T6 (triangles) conditions. In grey the results from *Santos Macías et al.* [107] for the AB (squares) and HT2 (circles) conditions.

6. Fatigue Behaviour: Experiments and Modelling

As introduced in Chapter 2.5 and confirmed by the experimental results presented in what follows, one of the main problems related to the fatigue life description of AM parts is the large scatter of the experimental results. When the residual stresses are limited, as in the current case, defects are the main variable affecting the fatigue resistance. Therefore, the largest part of experimental scatter should be strictly related to the initial size of manufacturing defects within the material, which control the fatigue resistance. Since the individual AM specimens may contain different defect populations (porosity, lack of fusion), the fatigue limit of one series of specimens is not constant and the results cannot be expressed with one representative S-N curve.
In this chapter, different approaches from the literature are applied and compared, in order to assess the scatter from two batches with different types of defects, as well as the influence of the two low temperature heat treatments.

6.1. Cyclic stress-strain response

Axial strain-controlled incremental-step tests (IST) were performed in order to investigate the cyclic stress-strain response of the material before and after heat treatment. The stabilised stress-strain curves resulting from the tests are shown in Figure 6.1. Two specimens for each HT condition were tested. Note that the testing was restricted to the first batch. A good repeatability is observed. The Ramberg-Osgood equation (Equation 3.17) was fitted to the data. The average values obtained for the two tested specimens per condition is reported in Table 6.1.
It is observed that in the AB and HT1 conditions, where an interconnected silicon structure is retained, the material behaviour is similar, even though a moderate reduction in strength is already observed. While, as also noted in the monotonic curves, the cyclic strength reduction mainly takes place with the spheroidization of the silicon networks, after HT2.

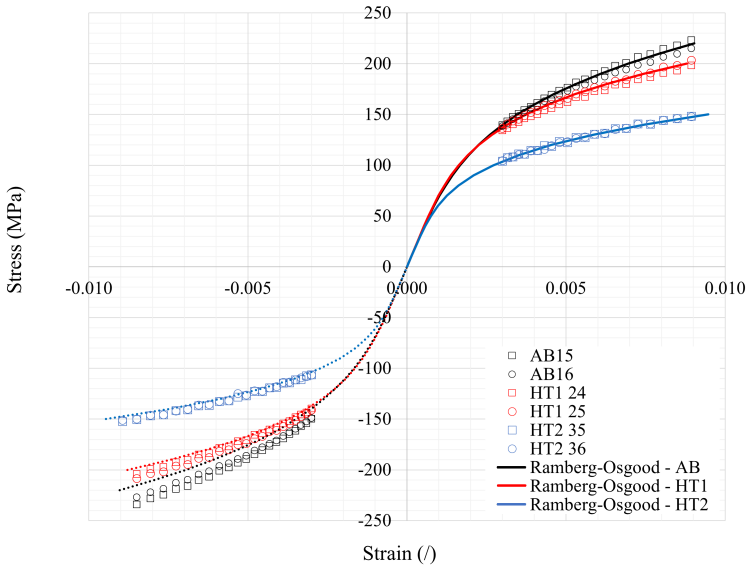

Figure 6.1.: Cyclic response of the PBF-LB/M AlSi10Mg: comparison between the stabilised stress-strain curves for the six specimens tested in AB condition (in black), after HT1 (in red) and after HT2 (in blue).

Table 6.1.: Coefficients of the Ramberg–Osgood relation fitted to the experimental stabilised cyclic curves.

HT condition	K' (MPa)	n' (/)	E (GPa)
AB	872	0.27	74.85
HT1	645.5	0.23	75.38
HT2	484	0.24	73.90

6.2. High Cycle Fatigue resistance

The results of the High Cycle Fatigue (HCF) tests on the two batches described in Chapter 4.1.2 are shown in the S-N curves in Figure 6.2. In each batch, the three heat treated conditions were tested: as-built (AB), 265°C for 1 hour (HT1) and 300°C for 2 hours (HT2). The tests in which no failure was observed within a number of cycles $N_{\mathbf{lim}} = 10^7$ (runout) are plotted with triangles.

Notwithstanding the significant improvement observed in the fatigue crack propagation

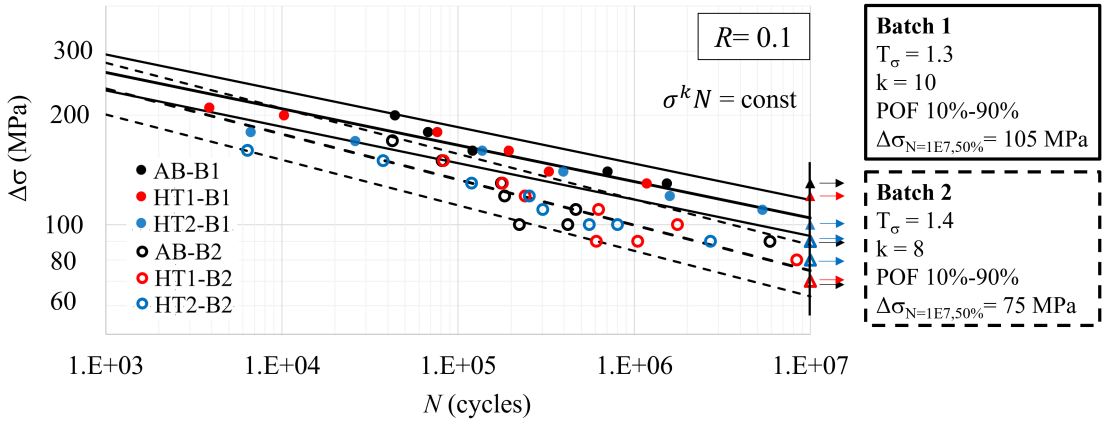

Figure 6.2.: Comparison of the S-N curves for the two batches in different heat treated conditions (as-built in black, HT1 in red and HT2 in blue). Filled symbols refer to batch 1 (B1) and empty symbols to batch 2 (B2). Full and dashed lines refer to the scatter band calculated fora a probability of failure between 10% and 90% at a confidence level of 95% for batch 1 and 2, respectively.

discussed in the previous chapter, it is noted that the heat treatments have no beneficial effect in the HCF.

This is not surprising when considering the results of the CT analyses described in Chapter 4.1.2. In this regard, hereinafter the defect size is defined by the $\sqrt{area}$ parameter, namely the square root of the projected area of the volumetric defect on a plane perpendicular to the maximum principal stress. This parameter is fundamental in the assessment of fatigue strength in metallic materials containing defects [139].

The presence of voids, porosity with a mean $\sqrt{area}$ of 75 μm in the batch 1 ad lack of fusion with a mean $\sqrt{area}$ of 195 μm in the batch 2, of a size significantly larger than the microstructural features (Al cells size < 1 μm and nanometric Si networks and particles),

overshadows the influence of the microstructure on the fatigue resistance. Therefore, it is considered that the finite life regime is not affected by the heat treatments.
The scatter band in Figure 6.2 is calculated for a probability of failure between 10% and 90% at a confidence level of 95%. In the statistical analysis, only the experimental points (N, $\Delta\sigma$) in which the specimen failure occurred at a number of cycles greater than 10^4 were used (elastic range) [135]. The results are summarised in Table 6.2.
The second batch, due to the larger size and irregular shape of the defects, generally

Table 6.2.: Statistical estimation of the S-N curve for batch 1 and 2 at a confidence level of 95% according to ISO12107:2012 [135].

	N (cycles)	$\Delta\sigma_{90\%}$ (MPa)	$\Delta\sigma_{50\%}$ (MPa)	$\Delta\sigma_{10\%}$ (MPa)
B1	1.E+04	186	208	234
	1.E+07	93	105	117
	T_σ =1.3		k = 10	
B2	1.E+04	151	178	208
	1.E+07	64	75	88
	T_σ =1.4		k = 8	

shows a lower endurance than the first batch, which contains smaller round pores. The stress amplitude $\Delta\sigma_{50\%}$ which results into a number of cycles $N = 10^7$ calculated at a probability of failure of 50% is equal to 105 MPa for B1 and 75 MPa for B2. The presence of large irregular defects not only decreases the fatigue resistance of the material, but also increases the scatter associated to the Wöhler curve [9].
The experimental parameters and the results for each test are summarised in Appendix C. The results shown are in agreement with the literature, summarised in the Chapter 2.5.2, Figure 2.5a. The wide scatter of the results shows how dependent the outcome is on the process parameters and its repeatability, which determine the defect population in the material and thus the fatigue strength.

6.2.1. Defects at the fracture origin

The fracture surface of each specimen was analysed after the fatigue failure. Some representative images are shown in Figure 6.3 for the two batches in different HT conditions. It is observed that the crack always originated from a surface or near-surface defect.

The area of the defect at the origin of failure (killer defect) was measured. In Figure 6.4a the killer defect dimensions are plotted for B1, in red triangles, and B2, in black circles. As predicted by the CT data analysis reported in Chapter 4.1.2, the killer defects in batch 1 are round pores. The sample mean value of $\sqrt{area}$ is 70 μm and the standard deviation of the population σ=12 μm is low: all the specimens in the batch presented a similar defect size and distribution and, consequently, the distribution of killer defects also presents a reduced scatter. Whereas, the killer defects in the second batch are lack of fusion with a mean value of $\sqrt{area}$ of 202 μm and a standard deviation about 7 times higher.

The measured values are compared with the prediction obtained from the CT data (blue squares in figure). The estimations were carried out following the procedure proposed by *Romano* [9, 10], using the Peak Over Threshold approach. For the calculation, only surface defects were considered, as they are proven to be the preferential initiation for failure. Applying an empirical rule by *Murakami* [139], a defect was classified as superficial, when the condition expressed by equation

$$\frac{a}{h} > 0.8 \tag{6.1}$$

is fulfilled. The parameter definition is clarified in Figure 6.4d: a is the radius of an equivalent circle with an area equal to the defect area and h is the distance between the defect centre and the external specimen surface. a can be calculated as $\sqrt{area/\pi}$. Additionally, it must be considered that the tested volume (gauge volume of the hourglass specimens) is greater than the volume scanned by CT. Therefore, a volume correction must be applied to the distributions. The resulting exceedances distribution can be approximated by a Gumbel distribution [10, 165]. More details on the procedure are given in Appendix B.

The obtained distributions of the maximum defects in the surface volume can be used to estimate the killer defect size. In Figure 6.5 the distributions are shown in a Gumbel probability plot and are compared with the effective distributions of the killer defects, for batch 1 (in red) and 2 (in black).

Taking into account the scatter within the second batch, the defect distributions measured on 4 different specimens were used for the estimation (values summarised in Figure 6.4d). The average killer size, $\sqrt{area}_{\mathbf{mean}}$, was calculated from the 50% percentile of the distribution with the average defect density (i.e., the distribution from specimen AB (3b)). The expected lower and upper bounds, $\sqrt{area}_{\mathbf{min}}$ and $\sqrt{area}_{\mathbf{max}}$, refer respectively to the 2.5% percentile with minimum defect density (HT2 (3b)) and 97.5% percentile with maximum

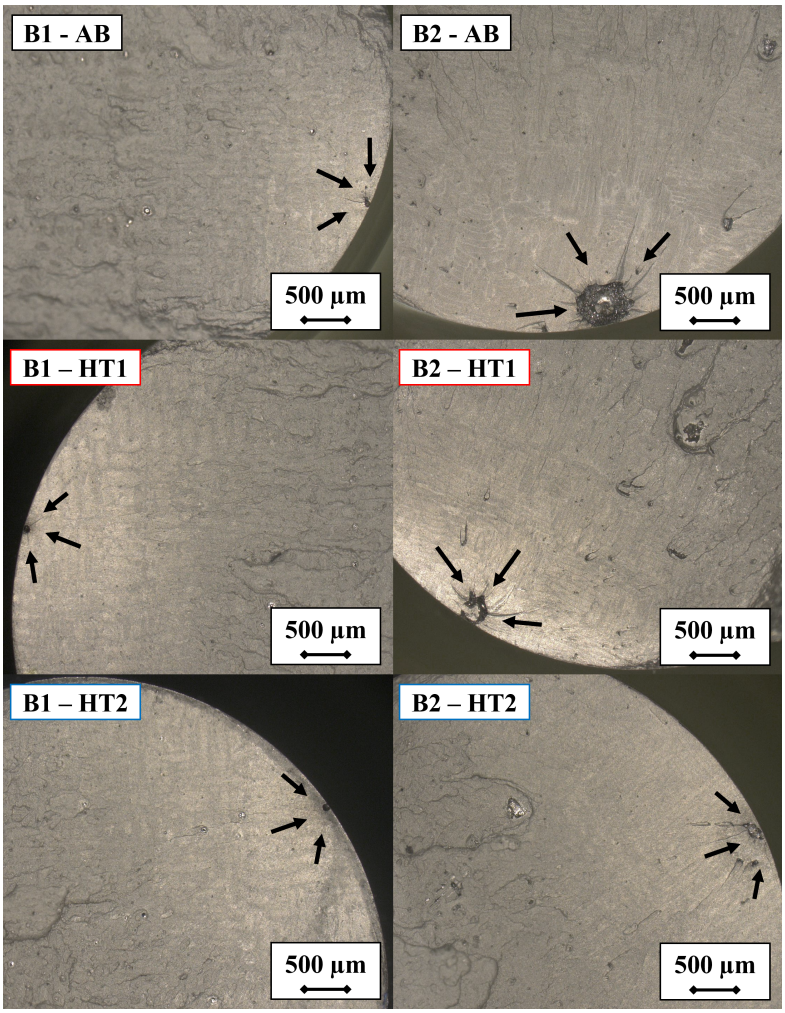

Figure 6.3.: Comparison of the fracture surfaces and the killer defects of batch 1 (left) and 2 (right).

defect density (HT1 (21b)). For batch 1, were the scatter was low, $\sqrt{area}_{\textbf{mean}}$, $\sqrt{area}_{\textbf{min}}$ and $\sqrt{area}_{\textbf{max}}$ were calculated adopting the same distribution, which is representative of the entire batch (from the specimen HT1(22)). These results are summarised and compared with the experimental results in Figure 6.4a,d.
It is noted that for B1 a conservative prediction of the killer size from the CT data is obtained adopting the statistic of extremes. Given the uniform distribution of the defects in the batch, the analysis of a single specimen provides a good and conservative estimate of the size of the killer defects. In contrast, for the second batch, the estimate of the mean killer defect size is precise but the estimation is non conservative. Given the high scatter observed in the batch, it is assumed that 4 specimens are not sufficient for a reliable estimate.

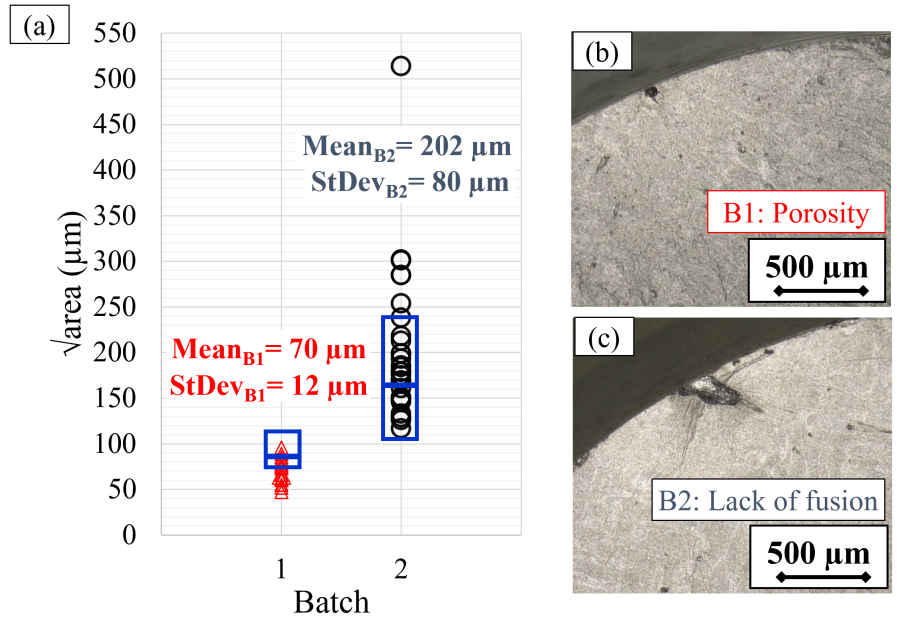

(d) **Peak Over Threshold estimation**

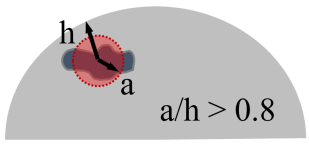

	√area$_{min}$ (µm)	**√area$_{mean}$ (µm)**	**√area$_{max}$ (µm)**
Batch 1	69	86	115
Batch 2	104	161	240

Figure 6.4.: Dimension of the killer defects in batch 1 and 2. (a) Comparison of the $\sqrt{area}$ of the measured killer defects for B1 (red triangles) and B2 (black circles) with the prediction obtained from the CT data analysis (blue squares); example of the killer defect size and shape: (b) porosity in B1 and (c) lack of fusion in B2; (d) estimation of the killer defect size with the Peak Over Threshold statistic: definition of surface defect and table with the $\sqrt{area}$ results.

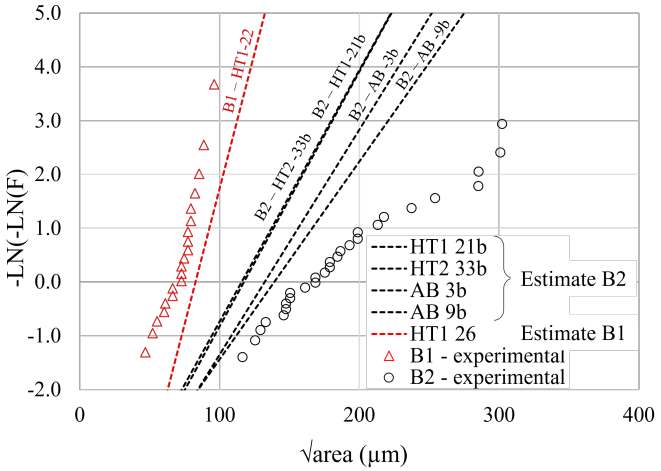

Figure 6.5.: Comparison between the estimated killer defect sizes by applying the Peak Over Threshold approach to the CT data and the measured killer defect distributions for batch 1 (in red) and 2 (in black). The estimated size distribution (dashed lines) is compared with the measured killer defects distribution (triangles for B1 and circles for B2) in a Gumbel probability plot (negative exponential). The samples measured for batch 1 are well described by HT1-22. For batch 2 four different samples are shown: AB-3b, AB-9b, HT1-21b and HT2-33b.

6.2.2. Determination of the $\Delta K - N$ curves

The scatter of fatigue strength can be reduced if data are correlated to the defect size at the failure origin [138]. A first approximation of the stress intensity factors ΔK at the tip of the defects was calculated considering the defects as elliptical cracks, as proposed by *Murakami* [139]. As described in Chapter 3.4.4, ΔK was calculated from the applied stress range $\Delta\sigma$ and the killer defect area as:

$$\Delta K = F \cdot \Delta\sigma \cdot \sqrt{\pi\sqrt{area}} \tag{6.2}$$

All the killer defects observed post mortem are located at the surface, therefore, $F = 0.65$. The results of the calculations are summarised in Appendix C in Table C.3 and C.4. The Wöhler curves of Figure 6.2 are recalculated in terms of $\Delta K - N$ in Figure 6.6. Considering the $\sqrt{area}$ of the killer defects, the wide scatter observed between the two different batches is reduced and the experimental data can be described by a single curve.

Moreover, equation 6.2 was used before testing to calculate the stress intensity factor ΔK of the defects detected by CT. In this way, it was possible to rank the defects according to their ΔK and to foresee which defect would have caused the fatigue failure. After the tests, the predictions were verified. For each tested specimen the three defects with the higher SIF are reported in Table 6.3. The prediction is robust as in every analysed specimen the killer defect was correctly predicted by CT.

Thereafter, the *short crack-corrected* stress intensity factor range by *El-Haddad, Smith and Topper* [140, 141] is calculated as described in Chapter 3.4.4 as:

$$\Delta K_{\mathbf{corr}} = \Delta\sigma \cdot \sqrt{\pi(F^2\sqrt{area} + \sqrt{area}_0)} \tag{6.3}$$

The $\sqrt{area}_0$ material parameter was estimated from the fatigue long cracks threshold $\Delta K_{\mathbf{th,LC}}$ and the fatigue limit of the flawless material $\Delta\sigma_{\mathbf{e}}$ at stress ratio R=0.1. The fatigue limit of the flawless material $\Delta\sigma_{\mathbf{e}}$ at stress ration R=-1 can be estimated from the Vickers hardness (HV) with an error band of $\pm$20% even for an aluminium alloy [139, 166] as:

$$\sigma_e = 1.6 \pm\ 0.1HV \tag{6.4}$$

The HV was measured in all the conditions and is summarised in Chapter 4.2 in Table 4.2. Since the performed tests were conducted at R=0.1, it was necessary to correct these values for a mean stress different from zero. This conversion was performed adopting the Goodman-Haigh diagram [167, 168] (see Appendix C). Moreover, a conservative value for $\Delta K_{\mathbf{th,LC}}$ was provided from the cyclic R-curves at R= 0.1 (see Chapter 5.1).

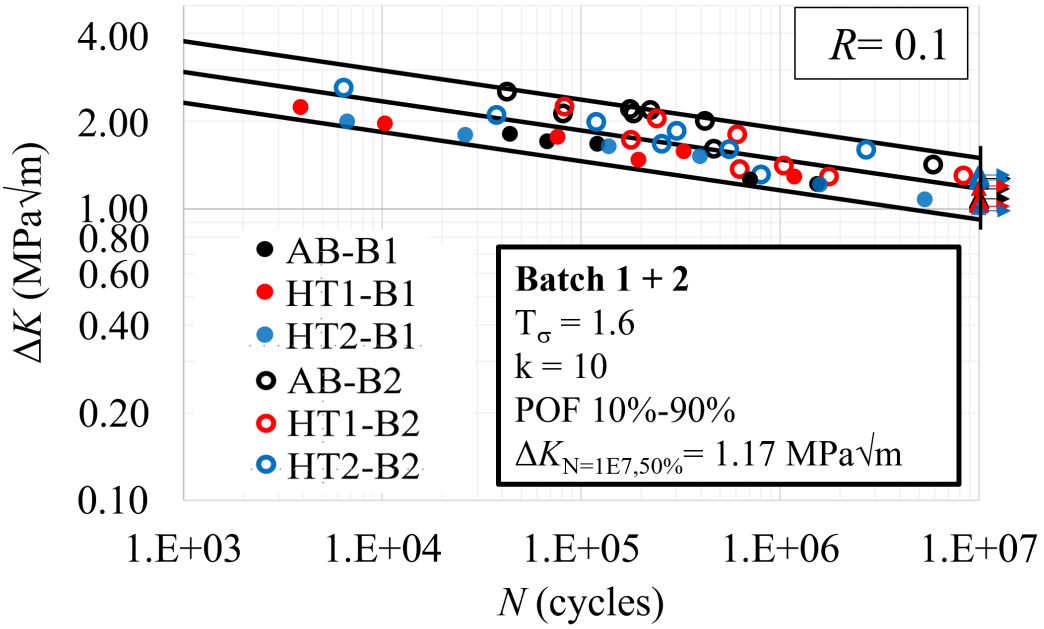

Figure 6.6.: Experimental relationship between stress intensity factor range ΔK at crack initiation site and number of cycles to failure N for the two batches in different heat treated conditions (as-built in black, HT1 in red and HT2 in blue). Filled symbols refer to batch 1 and empty symbols to batch 2.

A summary of the data used for the calculation and of the resulting values of $\sqrt{area}_0$ is provided in Table 6.4. The $\Delta K_{\mathbf{corr}} - N$ curves are shown in Figure 6.7. It can be seen that the correction significantly reduces the scatter between, as well as within, the batches and highlights the differences between the heat treatments. This representation shows an improved damage tolerance of the material after HT2, whereby the microstructure becomes more ductile due to the silicon spheroidisation.

Table 6.3.: Summary of the stress intensity factor investigation for the CT-analysed specimens.

Specimen Id.	$\sqrt{area}$ (μm)	$\Delta\sigma$ (MPa)	ΔK (MPa$\sqrt{\mathbf{m}}$)	Position	Killer defect
HT1-21b	89	150	1.63	surface	
	92	150	1.66	surface	
	159	150	2.01	surface	x
AB-9b	108	90	1.08	surface	
	118	90	1.13	surface	
	149	90	1.17	surface	x
AB-3b	81	110	1.14	surface	
	159	110	1.23	embedded	
	140	110	1.39	surface	x
HT1-22	88	140	1.63	surface	
	89	140	1.64	surface	
	94	140	1.72	surface	x

Table 6.4.: Summary of the material parameters used in the calculation estimated for each HT conditions.

	$\Delta\sigma_{\mathbf{e},R=-1}$ (MPa)	$\Delta\sigma_{\mathbf{e},R=0.1}$ (MPa)	$\Delta K_{\mathbf{th,LC}}$ (MPa$\sqrt{\mathbf{m}}$)	$\sqrt{area}_0$ (μm)
AB	275	160	1.4	24
HT1	256	142	1.6	40
HT2	220	110	2.4	150

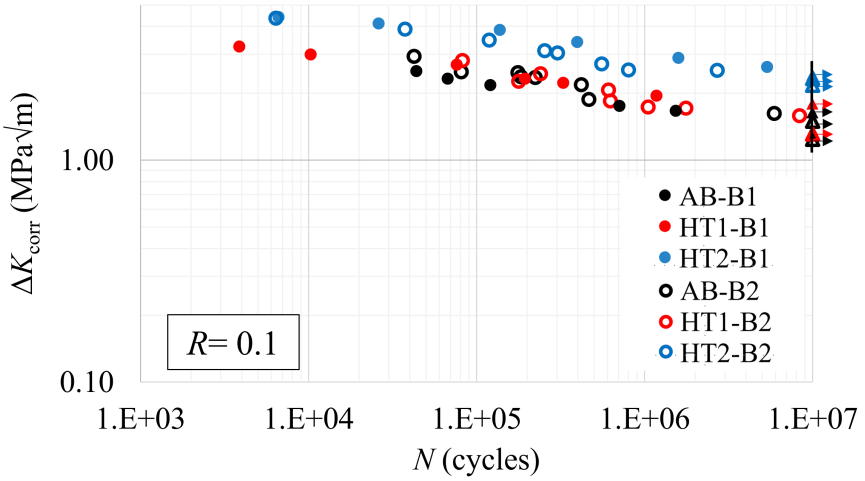

Figure 6.7.: Experimental relationship between the stress intensity factor range corrected for the short crack behaviour, $\Delta K_{\mathbf{corr}}$, and number of cycles to failure N for the two batches in different heat treated conditions (as-built in black, HT1 in red and HT2 in blue). Filled symbols refer to batch 1 and empty symbols to batch 2.

6.2.3. Modelling of fatigue resistance

Kitagawa-Takahashi diagram The results shown above evidenced that the presence of manufacturing defects causes a large scatter in the fatigue resistance. Most of this variability can be accounted for defining the relationship between the defect size and the material fatigue strength by means of the Kitagawa-Takahashi (KT) diagram, which provide the fatigue limit in presence of a defect. The results obtained are summarised in a KT diagram in Figure 6.8. The El Haddad and Murakami models, introduced in the Chapter 3.4.4 are compared.
For the El Haddad model (solid lines in Figure 6.8), the fatigue limit $\Delta\sigma_{\mathbf{e}}$ in the absence of defects and the crack propagation threshold $\Delta K_{\mathbf{th,LC}}$ at stress ratio R=0.1 (as estimated in Chapter 6.2.2 and reported in Table 6.4) are used to determine the left and right sides of the diagram for each HT condition. Equation 3.22 is adopted to describe the transition region.
The Murakami model (dashed lines in Figure 6.8), in its modified version in Equation 3.27 to take into account the mean stress, is calculated for each heat treated condition considering the different Vickers hardness measurements reported in Table 4.2.
The experimental points ($\Delta\sigma$, $\sqrt{area}$), obtained from the HCF testing, are shown in the figure for the two batches: batch 1 in '**x**' and batch 2 in '**+**'. The runouts are represented with triangles.
The KT diagram description with the El Haddad model (solid lines) provides a very good overview of the trend in the fatigue properties with respect to the defect size for the two batches, offering a sufficiently accurate approximation of the threshold of non-propagating cracks. Tests where failure occurred lie above the curve, in the region of propagating cracks, while the runout points are located at or below the threshold stress curve. On the contrary, it is observed that the Murakami model overestimates the fatigue threshold, providing a good approximation in a very small range of defect sizes: roughly for $\sqrt{area} = 20 - 60\ \mu m$ in the AB condition, $\sqrt{area} = 30 - 90\ \mu m$ for HT1 and $\sqrt{area} = 70 - 300\ \mu m$ for HT2. It is deemed that, in order to adopt this equation for the studied case, the α parameter, which weights the mean stress contribution, must be calibrated for aluminium alloys, as Schönbauer proposed for martensitic steels [169].

In conclusion, the different curves shown for the various HT conditions can be very well summarised by adopting the approach proposed by Atzori [144]. Introducing the effective defect size $\sqrt{area}_{\mathbf{eff}}$ (Equation 3.28), $\Delta\sigma_{\mathbf{th}}$ can be reformulated as in Equation 3.29. Normalising the values by the fatigue limit $\Delta\sigma_{\mathbf{e}}$, a general expression of the KT is obtained

as follow:

$$\frac{\Delta\sigma_{\mathbf{th}}}{\Delta\sigma_{\mathbf{e}}} = \frac{1}{\sqrt{\frac{\sqrt{area}_{\mathbf{eff}}}{\sqrt{area}_0} + 1}} \tag{6.5}$$

Equation 6.5 represents a general approach, which allows to convey all the experimental results in the different HT conditions in a single curve. The universal KT diagram is shown in Figure 6.9.

As an additional point, the fatigue threshold $\Delta\sigma_{\mathbf{th}}$ of the material with a certain defect size can be exploited to determine the effective driving force acting on the specimen during the test and accordingly determine a normalised S-N curve, net of the influence of defect size distribution [138]. The driving force, indeed, is not the absolute value of the applied stress $\Delta\sigma$ but should be measured as the value relative to the fatigue limit $\Delta\sigma_{\mathbf{th}}$, since it is the contribution $\Delta\sigma/\Delta\sigma_{\mathbf{th}}$, when greater than 1, that determines the finite lifetime of a component. Figure 6.2 shows the S-N curves of specimens from the two batches, containing defects with different sizes. When the Equation 3.22, proven to the best approximation of those examined, is applied to estimate the fatigue threshold $\Delta\sigma_{\mathbf{th}}$ for a specimen with a killer defect size $\sqrt{area}$, the experimental data can be rearranged in a normalised S-N diagram, as recently proposed by *Murakami* [138] and shown here in Figure 6.10.

The normalised S-N diagram allows to analyse the essential structure of S-N curves, highlighting that a change of slope occurs at 10^6 cycles. While for the first batch the scatter is minimised, the second batch still exhibits a non-negligible scatter.

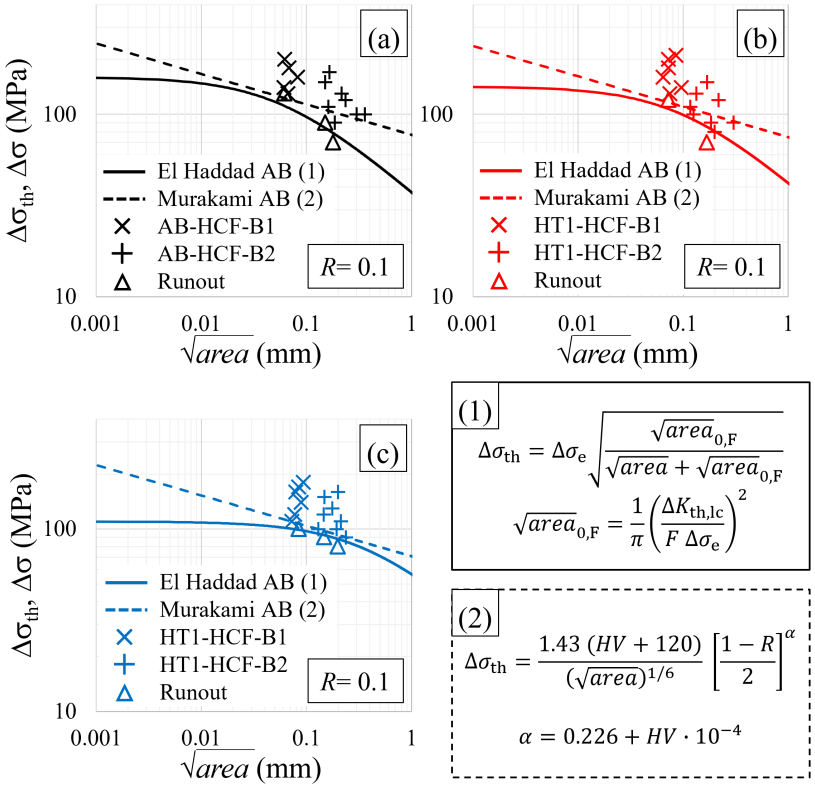

Figure 6.8.: Comparison in a Kitagawa-Takahashi diagram between the experimental fatigue results and the fatigue thresholds according to the El Haddad (1) and to the Murakami (2) model for the (a) AB, (b) HT1 and (c) HT2 conditions.

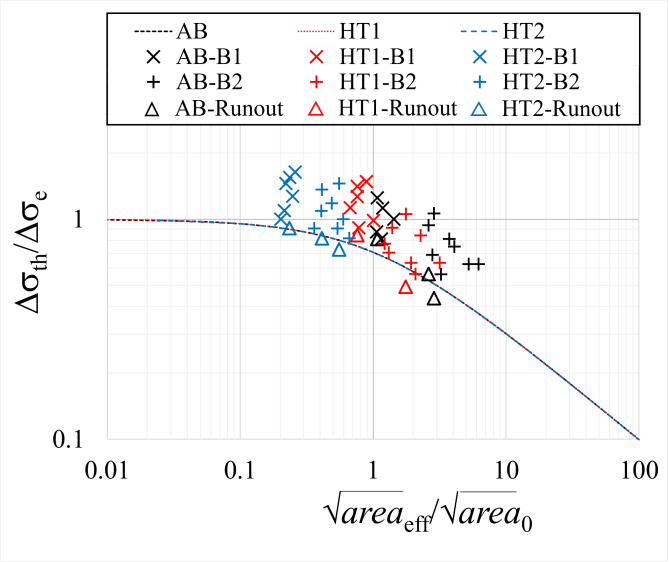

Figure 6.9.: Summary of all the experimental data for batch 1 and 2 in AB, HT1 and HT2 conditions in a Kitagawa-Takahashi diagram. The $\Delta\sigma_{th}$ is normalised by the flawless fatigue limit $\Delta\sigma_e$ and plotted as a function of $\sqrt{area}_{eff}/\sqrt{area}_0$.

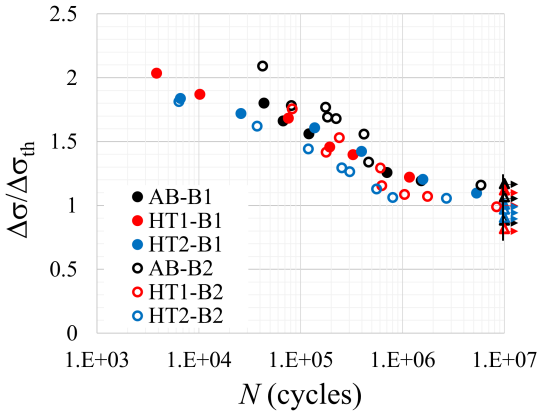

Figure 6.10.: Normalised S-N curve: summary of all the experimental data for batch 1 and 2 in AB, HT1 and HT2 conditions. The applied stress range $\Delta\sigma$ is normalised by the fatigue limit $\Delta\sigma_{th}$ of the specimen containing a small defect with a size equal to the killer defect $\sqrt{area}$.

Cyclic R-curve analysis It is important to note that both the Kitagawa-Takahashi diagram and the cyclic R-curve can describe whether a crack originating from a defect under given loading conditions is able to propagate or not. However, it has been proven [170], that the Kitagawa-Takahashi diagram is in many cases not conservative for short cracks, which have not built-up their crack closure completely. That implies that the region of non-propagating cracks in the Kitagawa-Takahashi diagram for physically short cracks is smaller than the prediction based on the El Haddad approximation. When the KT diagram is obtained using the cyclic R-curve it can predict significantly lower tolerable stresses.
This was verified for the present case by determining some points of the KT diagram through the cyclic R-curve analysis, as introduced in Chapter 3.4.4, identifying $\Delta\sigma_{\mathbf{th}}$ as the stress level $\Delta\sigma$ for which the crack driving force curve of the component $\Delta K_{\mathbf{p}}(\Delta\sigma)$ tangentially touches the cyclic R-curve, which starts at the level of $\Delta K_{\mathbf{th,eff}}$ and at the given initial crack (or defect) size a_i. The plasticity-corrected crack driving force was calculated from the Equation 3.31 after verifying that the material exhibits Masing's hypothesis. Details are provided in Appendix D. The points are depicted in a KT diagram in Figure 6.11, compared to the El Haddad model.

The theoretical cyclic R-curve analysis provides lower thresholds compared to the El Haddad model, whereby the build-up of closure is not considered. On the contrary, this aspect can be well captured by the cyclic R-curve analysis.
Furthermore, the effectiveness of the cyclic R-curve analysis approach in predicting crack arrest or propagation was verified. By introducing as input to the analysis the stress range $\Delta\sigma$ applied in the performed HCF tests and the size of the killer defect, measured post mortem, the crack propagation or arrest condition for the component can be determined by the mutual positioning of the curves. Some examples, from the two batches and in different heat treated conditions are shown in Figure 6.12. The results show how the cyclic R-curve gives a conservative prediction of the failure of a component. For example, in the tests where a runout occurred, the cyclic R-curve analysis shows a condition close to tangency of the curves as in Figure 6.12d,e. In the other cases the crack driving force curve lies above the R-curve.

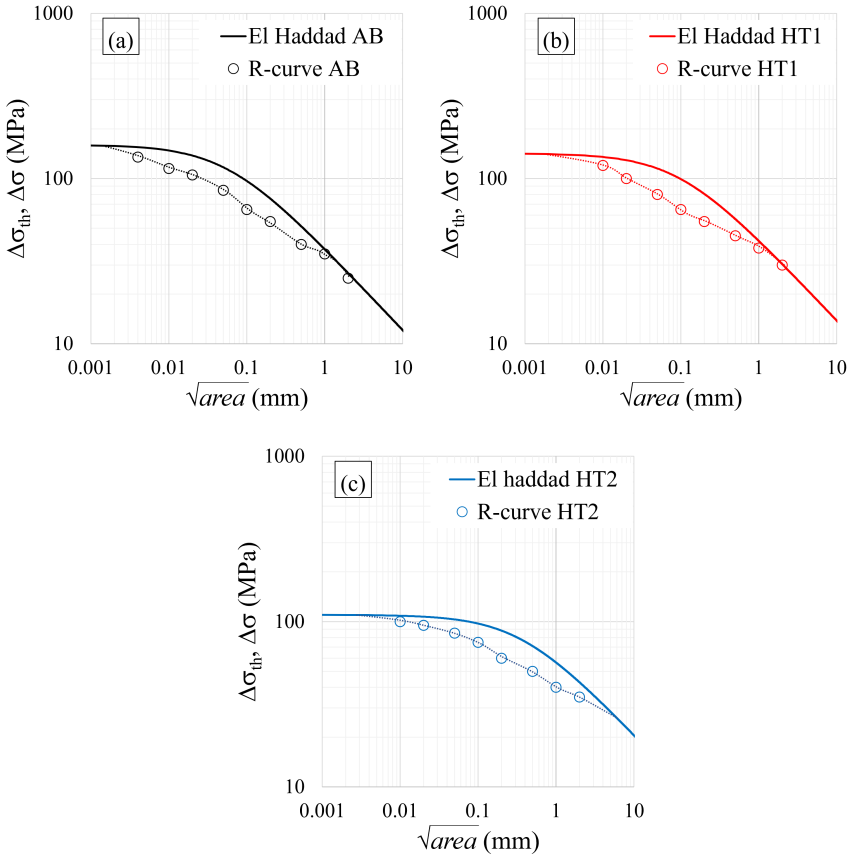

Figure 6.11.: Comparison of KT diagrams generated by the El Haddad approach and by cyclic R-curve analyses for the (a) AB, (b) HT1 and (c) HT2 conditions.

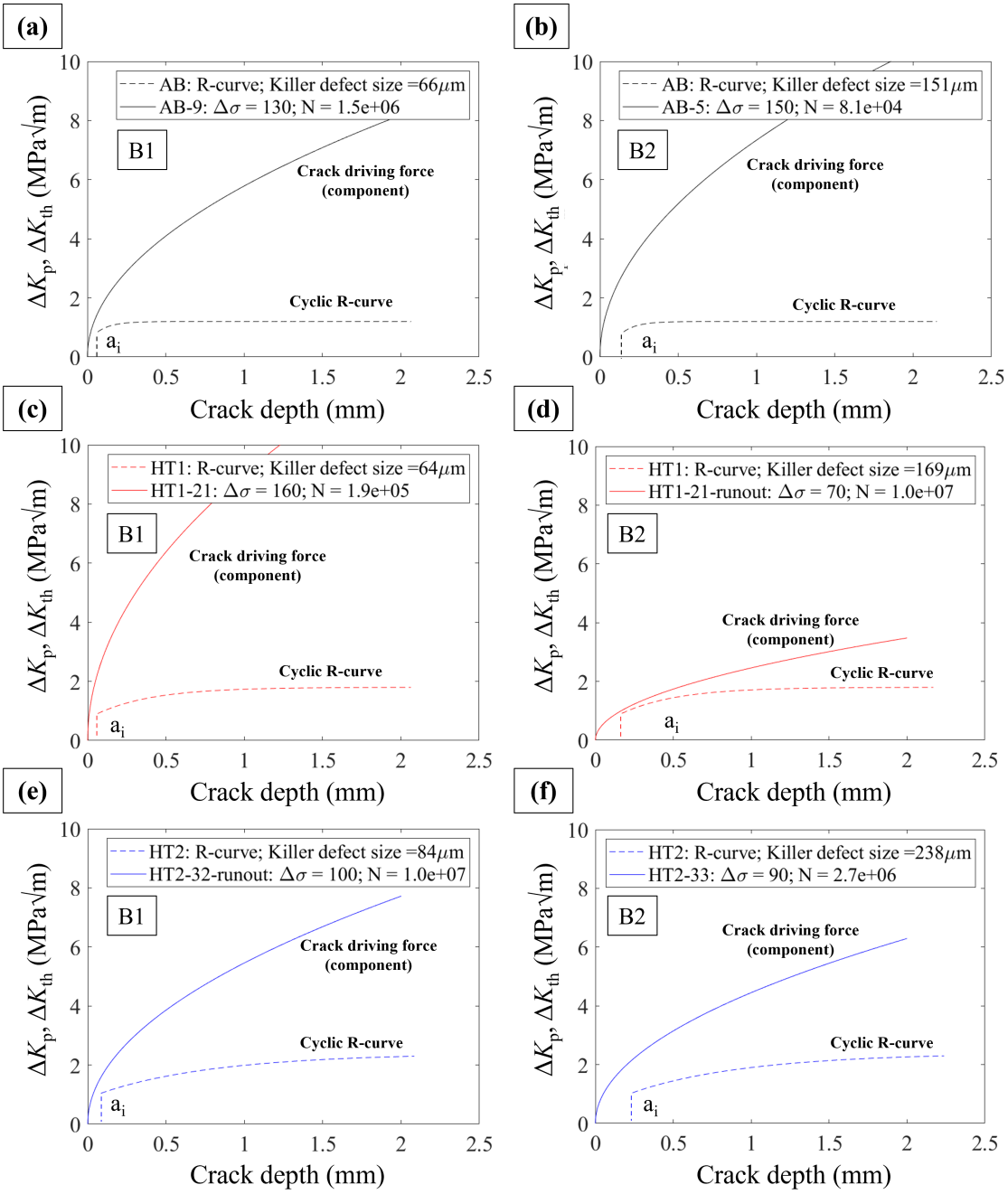

Figure 6.12.: Cyclic R-curve analysis. Examples for the three HT conditions: (a,b) AB; (c,d) HT1 and (e,f) HT2 for batch 1 (left) and 2 (right).

6.3. Conclusion

In the case of low residual stress values, as can be assumed from the measurements performed on a different specimen geometry, discussed in Chapter 4.3, the presence of defects overshadows the impact of the microstructure on the fatigue resistance. Defects, when larger than the microstructural features size, provide the nucleation site for the fatigue cracks. AM components are generally affected by manufacturing defects, with a stochastic nature. This results in a wide scatter in the experimental fatigue data. Consequently, in this work, it was observed that the S-N curves, which consider the remotely applied load as sole parameter, in the presence of a defective material are affected by a wide scatter and therefore, lose generality. In order to reduce the scatter of the data, it was proven to be crucial to take into account the size of the killer defect. This was shown by calculating the $\Delta K - N$ curves and thereafter, to take into account the behaviour of short cracks, the $\Delta K_{\mathbf{corr}} - N$ curves.
From a design point of view, fatigue strength estimations cannot be done without taking into account the mechanics of the defects. Therefore, various methods from the literature were applied to two batches with very different defect distributions. Their soundness and validity for the PBF-LB/M AlSi10Mg alloy was examined. The fatigue strength in the presence of defects and small crack propagation threshold have been defined by the Kitagawa diagram. The latter has been estimated in various ways: with the El Haddad approach, from the cyclic R-curve analysis and with the Murakami's $\sqrt{area}$ approach.
The El Haddad approach and the cyclic R-curve analysis were found to be valid and robust for predicting crack propagation or arrest. The prediction of the fatigue threshold as a function of defect size provided by the two models is in agreement with the experimental results. The determination of the fatigue threshold condition using the cyclic R-curve analysis was proved to be more conservative.
The model proposed by Murakami, which describes the fatigue limit as a function of only two parameters, very easily experimentally determined, namely the defect size and the Vickers hardness, was proved to be inaccurate for the case analysed. The model is likely to need a calibration for light alloys, particularly with regard to the correction for stress ratios R other than -1 (α coefficient).

7. Summary and concluding remarks

This work aimed to contribute to the understanding of the effects of low temperature heat treatments (HTs) on the properties of an AlSi10Mg alloy produced by laser powder bed fusion (PBF-LB/M). The AlSi10Mg material has been thoroughly characterised by means of microscopy, x-ray microtomography (μCT), diffraction methods for residual stress (RS) analysis, as well as static and fatigue testing. It is shown that the microstructure and residual stress state are subject to substantial changes at temperatures of 265°C and 300°C.

Regarding the microstructural and RS evolution in the as-built condition, the microstructure consists of α-aluminium small cells decorated by a nanometric silicon phase and enclosed by an almost continuous eutectic silicon (Si) network. Part of the Si and Mg atoms is in a supersaturated solid solution in the aluminium matrix. In this conformation, in the material bulk, tensile residual stresses, with an average value of 53 MPa, are measured in the aluminium matrix, while the silicon network undergoes compressive stresses, with an average value of -495 MPa. The heat treatment at 265°C for 1 hour (HT1) induces a precipitation of the supersaturated silicon from the aluminium matrix. This results in a stress relief on both the aluminium (average value of 23 MPa) and the silicon (average value of -255 MPa) phases. After the heat treatment at 300°C for 2 hours (HT2), the metastable as-built microstructure evolves towards a more stable condition with the formation of globularized Si particles through the disintegration of the eutectic network. This modification returns a higher residual stress state compared to HT1, with higher stresses on the matrix (40 MPa) and on the silicon particles (-315 MPa). While changes were observed in the core of the sample, the residual stress at the near-surface is similar in all the HT conditions: a compressive stress state with average values of 80 MPa was measured. This can be attributed to the machining and grinding performed to obtain the final geometry. In addition, it was found that porosity can have an influence on the residual stress measurements if clusters of voids happen to be located in the probed volume (gauge volume). This shows that, due to the complexity of AM materials, additional characterization regarding the microstructure of the component is strongly advised for a correct interpretation of the RS results.

Thereafter, the High Cycle Fatigue (HCF) behaviour (S-N curve), as well as the fatigue short (cyclic R-curve) and long ($\mathrm{d}a\,/\,\mathrm{d}N - \Delta K$ curve) crack growth behaviour were investigated. The detailed characterisation of microstructure and porosity (microscopy and (μCT) and residual stress was the key to interpret the results of the fatigue tests performed. When looking at the influence of these three fundamental factors on the fatigue resistance, the following conclusions can be drawn. Despite the above-mentioned differences, residual stresses are to be regarded as of little influence in the comparison of the fatigue performances of the three heat treatments examined. With regard to the HCF testing, the residual stress state in the near-surface, where the failure originates, is considered to be compressive and comparable in all the HT conditions. Similarly, in the fatigue crack propagation tests, the residual stress state at the notch tip, which adds up to the externally applied load and contribute to the stress experienced by the crack during its growth, is similar in all the conditions analysed. Thus, the focus turned on the effects of the microstructure and porosity.

Fatigue crack propagation in the near-threshold proved to be strongly influenced by the microstructure. A progressive increase in ductility after HT1 and HT2 leads to the development of plasticity-induced crack closure, which is believed to be the main mechanism involved in retarding fatigue crack propagation. The highest fatigue crack growth resistance was observed after HT2. The improvement is qualitatively comparable to that shown in the literature after a T6 (solution HT above 500°C + artificial ageing). This suggests that high temperature HTs may not be necessary to achieve better fatigue crack propagation resistance. A quantitative comparison between HT2 and T6, in order to assess conclusively whether the choice of a low temperature heat treatment over the traditional T6 is equivalent or even preferable, can be an important outlook in view of an industrial application.

Differently, when considering the total fatigue life by means of a S-N curve approach, the beneficial effect of the heat treatments was overshadowed. All the HT conditions could be represented by a single S-N curve with a large scatter. In other words, HCF testing evidenced one of the main challenges in the fatigue description of AM parts: the large scatter associated with the experimental results. This wide experimental scatter is related to the size of manufacturing defects within the material, which controls the fatigue resistance. In this work, the HCF response of two different batches of the material, with different defect distributions were investigated. The first batch presented the highest defect density (number of voids per volume unit), but with a regular round-shape, while the second batch contained fewer defects globally, but of larger sizes and irregular shapes. Consequently, the second batch generally showed a lower endurance than the first batch.

The presence of large irregular defects not only decreased the fatigue resistance of the material, but also increased the scatter associated to the Wöhler curve. In this regard, it is considered safer to produce a component with a higher gas porosity content but of controlled and regular size, as opposed to a component with higher density but with larger and irregular lack of fusion defects.

The presence of a wide scatter in the defect size and location distribution, typical of AM components, highlights the limit of generality represented by the S-N curves approach. These outcomes indicate that because of the major role that defects play in the fatigue behaviour of AM processed components, and therefore, fatigue design must be defect tolerant. The effect of defects on crack initiation and early propagation should be taken into account to establish fatigue assessment methods. This requires fracture mechanics-based approaches which cover the specific characteristics of so-called short fatigue cracks. Therefore, the experimentally obtained data were processed through defect tolerant approaches to determine the load carrying capacity of PBF-LB/M AlSi10Mg components in the presence of defects. The semi-empirical Kitagawa–Takahashi (KT) diagram was applied. In such diagram, the threshold cyclic stress is plotted against the crack (or defect size) in double-logarithmic scale. The KT diagram was determined in three different ways: with the El Haddad approach, from the cyclic R-curve analysis and with the Murakami's $\sqrt{area}$ approach. The El Haddad approach and the cyclic R-curve analysis were found to be valid and robust for predicting crack propagation or arrest. The prediction of the fatigue threshold as a function of defect size provided by the two models is in agreement with the experimental results. The determination of the fatigue threshold condition using the cyclic R-curve analysis was proved to be more conservative, particularly in the case of the heat-treated materials, where the effects of closure are more pronounced. In contrast, the empirical model proposed by Murakami, which describes the fatigue limit as a function of only two parameters, namely the defect size and the Vickers hardness, was proved to be inaccurate for the case analysed. The model is likely to need a calibration for light alloys, particularly with regard to the correction for stress ratios R other than -1 (i.e., the α coefficient).
In summary, the fracture mechanics methods are proved to be effective in evaluating the fatigue strength of the PBF-LB/M AlSi10Mg alloy when the main challenge is induced by the presence of defects.

In conclusion, it is important to remark that fatigue should not be regarded as a material property, but rather as a component property. Parameters such as the component geometry, the defect distribution and localization, the surface roughness, the residual stress state, are fundamental in identifying the critical sites and to establish suitable fatigue

assessment methods. The AM manufacturing technology is controlled by many process parameters which affect the build process, including the local cooling and reheating conditions. Consequently, the local material properties generally vary spatially within a given component. AM specimens may not be representative of those associated with parts, due primarily to differences in geometry which influence the thermal histories experienced during fabrication. The generation of representative test specimens and the reproducibility of the performance of the finished product seems to remain a limit which is particularly relevant for the safety of load carrying components. With respect to this, for example, it has been shown how the characterisation of defects by means of non-destructive testing becomes essential for fatigue design. In addition, if high residual stresses are present in the material, it becomes necessary to determine their distribution along the plane where the crack propagates in order to take RS influence into account. These distributions can be very complex and require very labour-intensive measurement or simulation techniques to be evaluated. Nevertheless such observations show how component design, damage and failure criteria, and microstructure characterisation need to be fully interlinked. Hence, future work needs to be focused on the use of these holistic approaches to develop enhanced damage tolerance concepts for AM products.

A. Heat treatment documentation

Herein the documentation related to the two heat treatment performed and studied in this work is reported. HT1 refers to an heat treatment at 265°C for 1 hour and HT2 to a heat treatment at 300°C for 2 hours. The heating and cooling rates were set to 10°C/min. The cooling was performed by an air cooling system. A schematic of the furnace during one of the treatment cycles performed is shown in Figure A.1a. The input temperature profiles in the programmable furnace are compared with the measured temperatures during the heat treatments in Figure A.1b.

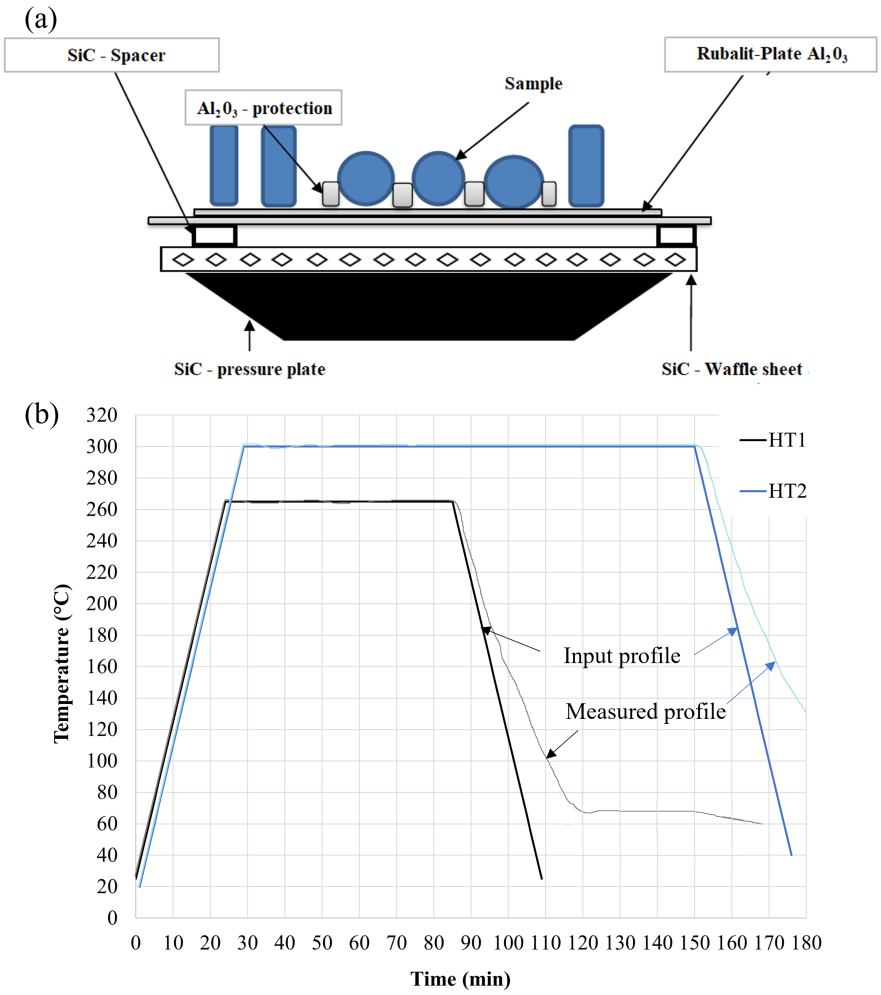

Figure A.1.: (a) Schematic of the PEO-630 furnace and (b) heat treatment temperature profiles during HT1 (265°C for 1 hour) and HT2 (300°C for 2 hours)

B. Peak-Over-Threshold method for μCT data analysis

The Peak Over Threshold-method (POT) allows to model extreme values by setting a threshold u and modelling the values in a distribution $x_1, \ldots, x_n$ exceeding it with the generalized Pareto class of distributions (GPD). The GPD is suitable for describing statistical properties of excesses.
Therefore a Generalized Pareto (GP) distribution $W_{\gamma,u,\sigma}$ can be fitted using the maximum likelihood (ML) method to determine the shape and scale parameters γ and σ. The cumulative distribution function of the GP is reported for the current case of γ=0.

$$W_{0,u,\sigma} = 1 - \exp \frac{x-u}{\sigma} \tag{B.1}$$

An appropriate u for all distributions studied was found to be 49 μm. The effectiveness of the choice can be verified by plotting the mean excess (ME) against the threshold value (Figure B.1) where ME can be empirically calculated as:

$$ME(u) = \frac{\sum_{i=1}^{n}(x_i - u)_{x_i|x_i>u}}{\sum_{i=1}^{n} i} \tag{B.2}$$

The linearity of the mean excess function characterizes the GPD class. Therefore a good threshold value can be selected in the range where the mean excess plot approximates a straight line. Two distributions are used in Chapter 4.1.2 and 6.2.1: one comprehend all the defects in the scanned volume, the second one, used to estimate the killer defects size, considers only the surface defects. The two Generalised Pareto distributions are shown in a probability plot in Figure B.2. When the extreme value statistics is used to assess the killer defects sizes, a correction to consider the real volume, subjected to the applied load, must be performed. In the current case, the scanned volume is only a portion of the gauge volume probed during HCF testing. This is taken into account by the following procedure [165]. Under the hypothesis of constant defect density, the return period T of the maximum defect in the actual tested volume V_c, can be calculated as:

$$T = \frac{N_s}{V_s} \cdot V_c \tag{B.3}$$

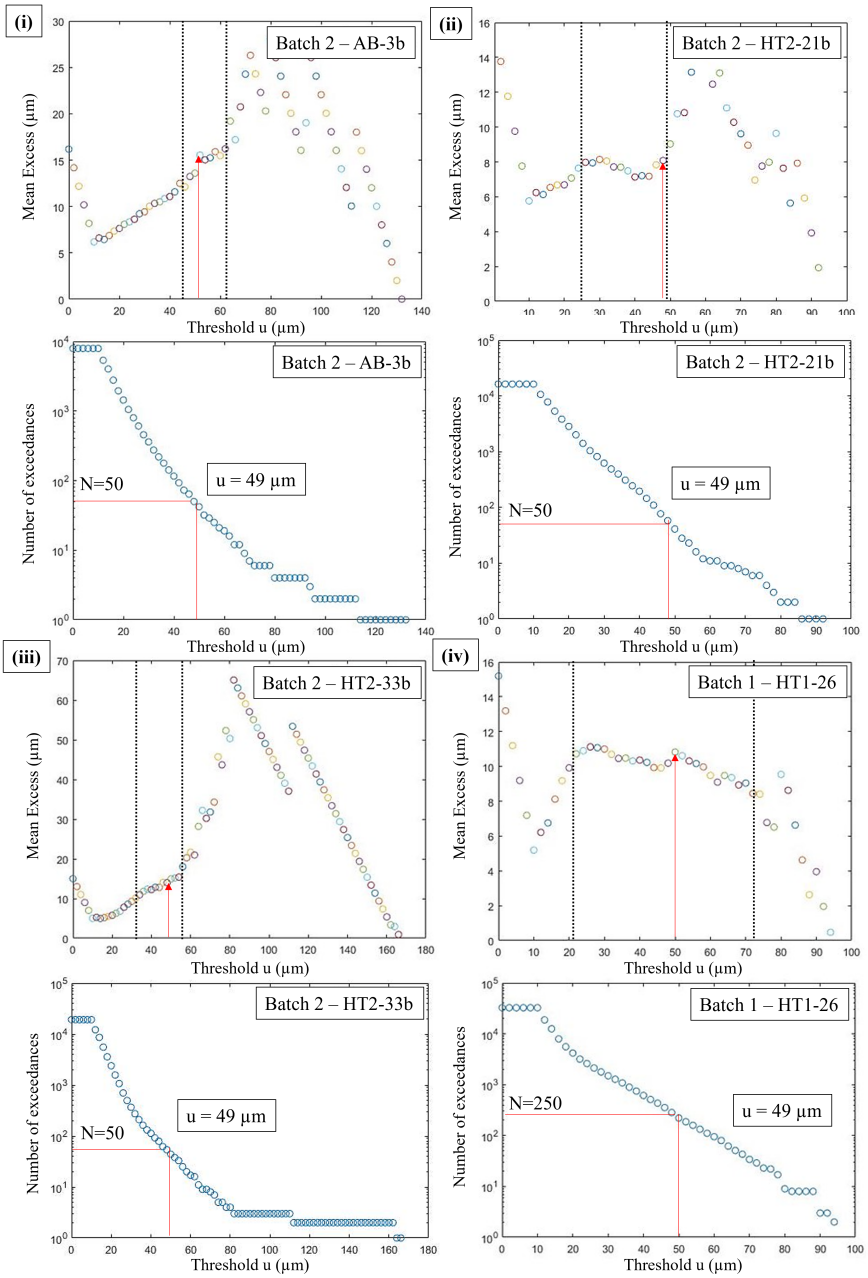

Figure B.1.: Mean excess and number of exceedances in function of the threshold value u for the defect distributions analysed in Chapter 4.1: three samples of the second batch (i) AB-3b, (ii) HT1-21b and (iii) HT2-33b and a sample from the first batch (iv) HT1-22.

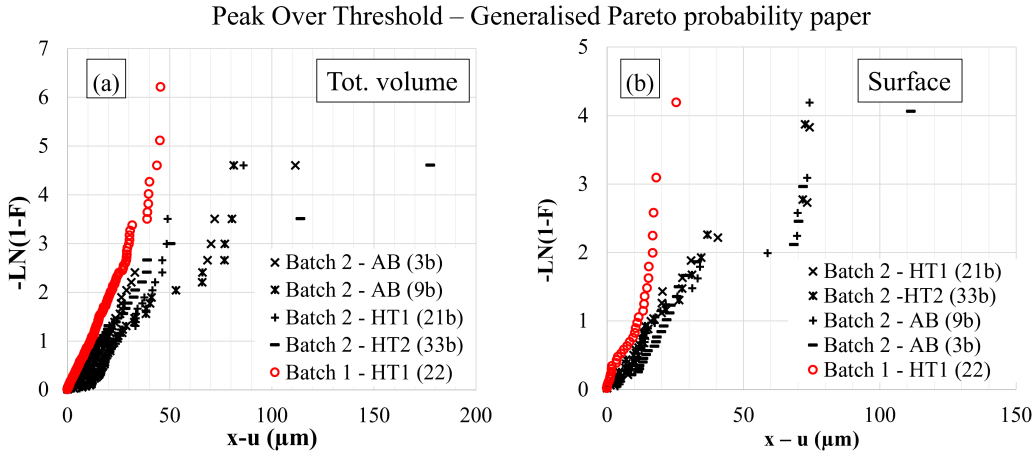

Figure B.2.: Generalised Pareto probability plot of the defect distribution considering (a) the total volume and (b) the superficial defects.

where N_s is the number of data exceeding the threshold in the scanned volume V_s. Applying the concepts of extreme value statistics, the modal value of the maximum defect in a volume V_c will have a size:

$$x_{\mathbf{max},V_c} = u + \sigma \cdot \ln(T) \tag{B.4}$$

The cumulative distribution function of the largest defect in V_c, in case of $\gamma \to 0$ can be approximated to a Gumbel distribution:

$$F_{\mathbf{max},V_c} \approx \exp\left(-\exp\left[-\frac{x - x_{\mathbf{max},V_c}}{\sigma}\right]\right) \tag{B.5}$$

C. HCF parameter and test results

The experimental parameters and results of the HCF tests discussed in Chapter 6.2 are shown in Table C.1 and C.2. The stress ratio (R), the test frequency (f), the minimum and maximum load applied (F_{min} and F_{max}) and the resulting force range (ΔF), the cross-sectional diameter in the gauge length (d), the applied stress range $\Delta\sigma$ and resulting number of cycles to failure (N) are reported.

In the post mortem state, the defect size of the killer defect was measured and is reported in Table C.3 and C.3 as $\sqrt{area}$. Consequently, considering that all defects were found superficial, the stress intensity factors ΔK from Equation 3.18 and the corrected values for short-crack effects from Equation 6.3 were calculated accordingly. The results are summarised in Table C.3.

Furthermore, in Chapter 6.2.2, the fatigue limit of the flawless material $\Delta\sigma_e$ for a fully-reversed load was estimated from the Vickers hardness (HV) as:

$$\sigma_{\mathbf{e}} = 1.6HV \pm 0.1HV \tag{C.1}$$

The conversion to a stress ratio R = 0.1, performed adopting the Goodman-Haigh diagram [167, 168], is illustrated in Figure C.1.

Table C.1.: Summary of the HCF experimental parameters and the corresponding results for batch 1.

Batch	Specimen Id.	R	f (Hz)	$F_{\mathbf{min}}$ (kN)	$F_{\mathbf{max}}$ (kN)	ΔF (kN)	d (mm)	σ (MPa)	N (cycles)	Runout
1	AB-8	0.1	30	1.162	11.624	10.462	7.904	105	1.65E+04	
	AB-9	0.1	30	0.709	7.088	6.379	7.905	65	1.53E+06	
	AB-10	0.1	30	0.991	9.913	8.922	7.944	90	6.73E+04	
	AB-11	0.1	30	0.885	8.853	7.967	7.963	80	1.20E+05	
	AB-12	0.1	30	0.770	7.695	6.926	7.937	70	7.06E+05	
	AB-13	0.1	30	0.720	7.196	6.476	7.964	65	1.00E+07	x
	AB-13-bis	0.1	30	0.720	7.196	6.476	7.964	100	4.37E+04	
	HT1-18	0.1	30	1.147	6.311	5.164	7.913	105	3.87E+03	
	HT1-19	0.1	30	1.103	6.065	4.962	7.959	90	1.03E+04	
	HT1-20	0.1	30	0.719	3.957	3.237	7.963	65	1.17E+06	
	HT1-21	0.1	30	0.883	4.858	3.974	7.953	80	1.94E+05	
	HT1-22	0.1	30	0.773	4.252	3.479	7.954	70	3.27E+05	
	HT1-23	0.1	30	0.662	3.639	2.977	7.949	60	1.00E+07	x
	HT1-23-bis	0.1	30	0.995	5.472	4.477	7.949	100	7.60E+04	
	HT2-27	0.1	30	0.749	4.121	3.372	7.832	70	3.96E+05	
	HT2-28	0.1	30	0.631	3.469	2.839	7.761	60	1.59E+06	
	HT2-29	0.1	30	0.852	4.684	3.832	7.810	80	1.37E+05	
	HT2-30	0.1	30	0.964	5.304	4.340	7.835	90	6.64E+03	
	HT2-31	0.1	30	0.593	3.260	2.668	7.859	55	5.34E+06	
	HT2-32	0.1	30	0.542	2.980	2.438	7.880	50	1.00E+07	x
	HT2-32-bis	0.1	30	0.921	5.066	4.145	7.880	85	2.60E+04	

Table C.2.: Summary of the HCF experimental parameters and the corresponding results for batch 2.

Batch	Specimen Id.	R	f (Hz)	$F_{\mathbf{min}}$ (kN)	$F_{\mathbf{max}}$ (kN)	ΔF (kN)	d (mm)	σ (MPa)	N (cycles)	Runout
	AB-2b	0.1	30	0.712	7.121	6.409	7.923	65	1.76E+05	
	AB-3b	0.1	30	0.605	6.047	5.442	7.937	55	4.66E+05	
	AB-4b	0.1	30	0.382	3.815	3.434	7.903	35	1.00E+07	x
	AB-4b-bis	0.1	30	0.927	9.266	8.340	7.903	85	4.24E+04	
	AB-5b	0.1	30	0.491	4.906	4.416	7.904	45	1.00E+07	x
	AB-5b-bis	0.1	30	0.818	8.177	7.360	7.904	75	8.12E+04	
	AB-6b	0.1	30	0.654	6.544	5.889	7.905	60	1.84E+05	
	AB-7b	0.1	30	0.546	5.456	4.911	7.907	50	2.24E+05	
	AB-8b	0.1	30	0.546	5.456	4.910	7.907	50	4.20E+05	
	AB-9b	0.1	30	0.490	4.905	4.414	7.903	45	5.91E+06	
	HT1-14b	0.1	30	0.707	7.069	6.362	7.894	65	1.78E+05	
	HT1-15b	0.1	30	0.489	4.888	4.399	7.889	45	1.05E+06	
	HT1-16b	0.1	30	0.586	5.859	5.274	7.813	55	6.28E+05	
	HT1-17b	0.1	30	0.653	6.530	5.877	7.897	60	2.41E+05	
2	HT1-18b	0.1	30	0.545	5.446	4.902	7.900	50	1.76E+06	
	HT1-19b	0.1	30	0.484	4.836	4.352	7.847	45	6.09E+05	
	HT1-20b	0.1	30	0.437	4.370	3.933	7.911	40	8.39E+06	
	HT1-21b	0.1	30	0.381	3.808	3.427	7.895	35	1.00E+07	x
	HT1-21b-bis	0.1	30	0.816	8.159	7.343	7.895	75	8.26E+04	
	HT2-26b	0.1	30	0.707	7.071	6.364	7.895	65	1.19E+05	
	HT2-27b	0.1	30	0.490	4.904	4.413	7.902	45	1.00E+07	x
	HT2-27b-bis	0.1	30	0.817	8.173	7.356	7.902	75	3.75E+04	
	HT2-28b	0.1	30	0.586	5.860	5.274	7.813	55	3.03E+05	
	HT2-29b	0.1	30	0.655	6.548	5.893	7.907	60	2.54E+05	
	HT2-30b	0.1	30	0.545	5.447	4.902	7.900	50	5.57E+05	
	HT2-31b	0.1	30	0.545	5.453	4.907	7.905	50	8.04E+05	
	HT2-32b	0.1	30	0.435	4.350	3.915	7.894	40	1.00E+07	x
	HT2-32b-bis	0.1	30	0.870	8.700	7.830	7.894	80	6.39E+03	
	HT2-33b	0.1	30	0.489	4.886	4.398	7.888	45	2.71E+06	

Table C.3.: Summary of the stress intensity factors at the crack tip in the tested specimens of batch 1.

Batch	Specimen Id.	$\sqrt{area}$ (μm)	ΔK (MPa$\sqrt{m}$)	$\Delta K_{\mathbf{corr}}$ (MPa$\sqrt{m}$)	$\Delta\sigma$ (MPa)	N (cycles)
1	AB-9	66	1.22	1.67	130	1.53E+06
	AB-10	68	1.71	2.32	180	6.73E+04
	AB-11	82	1.67	2.18	160	1.20E+05
	AB-12	61	1.26	1.76	140	7.06E+05
	AB-13	62	1.18	1.64	130	1.00E+07
	AB-13-bis	62	1.81	2.52	200	4.37E+04
	HT1-18	85	2.24	3.26	210	3.87E+03
	HT1-19	73	1.77	2.69	180	1.03E+04
	HT1-20	75	1.29	1.95	130	1.17E+06
	HT1-21	64	1.48	2.33	160	1.94E+05
	HT1-22	96	1.58	2.23	140	3.27E+05
	HT1-23	73	1.18	1.79	120	1.00E+07
	HT1-23-bis	73	1.96	2.99	200	7.60E+04
	HT2-27	89	1.52	3.41	140	3.96E+05
	HT2-28	77	1.22	2.89	120	1.59E+06
	HT2-29	79	1.64	3.86	160	1.37E+05
	HT2-30	93	2.00	4.41	180	6.64E+03
	HT2-31	73	1.08	2.63	110	5.34E+06
	HT2-32	84	1.06	2.43	100	1.00E+07
	HT2-32-bis	84	1.80	4.12	170	2.60E+04

Table C.4.: Summary of the stress intensity factors at the crack tip in the tested specimens of batch 2.

Batch	Specimen Id.	$\sqrt{area}$ (μm)	ΔK (MPa$\sqrt{m}$)	$\Delta K_{\mathbf{corr}}$ (MPa$\sqrt{m}$)	$\Delta\sigma$ (MPa)	N (cycles)
2	AB-2b	216	2.20	2.48	130	1.76E+05
	AB-3b	161	1.61	1.87	110	4.66E+05
	AB-4b	166	1.04	1.20	70	1.00E+07
	AB-4b-bis	166	2.62	3.01	170	4.24E+04
	AB-5b	151	1.27	1.50	90	1.00E+07
	AB-5b-bis	151	2.12	2.49	150	8.12E+04
	AB-6b	235	2.12	2.37	120	1.84E+05
	AB-7b	358	2.18	2.35	100	2.24E+05
	AB-8b	301	2.00	2.18	100	4.20E+05
	AB-9b	186	1.42	1.62	90	5.91E+06
	HT1-14b	133	1.73	2.26	130	1.78E+05
	HT1-15b	184	1.41	1.74	90	1.05E+06
	HT1-16b	117	1.37	1.85	110	6.28E+05
	HT1-17b	218	2.04	2.45	120	2.41E+05
	HT1-18b	126	1.29	1.71	100	1.76E+06
	HT1-19b	302	1.80	2.07	90	6.09E+05
	HT1-20b	199	1.30	1.58	80	8.39E+06
	HT1-21b	169	1.05	1.31	70	1.00E+07
	HT1-21b-bis	169	2.24	2.81	150	8.26E+04
	HT2-26b	175	1.98	3.46	130	1.19E+05
	HT2-27b	148	1.26	2.33	90	1.00E+07
	HT2-27b-bis	148	2.10	3.89	150	3.75E+04
	HT2-28b	213	1.85	3.03	110	3.03E+05
	HT2-29b	146	1.67	3.11	120	2.54E+05
	HT2-30b	193	1.60	2.71	100	5.57E+05
	HT2-31b	129	1.31	2.55	100	8.04E+05
	HT2-32b	199	1.30	2.18	80	1.00E+07
	HT2-32b-bis	199	2.60	4.35	160	6.39E+03
	HT2-33b	238	1.60	2.53	90	2.71E+06

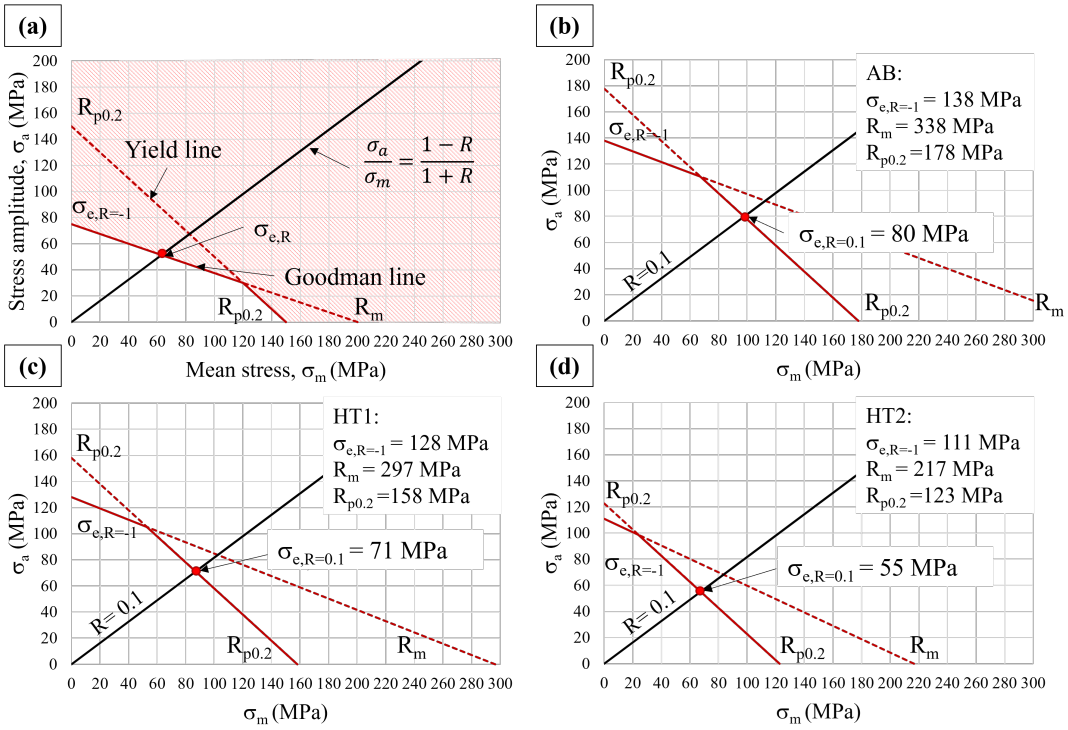

Figure C.1.: Goodman-Haigh diagram for the mean stress correction: (a) representation of the Goodman-Haigh diagram and application of the correction to the estimated fatigue limit in the (b) AB, (c) HT1 and (d) HT2 conditions.

D. Masing's behaviour of the PBF-LB/M AlSi10Mg alloy

Masing's hypothesis states that the stabilized hysteresis loop branch can be obtained by doubling the stabilised cyclic stress-strain curve [171]. Therefore, a simple correlation exists between the cyclic stress-strain curve and the ascending branch of the stabilized hysteresis loop. If the hysteresis loop branch is plotted in so-called relative coordinates ε' and σ', i.e., the last load reversal point is defined as the origin of the stress-strain coordinate system (blue curve in Figure D.1), and the cyclic stress-strain curve is magnified by a factor of two (orange curve in Figure D.1), both curves coincide in a reasonable approximation. In other words, both stress-strain paths are geometrically similar with a scale factor of two (homothetic transformation). It has been verified, for all heat treatments, that the material

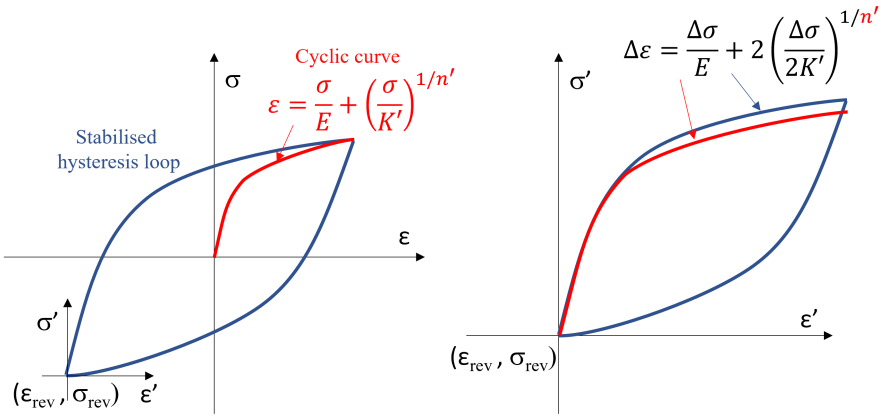

Figure D.1.: Schematic of the Masing's hypothesis.

exhibits Masing's behaviour. The results of the evaluations are shown in Figure D.2 for one of the two specimens tested for each condition. It is observed that the upper branch of the stabilised hysteresis cycle can be described in good approximation by the Ramberg-Osgood relation.

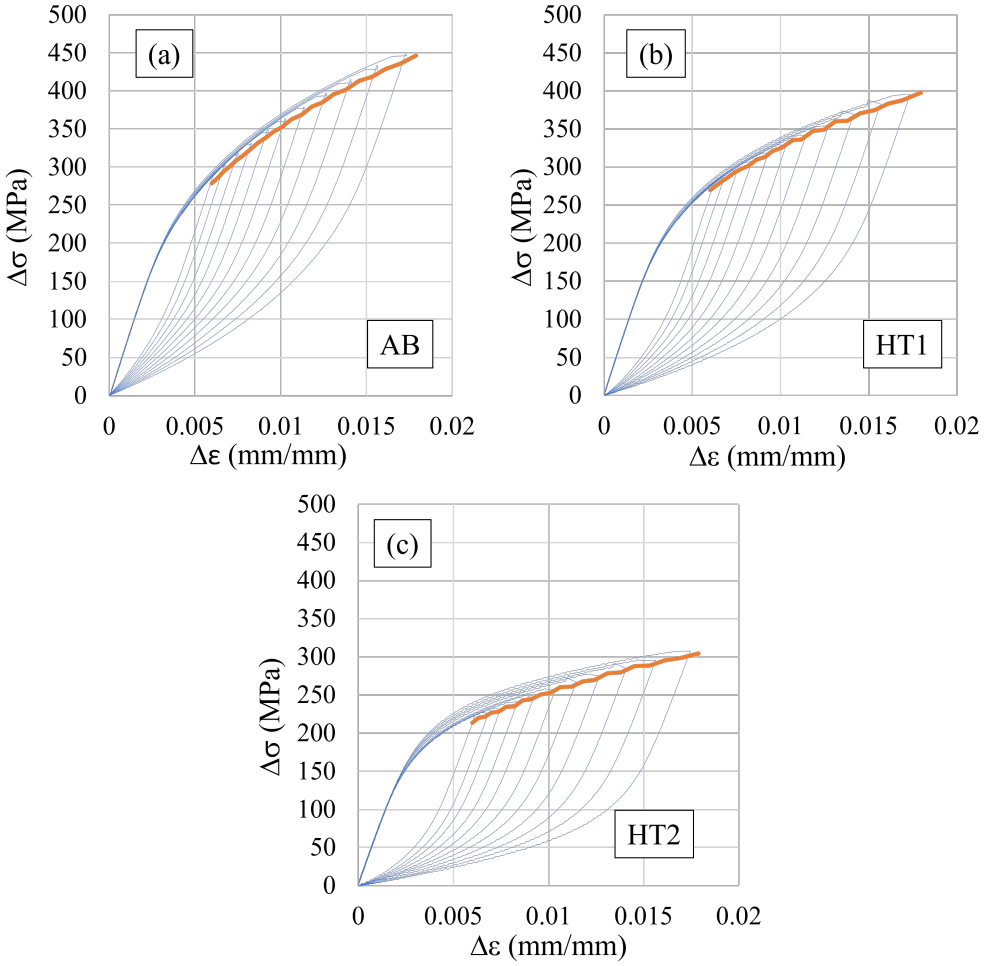

Figure D.2.: Verification of the Masing's hypothesis for the (a) as-built, (b) HT1 and (c) HT2 conditions.

E. Synchrotron X-ray diffraction results

Herein are reported the complete results of the synchrotron x-ray diffraction measurements on the SENB samples supplementing the information shown in Chapter 4.3.4.
The two lines in the notch plane at 1.5 mm from the surface, namely (vi) and (vii) in Figure 3.9, show a similar trend to the profiles on the central line (v) in Figure 4.16. The results are shown in Figure E.1 (line (vi)) and in Figure E.2 (line (vii)) for the Al {311} and the Si {311} diffraction in the AB (black), HT1 (red) and HT2 (blue) conditions.

The results for the Si {220}, which is affected by the intergranular stress and therefore is not considered representative of the RS on the Si phase, are show in Figures E.3 (line (v)), E.4 (line (vi)) and E.5 (line (vii)) to be thorough.

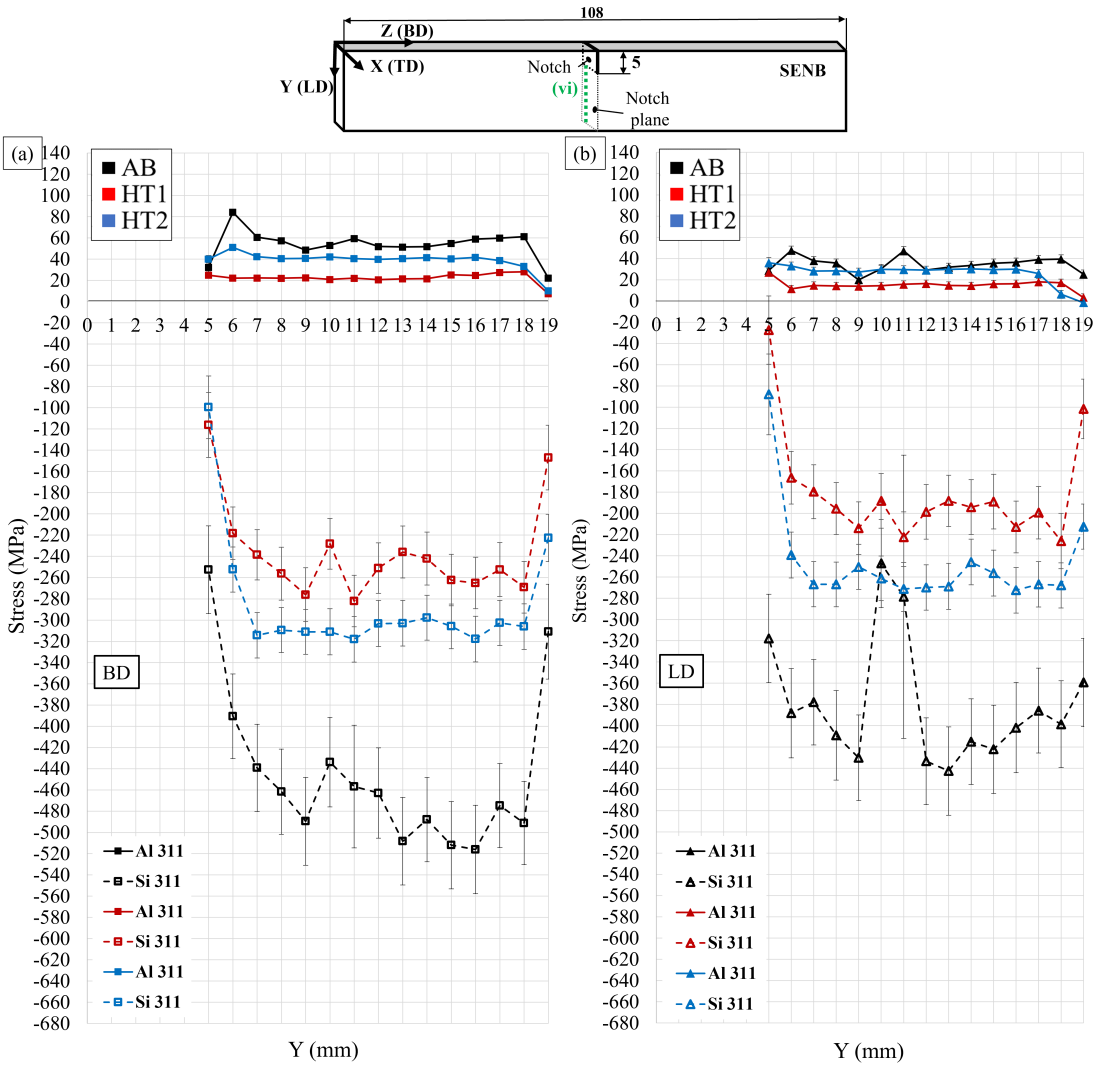

Figure E.1.: Bulk RS profiles before and after heat treatment in the notch plane at 1.5 mm from the surface for the (a) BD and (b) LD. The results are reported for the Al {311} and the Si {311} peaks in the AB (black), HT1 (red) and HT2 (blue) conditions.

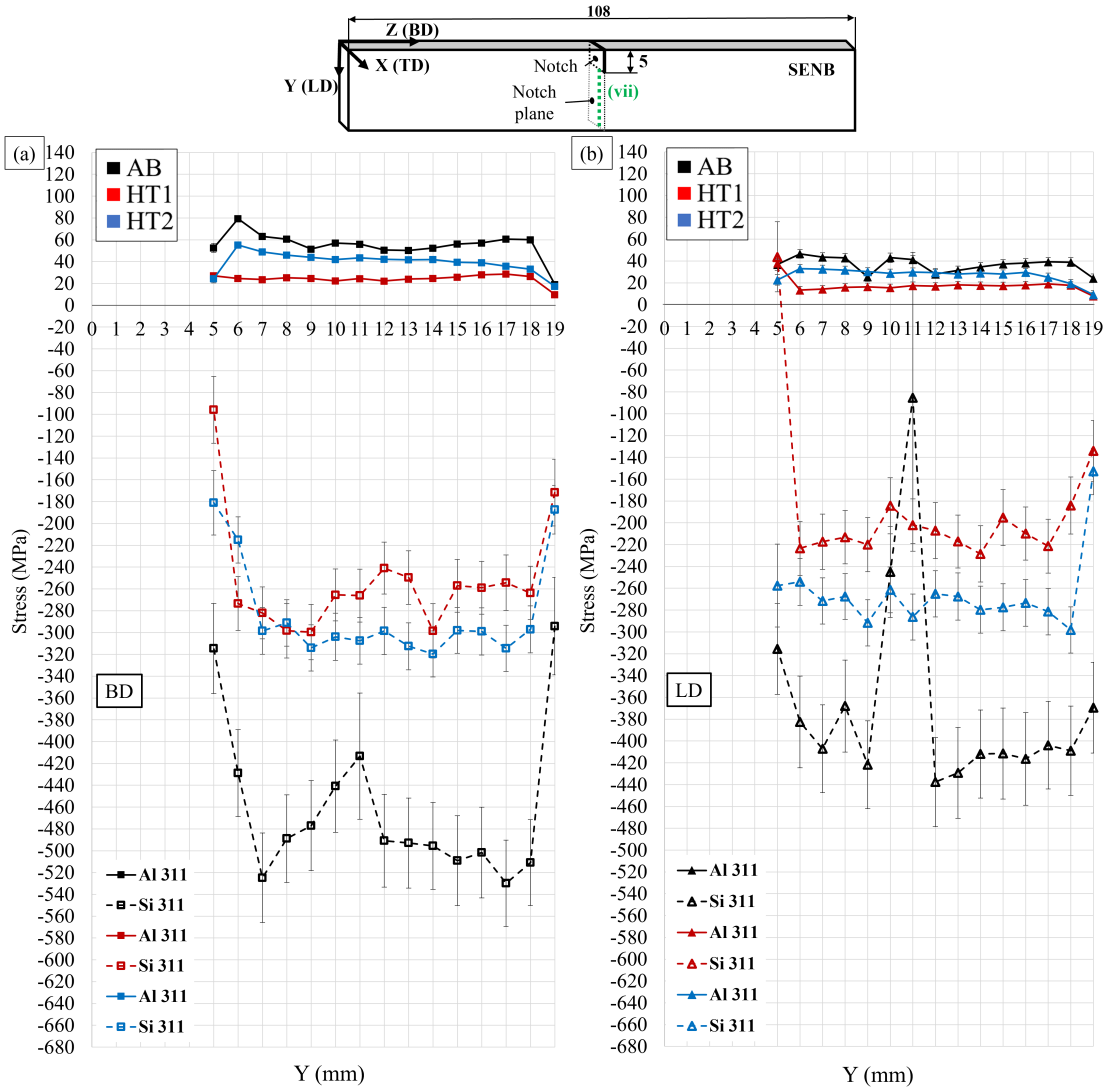

Figure E.2.: Bulk RS profiles before and after heat treatment in the notch plane at 1.5 mm from the surface for the (a) BD and (b) LD. The results are reported for the Al {311} and the Si {311} peaks in the AB (black), HT1 (red) and HT2 (blue) conditions.

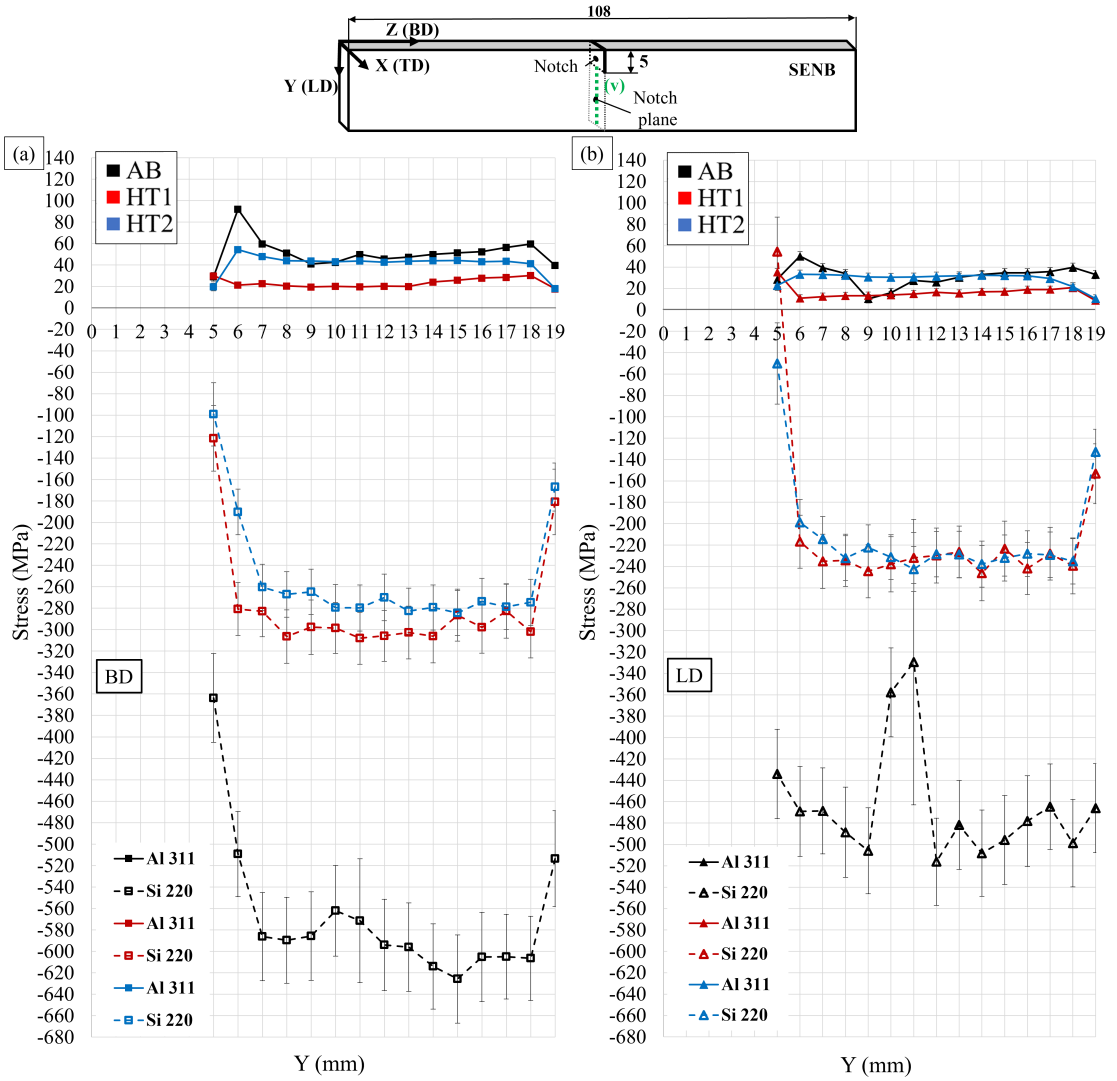

Figure E.3.: Bulk RS profiles before and after heat treatment in the centre of the notch plane for the (a) BD and (b) LD. The results are reported for the Al {311} and the Si {220} peaks in the AB (black), HT1 (red) and HT2 (blue) conditions.

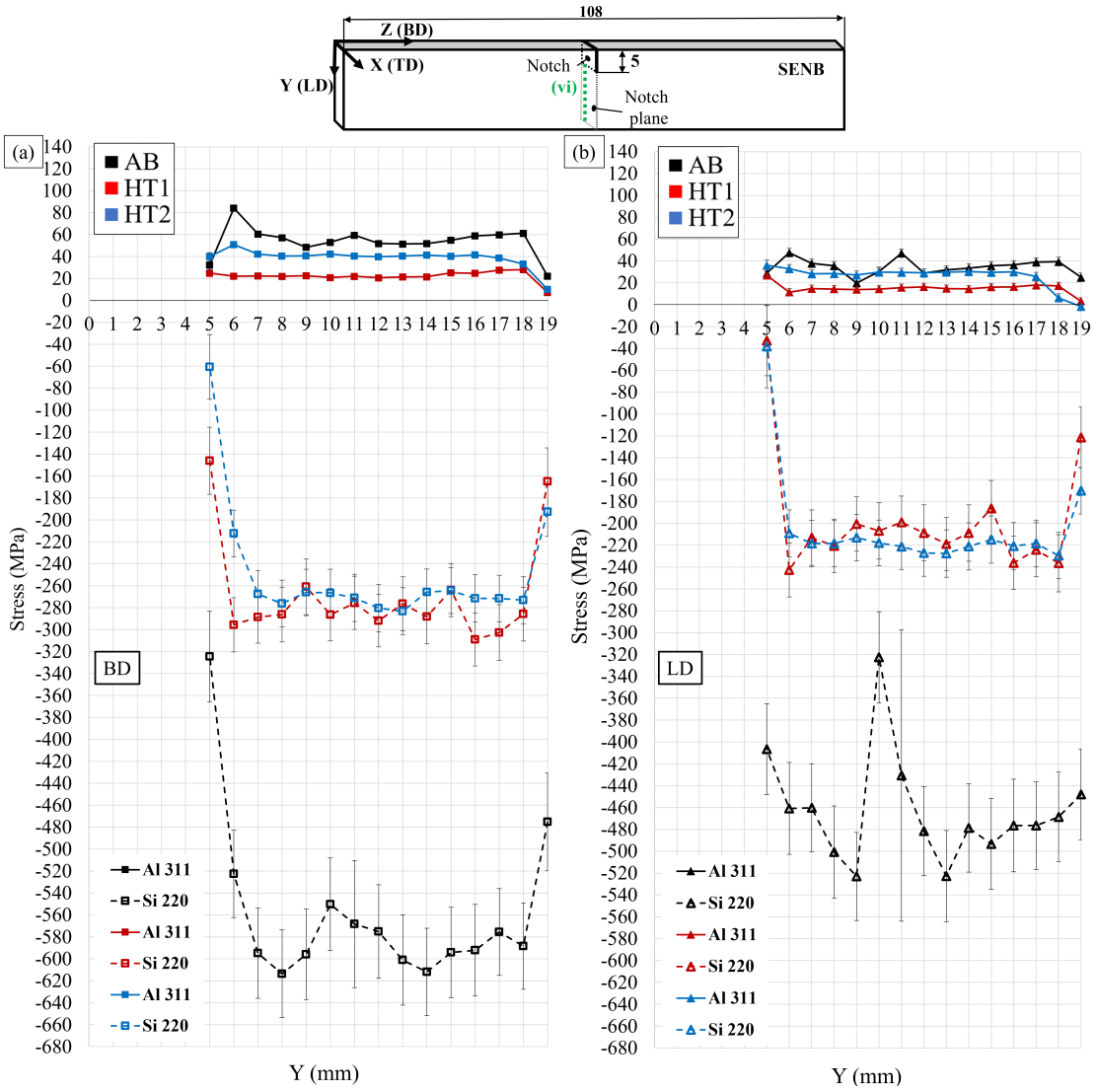

Figure E.4.: Bulk RS profiles before and after heat treatment in the notch plane at 1.5 mm from the surface for the (a) BD and (b) LD. The results are reported for the Al {311} and the Si {220} peaks in the AB (black), HT1 (red) and HT2 (blue) conditions.

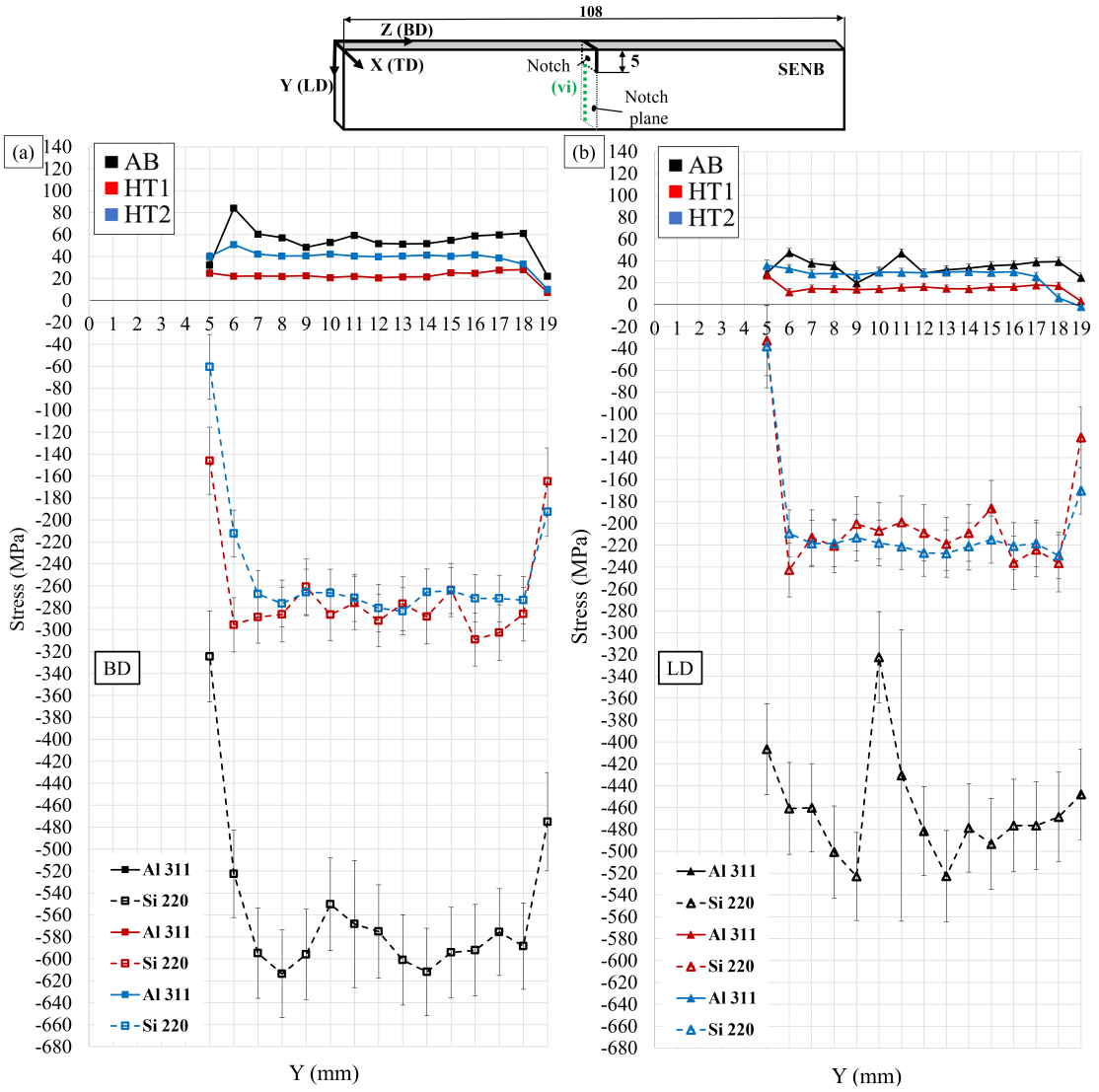

Figure E.5.: Bulk RS profiles before and after heat treatment in the notch plane at 1.5 mm from the surface for the (a) BD and (b) LD. The results are reported for the Al {311} and the Si {220} peaks in the AB (black), HT1 (red) and HT2 (blue) conditions.

Bibliography

[1] S. I. Shakil, A. Hadadzadeh, B. Shalchi Amirkhiz, H. Pirgazi, M. Mohammadi, and M. Haghshenas. Additive manufactured versus cast AlSi10Mg alloy: Microstructure and micromechanics. *Results in Materials*, 10, 2021. ISSN 2590048X. doi: 10.1016/j.rinma.2021.100178.

[2] P. Van Cauwenbergh, V. Samaee, L. Thijs, J. Nejezchlebova, P. Sedlak, A. Ivekovic, D. Schryvers, B. Van Hooreweder, and K. Vanmeensel. Unravelling the multi-scale structure-property relationship of laser powder bed fusion processed and heat-treated AlSi10Mg. *Sci Rep*, 11(1):6423, 2021. ISSN 2045-2322 (Electronic) 2045-2322 (Linking). doi: 10.1038/s41598-021-85047-2.

[3] E. Ogris, A. Wahlen, H. Lüchinger, and P. J. Uggowitzer. On the silicon spheroidization in Al–Si alloys. *Journal of Light Metals*, 2(4):263–269, 2002. ISSN 14715317. doi: 10.1016/s1471-5317(03)00010-5.

[4] J. Fiocchi, A. Tuissi, P. Bassani, and C. A. Biffi. Low temperature annealing dedicated to AlSi10Mg selective laser melting products. *Journal of Alloys and Compounds*, 695:3402–3409, 2017. ISSN 09258388. doi: 10.1016/j.jallcom.2016.12.019.

[5] P. Yang, L. A. Deibler, D. R. Bradley, D. K. Stefan, and J. D. Carroll. Microstructure evolution and thermal properties of an additively manufactured, solution treatable AlSi10Mg part. *Journal of Materials Research*, 33(23):4040–4052, 2018. ISSN 0884-2914 2044-5326. doi: 10.1557/jmr.2018.405.

[6] S. Marola, D. Manfredi, G. Fiore, M. G. Poletti, M. Lombardi, P. Fino, and L. Battezzati. A comparison of Selective Laser Melting with bulk rapid solidification of AlSi10Mg alloy. *Journal of Alloys and Compounds*, 742:271–279, 2018. ISSN 09258388. doi: 10.1016/j.jallcom.2018.01.309.

[7] P. J. Withers and H. K. D. H. Bhadeshia. Residual stress Part 1 – Measurement techniques. *Materials Science and Technology*, 17:355–365, 2001.

[8] Heinz Thomas Beier, Patrick Yadegari, and Michael Vormwald. Influence of discontinuities on fatigue strength using the example of additively manufactured specimens made of AlSi10Mg. *MATEC Web of Conference, ICEAF-VI 2021*, 349:1–8, 2021. doi: https://doi.org/10.1051/matecconf/202134902010.

[9] S. Romano, A. Brückner-Foit, A. Brandão, J. Gumpinger, T. Ghidini, and S. Beretta. Fatigue properties of AlSi10Mg obtained by additive manufacturing: Defect-based modelling and prediction of fatigue strength. *Engineering Fracture Mechanics*, 187: 165–189, 2018. ISSN 00137944. doi: 10.1016/j.engfracmech.2017.11.002.

[10] S. Romano, A. Brandão, J. Gumpinger, M. Gschweitl, and S. Beretta. Qualification of AM parts: Extreme value statistics applied to tomographic measurements. *Materials & Design*, 131:32–48, 2017. ISSN 02641275. doi: 10.1016/j.matdes.2017.05.091.

[11] J. Fiocchi, A. Tuissi, and C. A. Biffi. Heat treatment of aluminium alloys produced by laser powder bed fusion: a review. *Materials & Design*, 204:109651, 2021. doi: https://doi.org/10.1016/j.matdes.2021.109651.

[12] M. K. Thompson, G. Moroni, T. Vaneker, G. Fadel, R. I. Campbell, I. Gibson, A. Bernard, J. Schulz, P. Graf, B. Ahuja, and F. Martina. Design for Additive Manufacturing: Trends, opportunities, considerations, and constraints. *CIRP Annals*, 65(2):737–760, 2016. ISSN 0007-8506. doi: https://doi.org/10.1016/j.cirp.2016.05.004.

[13] A. Paolini, S. Kollmannsberger, and E. Rank. Additive manufacturing in construction: A review on processes, applications, and digital planning methods. *Additive Manufacturing*, 30, 2019. ISSN 22148604. doi: 10.1016/j.addma.2019.100894.

[14] A. Aversa, G. Marchese, A. Saboori, E. Bassini, D. Manfredi, S. Biamino, D. Ugues, P. Fino, and M. Lombardi. New Aluminum Alloys Specifically Designed for Laser Powder Bed Fusion: A Review. *Materials (Basel)*, 12(7), 2019. ISSN 1996-1944 (Print) 1996-1944 (Linking). doi: 10.3390/ma12071007.

[15] K. Bartkowiak, S. Ullrich, T. Frick, and M. Schmidt. New Developments of Laser Processing Aluminium Alloys via Additive Manufacturing Technique. *Physics Procedia*, 12:393–401, 2011. ISSN 18753892. doi: 10.1016/j.phpro.2011.03.050.

[16] L. Thijs, K. Kempen, J. Kruth, and J. Van Humbeeck. Fine-structured aluminium products with controllable texture by selective laser melting of pre-alloyed AlSi10Mg powder. *Acta Materialia*, 61(5):1809–1819, 2013. ISSN 13596454. doi: 10.1016/j.actamat.2012.11.052.

[17] K. Kempen, L. Thijs, J. Van Humbeeck, and J.-P. Kruth. Mechanical Properties of AlSi10Mg Produced by Selective Laser Melting. *Physics Procedia*, 39:439–446, 2012. ISSN 18753892. doi: 10.1016/j.phpro.2012.10.059.

[18] T. DebRoy, H. L. Wei, J. S. Zuback, T. Mukherjee, J. W. Elmer, J. O. Milewski, A. M. Beese, A. Wilson-Heid, A. De, and W. Zhang. Additive manufacturing of metallic components – Process, structure and properties. *Progress in Materials Science*, 92: 112–224, 2018. ISSN 00796425. doi: 10.1016/j.pmatsci.2017.10.001.

[19] P. Yang, M. A. Rodriguez, L. A. Deibler, B. H. Jared, J. Griego, A. Kilgo, A. Allen, and D. K. Stefan. Effect of thermal annealing on microstructure evolution and mechanical behavior of an additive manufactured AlSi10Mg part. *Journal of Materials Research*, 33(12):1701–1712, 2018. ISSN 0884-2914 2044-5326. doi: 10.1557/jmr.2018.82.

[20] L. Zhou, A. Meht, E. Schulz, B. McWilliams, K. Cho, and Y. Sohn. Microstructure, precipitates and hardness of selectively laser melted AlSi10Mg alloy before and after heat treatment. *Materials Characterization*, 143:5–17, 2018. doi: https://doi.org/10.1016/j.matchar.2018.04.022.

[21] E. Padovano, C. Badini, A. Pantarelli, F. Gili, and F. D'Aiuto. A comparative study of the effects of thermal treatments on AlSi10Mg produced by laser powder bed fusion. *Journal of Alloys and Compounds*, 831, 2020. ISSN 09258388. doi: 10.1016/j.jallcom.2020.154822.

[22] H. Qin, Q. Dong, V. Fallah, and M. R. Daymond. Rapid Solidification and Non-equilibrium Phase Constitution in Laser Powder Bed Fusion (LPBF) of AlSi10Mg Alloy: Analysis of Nano-precipitates, Eutectic Phases, and Hardness Evolution. *Metallurgical and Materials Transactions A*, 51(1):448–466, 2019. ISSN 1073-5623 1543-1940. doi: 10.1007/s11661-019-05505-5.

[23] B. J. Mfusi, N. R. Mathe, L. C. Tshabalala, and P. AI. Popoola. The Effect of Stress Relief on the Mechanical and Fatigue Properties of Additively Manufactured AlSi10Mg Parts. *Metals*, 9(11), 2019. ISSN 2075-4701. doi: 10.3390/met9111216.

[24] I. Rosenthal, R. Shneck, and A. Stern. Heat treatment effect on the mechanical properties and fracture mechanism in AlSi10Mg fabricated by additive manufacturing selective laser melting process. *Materials Science and Engineering: A*, 729: 310–322, 2018. ISSN 09215093. doi: 10.1016/j.msea.2018.05.074.

[25] N. Takata, H. Kodaira, K. Sekizawa, A. Suzuki, and M. Kobashi. Change in microstructure of selectively laser melted AlSi10Mg alloy with heat treatments. *Materials Science and Engineering: A*, 704:218–228, 2017. ISSN 09215093. doi: 10.1016/j.msea.2017.08.029.

[26] I. Serrano-Munoz, I. Roveda, A. Kupsch, B. R. Müller, and G. Bruno. Synchrotron X-ray refraction detects microstructure and porosity evolution during in-situ heat treatments. *Materials Science and Engineering A*, 838:142732, 2022. doi: https://doi.org/10.1016/j.msea.2022.142732.

[27] N. T Aboulkhair, I. Maskery, C. Tuck, I. Ashcroft, and N. M. Everitt. The microstructure and mechanical properties of selectively laser melted AlSi10Mg: The effect of a conventional T6-like heat treatment. *Materials Science and Engineering: A*, 667: 139–146, 2016. ISSN 0921-5093.

[28] E. Brandl, U. Heckenberger, V. Holzinger, and D. Buchbinder. Additive manufactured AlSi10Mg samples using Selective Laser Melting (SLM): Microstructure, high cycle fatigue, and fracture behavior. *Materials & Design*, 34:159–169, 2012. ISSN 02613069. doi: 10.1016/j.matdes.2011.07.067.

[29] J. N. Domfang N., G. Henaff, Y. Nadot, J. Nicolai, and L. Ridosz. Fatigue resistance of selectively laser melted aluminum alloy under T6 heat treatment. *Procedia Engineering*, 213:79–88, 2018. ISSN 1877-7058. doi: https://doi.org/10.1016/j.proeng.2018.02.009.

[30] A. Kempf and K. Hilgenberg. Influence of heat treatments on AlSi10Mg specimens manufactured with different laser powder bed fusion machines. *Materials Science and Engineering: A*, 818, 2021. ISSN 09215093. doi: 10.1016/j.msea.2021.141371.

[31] L. F. Wang, J. Sun, X. L. Yu, Y. Shi, X. G. Zhu, L. Y. Cheng, H. H. Liang, B. Yan, and L. J. Guo. Enhancement in mechanical properties of selectively laser-melted AlSi10Mg aluminum alloys by T6-like heat treatment. *Materials Science and Engineering: A*, 734:299–310, 2018. ISSN 0921-5093.

[32] P. Wei, Z. Chen, S. Zhang, X. Fang, B. Lu, L. Zhang, and Z. Wei. Effect of t6 heat treatment on the surface tribological and corrosion properties of alsi10mg samples produced by selective laser melting. *Materials Characterization*, 171, 2021. ISSN 10445803. doi: 10.1016/j.matchar.2020.110769.

[33] J. G. Santos Macias, T. Douillard, L. Zhao, E. Maire, G. Pyka, and A. Simar. Influence on microstructure, strength and ductility of build platform temperature during

laser powder bed fusion of AlSi10Mg. *Acta Materialia*, 201:231–243, 2020. doi: https://doi.org/10.1016/j.actamat.2020.10.001.

[34] R. Casati, M. H. Nasab, M. Coduri, V. Tirelli, and M. Vedani. Effects of Platform Pre-Heating and Thermal-Treatment Strategies on Properties of AlSi10Mg Alloy Processed by Selective Laser Melting. *Metals*, 8:954, 2018. doi: https://doi.org/10.3390/met8110954.

[35] G. Asghar, L. Peng, P. Fu, L. Yuan, and Y. Liu. Role of Mg_2Si precipitates size in determining the ductility of A357 cast alloy. *Materials & Design*, 186:108280, 2020. ISSN 0264-1275. doi: https://doi.org/10.1016/j.matdes.2019.108280.

[36] C. Galy, E. Le Guen, E. Lacoste, and C. Arvieu. Main defects observed in aluminum alloy parts produced by SLM: From causes to consequences. *Additive Manufacturing*, 22:165–175, 2018. ISSN 22148604. doi: 10.1016/j.addma.2018.05.005.

[37] L. Wang, Y. Zhang, H. Y. Chia, and W. Yan. Mechanism of keyhole pore formation in metal additive manufacturing. *npj Computational Materials*, 8(1), 2022. ISSN 2057-3960. doi: 10.1038/s41524-022-00699-6.

[38] J.-P. Kruth, J. Deckers, E. Yasa, and R. Wauthl*é*. Assessing and comparing influencing factors of residual stresses in Selective Laser Melting using a novel analysis method. *Journal of Engineering Manufacture*, 226(6):980–991, 2012. doi: https://doi.org/10.1177/0954405412437085.

[39] P. Mercelis and J. Kruth. Residual stresses in selective laser sintering and selective laser melting. *Rapid Prototyping Journal*, 12(5):254–265, 2006. ISSN 1355-2546. doi: 10.1108/13552540610707013.

[40] C. Li, Z. Y. Liu, X. Y. Fang, and Y. B. Guo. Residual Stress in Metal Additive Manufacturing. *Procedia CIRP*, 71:348–353, 2018. doi: https://doi.org/10.1016/j.procir.2018.05.039.

[41] A. Niku-Lari. *Advances in surface treatments*, volume 4 of *Residual stresses : technology - applications - effects*. Pergamon Press, Oxford, 1987. doi: https://search.ebscohost.com/login.aspx?direct=true\&scope=site\&db=nlebk\&db=nlabk\&AN=922526.

[42] N. Read, W. Wang, K. Essa, and M. M. Attallah. Selective laser melting of AlSi10Mg alloy: Process optimisation and mechanical properties development. *Materials & Design*, 65:417–424, 2015. doi: https://doi.org/10.1016/j.matdes.2014.09.044.

[43] A. H. Maamoun, M. Elbestawi, G. K. Dosbaeva, and S. C. Veldhuis. Thermal Post-processing of AlSi10Mg parts produced by Selective Laser. *Additive Manufacturing*, 21:234–247, 2018. doi: https://doi.org/10.1016/j.addma.2018.03.014.

[44] E. Beevers, A. D. Brandão, J. Gumpinger, M. Gschweitl, C. Seyfertc, P. Hofbauer, T. Rohra, and T. Ghidini. Fatigue properties and material characteristics of additively manufactured AlSi10Mg – Effect of the contour parameter on the microstructure, density, residual stress, roughness and mechanical properties. *International Journal of Fatigue*, 117:148–162, 2018. doi: https://doi.org/10.1016/j.ijfatigue.2018.08.023.

[45] M. Guo and X. Jiang. Microstructure, Mechanical Properties and Residual Stress of Selective Laser Melted AlSi10Mg. *Journal of Materials Engineering and Performance*, 28:6753–6760, 2019. doi: https://doi.org/10.1007/s11665-019-04423-2.

[46] S. Marola, S. Bosia, A. Veltro, G. Fiore, D. Manfredi, M. Lombardi, G. Amato, M. Baricco, and L. Battezzati. Residual stresses in additively manufactured AlSi10Mg: Raman spectroscopy and X-ray diffraction analysis. *Materials & Design*, 202, 2021. ISSN 02641275. doi: 10.1016/j.matdes.2021.109550.

[47] S. Romano, L. Patriarca, S. Foletti, and S. Beretta. LCF behaviour and a comprehensive life prediction model for AlSi10Mg obtained by SLM. *International Journal of Fatigue*, 117:47–62, 2018. ISSN 01421123. doi: 10.1016/j.ijfatigue.2018.07.030.

[48] L. Zhao, J. G. Santos Macias, A. Dolimont, A. Simar, and E. Riviere-Lorphevre. Comparison of residual stresses obtained by the crack compliance method for parts produced by different metal additive manufacturing techniques and after friction stir processing. *Additive Manufacturing*, 36:101499, 2020. doi: https://doi.org/10.1016/j.addma.2020.101499.

[49] B. Liu, B. Li, and Z. Li. Selective laser remelting of an additive layer manufacturing process on AlSi10Mg. *Results in Physics*, 12:982–988, 2019. ISSN 22113797. doi: 10.1016/j.rinp.2018.12.018.

[50] I. Roveda, I. Serrano-Munoz, A. Kromm, and M. Madia. Investigation of residual stresses and microstructure effects on the fatigue behaviour of a L-PBF AlSi10Mg alloy. *Procedia Structural Integrity*, 38C:564–571, 2022. doi: https://doi.org/10.1016/j.prostr.2022.03.057.

[51] C. Colombo, C. A. Biffi, J. Fiocchi, and A. Tuissi. Effect of Optimized Heat Treatments on the Tensile Behavior and Residual Stresses of Selective Laser

Melted AlSi10Mg Samples. *Key Engineering Materials*, 813:364–369, 2019. doi: https://doi.org/10.4028/www.scientific.net/KEM.813.364.

[52] A. Salmi and E. Atzeni. Residual stress analysis of thin AlSi10Mg parts produced by Laser Powder Bed Fusion. *Virtual and Physical Prototyping*, 15(1):49–61, 2019. ISSN 1745-2759 1745-2767. doi: 10.1080/17452759.2019.1650237.

[53] L. Tonelli, E. Liverani, A. Morri, and L. Ceschini. Role of Direct Aging and Solution Treatment on Hardness, Microstructure and Residual Stress of the A357 (AlSi7Mg0.6) Alloy Produced by Powder Bed Fusion. *Metallurgical and Materials Transactions B*, 52(4):2484–2496, 2021. ISSN 1073-5615 1543-1916. doi: 10.1007/s11663-021-02179-6.

[54] P. Van Cauwenbergh, A. Beckers, L. Thijs, B. Van Hooreweder, and K. Vanmeensel. Heat Treatment Optimization via Thermo-Physical Characterization of AlSi7Mg and AlSi10Mg Manufactured by Laser Powder Bed Fusion (LPBF). *Euro PM2018 Congress*, Euro PM2018 Congress Proceedings, 2018.

[55] L. Zhuo, Z. Wang, H. Zhang, E. Yin, Y. Wang, T. Xu, and C. Li. Effect of post-process heat treatment on microstructure and properties of selective laser melted AlSi10Mg alloy. *Materials Letters*, 234:196–200, 2019. ISSN 0167577X. doi: 10.1016/j.matlet.2018.09.109.

[56] Z. Dong, X. Zhang, W. Shi, H. Zhou, H. Lei, and J. Liang. Study of size effect on microstructure and mechanical properties of AlSi10Mg samples made by selective laser melting. *Materials*, 11(12):2463, 2018. ISSN 1996-1944.

[57] F. Trevisan, F. Calignano, M. Lorusso, J. Pakkanen, A. Aversa, E. P. Ambrosio, M. Lombardi, P. Fino, and D. Manfredi. On the Selective Laser Melting (SLM) of the AlSi10Mg Alloy: Process, Microstructure, and Mechanical Properties. *Materials (Basel)*, 10(1), 2017. ISSN 1996-1944 (Print) 1996-1944 (Linking). doi: 10.3390/ma10010076.

[58] C. Jing, H. Wei, W. Xiuzhuan, C. Songlin, and Y. Zhiyi. Microstructure, porosity and mechanical properties of selective laser melted AlSi10Mg. *Chinese Journal of Aeronautics*, 33(7):2043–2054, 2020. ISSN 1000-9361.

[59] W. Li, S. Li, J. Liu, A. Zhang, Y. Zhou, Q. Wei, C. Yan, and Y. Shi. Effect of heat treatment on AlSi10Mg alloy fabricated by selective laser melting: Microstructure evolution, mechanical properties and fracture mechanism. *Materials Science and Engineering: A*, 663:116–125, 2016. ISSN 0921-5093.

[60] I. Rosenthal, A. Stern, and N. Frage. Microstructure and mechanical properties of AlSi10Mg parts produced by the laser beam additive manufacturing (AM) technology. *Metallography, Microstructure, and Analysis*, 3(6):448–453, 2014. ISSN 2192-9270.

[61] Y. J. Liu, Z. Liu, Y. Jiang, G. W. Wang, Yang Yang, and L. C. Zhang. Gradient in microstructure and mechanical property of selective laser melted AlSi10Mg. *Journal of Alloys and Compounds*, 735:1414–1421, 2018. ISSN 0925-8388.

[62] K. Zyguła, B. Nosek, H. Pasiowiec, and N. Szysiak. [mechanical properties and microstructure of alsi10mg alloy obtained by casting and slm technique.

[63] Z. H. Xiong, S. L. Liu, S. F. Li, Y. Shi, Ya Feng Yang, and R. D. K. Misra. Role of melt pool boundary condition in determining the mechanical properties of selective laser melting AlSi10Mg alloy. *Materials Science and Engineering: A*, 740:148–156, 2019. ISSN 0921-5093.

[64] M. Fousová, D. Dvorský, A. Michalcová, and D. Vojtěch. Changes in the microstructure and mechanical properties of additively manufactured AlSi10Mg alloy after exposure to elevated temperatures. *Materials Characterization*, 137:119–126, 2018. ISSN 1044-5803.

[65] N. T. Aboulkhair, I. Maskery, C. Tuck, I. Ashcroft, and N. M. Everitt. On the formation of AlSi10Mg single tracks and layers in selective laser melting: Microstructure and nano-mechanical properties. *Journal of Materials Processing Technology*, 230:88–98, 2016. ISSN 0924-0136.

[66] A. H. Maamoun, Y. F. Xue, M. A. Elbestawi, and S. C. Veldhuis. The effect of selective laser melting process parameters on the microstructure and mechanical properties of Al6061 and AlSi10Mg alloys. *Materials*, 12(1):12, 2018. ISSN 1996-1944.

[67] X. Li, D. Yi, X. Wu, J. Zhang, X. Yang, Z. Zhao, Y. Feng, J. Wang, P. Bai, and B. Liu. Effect of construction angles on microstructure and mechanical properties of AlSi10Mg alloy fabricated by selective laser melting. *Journal of Alloys and Compounds*, 881:160459, 2021. ISSN 0925-8388.

[68] N. O. Larrosa, W. Wang, N. Read, M. H. Loretto, C. Evans, J. Carr, U. Tradowsky, M. M. Attallah, and P. J. Withers. Linking microstructure and processing defects to mechanical properties of selectively laser melted AlSi10Mg alloy. *Theoretical and Applied Fracture Mechanics*, 98:123–133, 2018. ISSN 0167-8442.

[69] S.D. Saravanan and M Senthil Kumar. Effect of mechanical properties on rice husk ash reinforced aluminum alloy (AlSi10Mg) matrix composites. *Procedia Engineering*, 64:1505–1513, 2013. ISSN 1877-7058.

[70] P. Wang, H. Lei, X. Zhu, H. Chen, and D. Fang. Influence of manufacturing geometric defects on the mechanical properties of AlSi10Mg alloy fabricated by selective laser melting. *Journal of Alloys and Compounds*, 789:852–859, 2019. ISSN 0925-8388.

[71] Z. Li, Y. Nie, B. Liu, Z. Kuai, M. Zhao, and F. Liu. Mechanical properties of AlSi10Mg lattice structures fabricated by selective laser melting. *Materials & Design*, 192: 108709, 2020. ISSN 0264-1275.

[72] N. E. Uzan, R. Shneck, O. Yeheskel, and N. Frage. High-temperature mechanical properties of AlSi10Mg specimens fabricated by additive manufacturing using selective laser melting technologies (AM-SLM). *Additive Manufacturing*, 24:257–263, 2018. ISSN 2214-8604.

[73] Z. Dong, Y. Liu, W. Li, and J. Liang. Orientation dependency for microstructure, geometric accuracy and mechanical properties of selective laser melting AlSi10Mg lattices. *Journal of Alloys and Compounds*, 791:490–500, 2019. ISSN 0925-8388.

[74] C. Zhang, H. Zhu, Z. Hu, L. Zhang, and X. Zeng. A comparative study on single-laser and multi-laser selective laser melting AlSi10Mg: defects, microstructure and mechanical properties. *Materials Science and Engineering: A*, 746:416–423, 2019. ISSN 0921-5093.

[75] I. Rosenthal, E. Tiferet, M. Ganor, and A. Stern. Post-processing of AM-SLM AlSi10Mg specimens: Mechanical properties and fracture behaviour. *Annals of "Dunarea de Jos" University of Galati. Fascicle XII, Welding Equipment and Technology*, 26:33–38, 2015. ISSN 2668-6163.

[76] K. Kempen, L. Thijs, J. Van Humbeeck, and J.-P. Kruth. Mechanical properties of AlSi10Mg produced by selective laser melting. *Physics Procedia*, 39:439–446, 2012. ISSN 1875-3892.

[77] T. Hirata, T. Kimura, and T. Nakamoto. Effect of Internal Pores on Fatigue Properties in Selective Laser Melted AlSi10Mg Alloy. *Materials Transactions*, 63(7):1013–1020, 2022. ISSN 1345-9678 1347-5320. doi: 10.2320/matertrans.MT-L2022005.

[78] L. Zhao, J. G. Santos Macías, L. Ding, H. Idrissi, and A. Simar. Damage mechanisms in selective laser melted AlSi10Mg under as built and different post-treatment

conditions. *Materials Science and Engineering: A*, 764, 2019. ISSN 09215093. doi: 10.1016/j.msea.2019.138210.

[79] U. Zerbst, G. Bruno, J. Y. Buffiere, T. Wegener, T. Niendorf, T. Wu, X. Zhang, N. Kashaev, G. Meneghetti, N. Hrabe, M. Madia, T. Werner, K. Hilgenberg, M. Koukolikova, R. Prochazka, J. Dzugan, B. Moller, S. Beretta, A. Evans, R. Wagener, and K. Schnabel. Damage tolerant design of additively manufactured metallic components subjected to cyclic loading: State of the art and challenges. *Prog Mater Sci*, 121, 2021. ISSN 0079-6425 (Print) 0079-6425 (Linking). doi: 10.1016/j.pmatsci.2021.100786.

[80] I. Serrano-Munoz, J. Y. Buffiere, R. Mokso, C. Verdu, and Y. Nadot. Location, location & size: defects close to surfaces dominate fatigue crack initiation. *Sci Rep*, 7:45239, 2017. ISSN 2045-2322 (Electronic) 2045-2322 (Linking). doi: 10.1038/srep45239.

[81] T. M. Mower and M. J. Long. Mechanical behavior of additive manufactured, powder-bed laser-fused materials. *Materials Science and Engineering: A*, 651: 198–213, 2016. ISSN 09215093. doi: 10.1016/j.msea.2015.10.068.

[82] M. H. Nasab, A. Giussani, D. Gastaldi, V. Tirelli, and M. Vedani. Effect of Surface and Subsurface Defects on Fatigue Behavior of AlSi10Mg Alloy Processed by Laser Powder Bed Fusion (L-PBF). *Metals*, 9(10), 2019. ISSN 2075-4701. doi: 10.3390/met9101063.

[83] N. E. Uzan, R. Shneck, O. Yeheskel, and N. Frage. Fatigue of AlSi10Mg specimens fabricated by additive manufacturing selective laser melting (AM-SLM). *Materials Science and Engineering: A*, 704:229–237, 2017. ISSN 09215093. doi: 10.1016/j.msea.2017.08.027.

[84] A. Kempf, J. Kruse, M. Madia, and K. Hilgenberg. Correlation between quasistatic und fatigue properties of additively manufactured AlSi10Mg using Laser Powder Bed Fusion. *Procedia Structural Integrity*, 38:77–83, 2022. doi: https://doi.org/10.1016/j.prostr.2022.03.009.

[85] J. N. Domfang N., Y. Nadot, G. Henaff, J. Nicolai, W. H. Kan, J. M. Cairney, and L. Ridosz. Fatigue properties of AlSi10Mg produced by Additive Layer Manufacturing. *International Journal of Fatigue*, 119:160–172, 2019. ISSN 01421123. doi: 10.1016/j.ijfatigue.2018.09.029.

[86] I. Maskery, N.T. Aboulkhair, C. Tuck, R.D. Wildman, I.A. Ashcroft, N.M. Everitt, and R.J.M. Hague. Fatigue Performance Enhancement of Selectively Laser Melted Aluminum Alloy by Heat Treatment. *26th Annual International Solid Freeform Fabrication Symposium*, 2015.

[87] N. T. Aboulkhair, I. Maskery, C. Tuck, I. Ashcroft, and N. M. Everitt. Improving the fatigue behaviour of a selectively laser melted aluminium alloy: Influence of heat treatment and surface quality. *Materials & Design*, 104:174–182, 2016. ISSN 0264-1275. doi: https://doi.org/10.1016/j.matdes.2016.05.041.

[88] C. Zhang, H. Zhu, H. Liao, Y. Cheng, Z. Hu, and X. Zeng. Effect of heat treatments on fatigue property of selective laser melting AlSi10Mg. *International Journal of Fatigue*, 116:513–522, 2018. ISSN 01421123. doi: 10.1016/j.ijfatigue.2018.07.016.

[89] A. Tridello, J. Fiocchi, C. A. Biffi, G. Chiandussi, M. Rossetto, A. Tuissi, and D. S. Paolino. Influence of the annealing and defects on the VHCF behavior of an SLM AlSi10Mg alloy. *Fatigue & Fracture of Engineering Materials & Structures*, 42(12): 2794–2807, 2019. ISSN 8756-758X 1460-2695. doi: 10.1111/ffe.13123.

[90] A. Yadollahi and N. Shamsaei. Additive manufacturing of fatigue resistant materials: Challenges and opportunities. *International Journal of Fatigue*, 98:14–31, 2017. ISSN 01421123. doi: 10.1016/j.ijfatigue.2017.01.001.

[91] U. Zerbst and K. Hilgenberg. Damage development and damage tolerance of structures manufactured by selective laser melting – a review. *Procedia Structural Integrity*, pages 141–148, 2017. doi: https://doi.org/10.1016/j.prostr.2017.11.071.

[92] J. Polak. Cyclic deformation, crack initiation, and low-cycle fatigue. *Comprehensive Structural Integrity*, 4(Cyclic loading and Fracture):1–39, 2003.

[93] U. Zerbst, M. Madia, B. Schork, J. Hensel, P. Kucharczyk, D. Tchoffo Ngoula, D. Tchuindjang, J. Bernhard, and C. Beckmann. *Fatigue and Fracture of Weldments - The IBESS Approach for the Determination of the Fatigue Life and Strength of Weldments by Fracture Mechanics Analysis*. Springer Cham, 2019. doi: 10.1007/978-3-030-04073-4.

[94] S. Ishihara, Y. Sugai, and A. J. McEvily. On the Distinction Between Plasticity- and Roughness-Induced Fatigue Crack Closure. *Metallurgical and Materials Transactions A*, 43(9):3086–3096, 2012. ISSN 1073-5623. doi: 10.1007/s11661-012-1121-9.

[95] L. Lawson, E.Y. Chen, and M. Meshi. Near-threshold fatigue: a review. *International Journal of Fatigue*, 21:S15–S34, 1999. doi: https://doi.org/10.1016/S0142-1123(99)00053-5.

[96] K. Tanaka and Y. Akiniwa. Resistance-curve method for predicting propagation threshold of short fatigue cracks at notches. *Engineering Fracture Mechanics*, 30(6): 863–876, 1988. ISSN 0013-7944. doi: https://doi.org/10.1016/0013-7944(88)90146-4.

[97] ASTM. ASTM E 647-93. *Standard Test Method for Measurement of Fatigue Crack Growth Rates, Annual Book of ASTM Standards*, 03.01(569):569–596, 1994. doi: 10.1520/e0647-15.

[98] ISO12108:2018. Metallic materials — Fatigue testing — Fatigue crack growth method. *77.040.10 Mechanical testing of metals*, page 53, 2018.

[99] J. Maierhofer, S. Kolitsch, R. Pippan, H. Gänser, M. Madia, and U. Zerbst. The cyclic R-curve – Determination, problems, limitations and application. *Engineering Fracture Mechanics*, 198:45–64, 2018. ISSN 00137944. doi: 10.1016/j.engfracmech.2017.09.032.

[100] R. O. Ritchie and J. Lankford. Small Fatigue Cracks: A Statement of the Problem and Potential Solutions. *Materials Science and Engineering*, 84:11–16, 1986. doi: https://doi.org/10.1016/0025-5416(86)90217-X.

[101] R. O. Ritchie. Mechanisms of Fatigue Crack Propagation in Metals, Ceramics and Composites: Role of Crack Tip Shielding. *Materials Science and Engineering*, A103: 15–28, 1988.

[102] R. Pippan. The effective threshold of fatigue crack propagation in aluminium alloys. I. The influence of yield stress and chemical composition. *Philosophical Magazine A*, 77(4):861–873, 1998. ISSN 0141-8610 1460-6992. doi: 10.1080/01418619808221216.

[103] U. Krupp, A. Giertler, S. Siegfanz, and W. Michels. Mutual Interaction between Fatigue Crack Initiation/Propagation and Microstructural Features in Cast Aluminum Alloys. *Advanced Materials Research*, 891-892:488–493, 2014. ISSN 1662-8985. doi: 10.4028/www.scientific.net/AMR.891-892.488.

[104] S. Siegfanz, A. Giertler, W. Michels, and U. Krupp. Influence of the microstructure on the fatigue damage behaviour of the aluminium cast alloy AlSi7Mg0.3. *Materials*

Science and Engineering: A, 565:21–26, 2013. ISSN 09215093. doi: 10.1016/j.msea.2012.12.047.

[105] M. F. Hafiz and T. Kobayashi. A study on the microstructure-fracture behavior relations in Al-Si casting alloys. *Scripta Metallurgica et Materialia*, 30:475–480, 1994. doi: 10.1016/0956-716X(94)90606-8.

[106] M. Di Giovanni, J. T. O. de Menezes, G. Bolelli, E. Cerri, and E. M. Castrodeza. Fatigue crack growth behavior of a selective laser melted AlSi10Mg. *Engineering Fracture Mechanics*, 217, 2019. ISSN 00137944. doi: 10.1016/j.engfracmech.2019.106564.

[107] J. G. Santos Macías, C. Elangeswaran, L. Zhao, J. Buffière, B. Van Hooreweder, and A. Simar. Fatigue crack nucleation and growth in laser powder bed fusion AlSi10Mg under as built and post-treated conditions. *Materials & Design*, 210, 2021. ISSN 02641275. doi: 10.1016/j.matdes.2021.110084.

[108] ASTM E466-21. Standard Practice for Conducting Force Controlled Constant Amplitude Axial Fatigue Tests of Metallic Materials. page 7, 2021.

[109] ISO 1099:2017. Metallic materials — Fatigue testing — Axial force-controlled method. page 24, 2017.

[110] ISO 12106:2017. Metallic materials — Fatigue testing —Axial-strain-controlled method. page 38, 2017.

[111] E606/E606M – 12. Standard Test Method for Strain-Controlled Fatigue Testing. page 16, 2020.

[112] Oxford Instrument. HKL Channel 5. *SP9E*, 2008.

[113] F. Bachmann, R. Hielscher, and H. Schaeben. Texture Analysis with MTEX - Free and Open Source Software Toolbox. *Solid State Phenomena*, 160:63–68, 2021. doi: https://doi.org/10.4028/www.scientific.net/SSP.160.63.

[114] Volume Graphics GmbH. VGSTUDIO MAX. 2019. URL `https://www.volumegraphics.com/en/products/vgsm.html`.

[115] ISO 6892-1:2019. Metallic materials — Tensile testing — Part 1: Method of test at room temperature. 2019.

[116] ISO 6507-1:2018. Metallic materials — Vickers hardness test — Part 1: Test method. 2018.

[117] NanoFocus AG. μsoft analysis premium 8.0.9173. 2021.

[118] X.X. Zhang, A. Lutz, H. Andrä, M. Lahres, W. M. Gan, E. Maawad, and C. Emmelmann. Evolution of microscopic strains, stresses, and dislocation density during in-situ tensile loading of additively manufactured AlSi10Mg alloy. *International Journal of Plasticity*, 139:102946, 2021. doi: https://doi.org/10.1016/j.ijplas.2021.102946.

[119] ISO-21432. Non-Destructive Tesing—Standard Test Method for Determining Residual Stresses by Neutron Diffraction; International. 2019.

[120] Helmholtz-Zentrum Berlin für Materialien und Energie. In-situ X-ray Lab. URL `https://www.helmholtz-berlin.de/pubbin/igama_output?modus=einzel&sprache=en&gid=2117&typoid=68892`.

[121] I. Serrano-Munoz, S. Cabeza, A. Evans, M. Madia, T. Mishurova, T. Pirling, and I. Roveda. Effect of as-built residual stress state on the fatigue response of a LPBF AlSi10Mg alloy. 2021. doi: doi:10.5291/ILL-DATA.1-02-338.

[122] A. Evans, I. Roveda, I. Serrano-Munoz, and T. Mishurova. Evaluation of inter-phase strains present in as-built and heat treated LPBF AlSi10Mg materials. (MA-5011), 2022. doi: doi:10.15151/ESRF-ES-819996597.

[123] G. Albertini, G. Bruno, B.D. Dunn, F. Fiori, W. Reimers, and J.S. Wright. Comparative neutron and X-ray Residual stress measurements in AA-2219 welded plate. *Materials Science Engineering A*, 224:157–165, 1997. doi: https://doi.org/10.1016/S0921-5093(96)10546-3.

[124] K. An, L. Yuan, L. Dial, I. Spinelli, A. D. Stoica, and Y. Gao. Neutron residual stress measurement and numerical modeling in a curved thin-walled structure by laser powder bed fusion additive manufacturing. *Materials & Design*, 135:122–132, 2017. doi: https://doi.org/10.1016/j.matdes.2017.09.018.

[125] ISO 12108:2012. Metallic materials — Fatigue testing - Fatigue crack growth method. page 43, 2012.

[126] B. Tabering, P. Powell, and R. Pippan. Resistance Curves for the Threshold of Fatigue Crack Propagation in Particle Reinforced Aluminium Alloys. *ASTM STP 1372*, Fatigue Crack Growth Thresholds, Endurance Limits, and Design, 2000.

[127] B. Tabernig and R. Pippan. Determination of the length dependence of the threshold for fatigue crack propagation. *Engineering Fracture Mechanics*, 69:899–907, 2002.

[128] R. Pippan and A. Hohenwarter. Fatigue crack closure: a review of the physical phenomena. *Fatigue Fract Eng Mater Struct*, 40(4):471–495, 2017. ISSN 8756-758X (Print) 1460-2695 (Linking). doi: 10.1111/ffe.12578.

[129] R. Pippan, F. O. Riemelmoser, H. Weinhandl, and H. Kreuzer. Plasticity-induced crack closure under plane-strain conditions in the near-threshold regime. *Philosophical Magazine A*, 82(17-18):3299–3309, 2002. ISSN 0141-8610 1460-6992. doi: 10.1080/01418610208240442.

[130] M. Zerbst, U. Madia. Fracture mechanics-based assessment of the fatigue strength: approach for the determination of the initial crack size. *Fatigue Fract Eng Mater Struct*, 38:1066–1075, 2015. doi: https://doi.org/10.1111/ffe.12288.

[131] J. Maierhofer, R. Pippan, and H. P. Gänser. Modified NASGRO equation for physically short cracks. *International Journal of Fatigue*, 59:200–207, 2014. ISSN 01421123. doi: 10.1016/j.ijfatigue.2013.08.019.

[132] R.G. Forman and S.R. Mettu. Behavior of surface and corner cracks subjected to tensile and bending loads in Ti-6Al-4V alloy. *Fracture Mechanics 22nd Symposium*, 1, 1992.

[133] J. J. Newman. A crack opening stress equation for fatigue crack growth. *International Journal of Fatigue*, 24:R131 – R135, 1984. doi: https://doi.org/10.1007/BF00020751.

[134] J.C. Newman. A crack opening stress equation for fatigue crack growth. *Int J Fract*, 24:R131–R135, 1984. doi: https://doi.org/10.1007/BF00020751.

[135] ISO 12107:2012. Metallic materials — Fatigue testing — Statistical planning and analysis of data. 2012.

[136] W. Ramberg and W. R. Osgood. Description of stress-strain curves by three parameters. *National Bureau of Standards, Washington DC*, 1943.

[137] J. R. Hollomon. Tensile deformation. *Transactions of AIME*, 162:268–277, 1945.

[138] Y. Murakami, T. Takagi, K. Wada, and H. Matsunaga. Essential structure of s-n curve: Prediction of fatigue life and fatigue limit of defective materials and nature of scatter. *International Journal of Fatigue*, 146, 2021. ISSN 01421123. doi: 10.1016/j.ijfatigue.2020.106138.

[139] Y. Murakami. *Metal Fatigue: Effect of Small Defects and Nonmetallic Inclusions*. Academic Press. Elsevier, 2002.

[140] M. H. El Haddad, K. N. Smith, and Topper T. H. Fatigue crack propagation of short cracks. *J. Eng. Mater. Technol.*, 101:42–46, 1979.

[141] M. H. El Haddad, T. H. Topper, and K. N. Smith. Prediction of non propagating cracks. *Engineering Fracture Mechanics*, 11:573–584, 1979.

[142] H. Kitagawa and S. Takahashi. Applicability of fracture mechanics to very small cracks or cracks in the early stage. *Proceeding of the second international conference on mechanical behavior of materials, ASM*, pages 627–631, 1976.

[143] Y Murakami and M Endo. The area parameter model for small defects and non-metallic inclusions in fatigue strength: experimental evidences and applications. *Theoretical concepts and numerical analysis of fatigue*, pages 51–71, 1992.

[144] B. Atzori, P. Lazzarin, and G. Meneghetti. Fracture mechanics and notch sensitivity. *Fatigue Fracture of Engineering Materials and Structures*, 26(3):257–267, 2003. ISSN 8756-758X 1460-2695. doi: 10.1046/j.1460-2695.2003.00633.x.

[145] M. Madia, U. Zerbst, H. Th. Beier, and B. Schork. The ibess model – elements, realisation and validation. *Engineering Fracture Mechanics*, 198:171–208, 2018. ISSN 00137944. doi: 10.1016/j.engfracmech.2017.08.033.

[146] N. E. Dowling. *Crack growth during low-cycle fatigue of smooth axial specimens*. ASTM International, 1977.

[147] H. Qin, V. Fallah, Q. Dong, M. Brochu, M. R. Daymond, and M. Gallerneault. Solidification pattern, microstructure and texture development in Laser Powder Bed Fusion (LPBF) of Al10SiMg alloy. *Materials Characterization*, 145:29–38, 2018. ISSN 10445803. doi: 10.1016/j.matchar.2018.08.025.

[148] K. V. Yang, P. Rometsch, T. Jarvis, J. Rao, S. Cao, C. Davies, and X. Wu. Porosity formation mechanisms and fatigue response in Al-Si-Mg alloys made by selective laser melting. *Materials Science and Engineering: A*, 712:166–174, 2018. doi: https://doi.org/10.1016/j.msea.2017.11.078.

[149] I. Maskery, N. T. Aboulkhair, M. R. Corfield, C. Tuck, A. T. Clare, R. K. Leach, R. D. Wildman, I. A. Ashcroft, and R. J. M. Hague. Quantification and characterisation of porosity in selectively laser melted AlSi10Mg using X-ray computed tomography.

Materials Characterization, 111:193–204, 2016. ISSN 1044-5803. doi: https://doi.org/10.1016/j.matchar.2015.12.001.

[150] A. K. Syed, B. Ahmad, H. Guo, T. Machry, D. Eatock, J. Meyer, M. E. Fitzpatrick, and X. Zhang. An experimental study of residual stress and direction-dependence of fatigue crack growth behaviour in as-built and stress-relieved selective-laser-melted Ti6Al4V. *Materials Science and Engineering: A*, 755:246–257, 2019. doi: https://doi.org/10.1016/j.msea.2019.04.023.

[151] T. Thiede, S Cabeza, T. Mishurova, N. Nadammal, A. Kromm, J. Bode, C. Haberland, and G. Bruno. Residual Stress in Selective Laser Melted Inconel 718: Influence of the Removal from Base Plate and Deposition Hatch Length. *Materials Performance and Characterization*, 7:717–735, 2018. doi: https://doi.org/10.1520/MPC20170119.

[152] A. Ulbricht, S. J. Altenburg, M. Sprengel, K. Sommer, G. Mohr, T. Fritsch, T. Mishurova, I. Serrano-Munoz, A. Evans, M. Hofmann, and G. Bruno. Separation of the Formation Mechanisms of Residual Stresses in LPBF 316L. *Metals*, 10: 1234, 2020. doi: https://doi.org/10.3390/met10091234.

[153] Z. Wang, E. Denlinger, P. Michaleris, A. D. Stoica, D. Mac Allison, and M. Beese. Residual stress mapping in Inconel 625 fabricated through additive manufacturing: Method for neutron diffraction measurements to validate thermomechanical model predictions. *Materials & Design*, 113:169–177, 2017. doi: https://doi.org/10.1016/j.matdes.2016.10.003.

[154] N. T. Aboulkhair, N. M. Everitt, I. Ashcroft, and C. Tuck. Reducing porosity in AlSi10Mg parts processed by selective laser melting. *Additive Manufacturing*, 1-4: 77–86, 2014. doi: https://doi.org/10.1016/j.addma.2014.08.001.

[155] A. Ladewig, G. Schlick, M. Fisser, V. Schulze, and U. Glatzel. Influence of the shielding gas flow on the removal of process by-products in the selective laser melting process. *Additive Manufacturing*, 10:1–9, 2016. doi: https://doi.org/10.1016/j.addma.2016.01.004.

[156] P. J. Withers, M. Preuss, A. Steuwer, and J. W. L. Pang. Methods for obtaining the strain-free lattice parameter when using diffraction to determine residual stress. *Journal of Applied Cristallography*, 40:891–904, 2007. doi: https://doi.org/10.1107/S0021889807030269.

[157] R.J. Moat, A.J. Pinkerton, L. Li, P.J. Withers, and M. Preuss. Residual stresses in laser direct metal deposited Waspaloy. *Materials Science and Engineering: A*, 528: 2288–2298, 2011. doi: https://doi.org/10.1016/j.msea.2010.12.010.

[158] A. Pourheidar, L. Patriarca, M. Madia, T. Werner, and S. Beretta. Progress in the measurement of the cyclic R-curve and its application to fatigue assessment. *Engineering Fracture Mechanics*, 260:108122, 2022. ISSN 0013-7944. doi: https://doi.org/10.1016/j.engfracmech.2021.108122.

[159] J. Maierhofer, R. Pippan, and H. Gänser. Modified NASGRO Equation for Short Cracks and Application to the Fitness-for-purpose Assessment of Surface-treated Components. *Procedia Materials Science*, 3:930–935, 2014. ISSN 22118128. doi: 10.1016/j.mspro.2014.06.151.

[160] R. A. Schmidt and P. Paris. Threshold for fatigue crack propagation and the effects of load ratio and frequency. *ASTM special technical publications*, pages 79–94, 1973.

[161] D.A. Lados and D. Apelian. Fatigue Crack Growth Characteristics in Cast Al-Si-Mg Alloys - Part I: Effect of Processing Conditions and Microstructure. *Materials Science and Engineering A*, A385:200–211, 2004.

[162] U. Zerbst, M. Vormwald, R. Pippan, H. Gänser, C. Sarrazin-Baudoux, and M. Madia. About the fatigue crack propagation threshold of metals as a design criterion – A review. *Engineering Fracture Mechanics*, 153:190–243, 2016. ISSN 00137944. doi: 10.1016/j.engfracmech.2015.12.002.

[163] R. Pippan, G. Strobl, H. Kreuzer, and C. Motz. Asymmetric crack wake plasticity – a reason for roughness induced crack closure. *Acta Materialia*, 52(15):4493–4502, 2004. ISSN 13596454. doi: 10.1016/j.actamat.2004.06.014.

[164] G. T. Gray, J. C. Williams, and A. W. Thomson. Roughness-Induced Crack Closure. An Explanation for Microstructurally Sensitive Fatigue Crack Growth. *Metallurgical Transactions A*, 14A:421–433, 1982.

[165] S. Beretta. More than 25 years of extreme value statistics for defects: Fundamentals, historical developments, recent applications. *International Journal of Fatigue*, 151, 2021. ISSN 01421123. doi: 10.1016/j.ijfatigue.2021.106407.

[166] Y. Murakami, Y. Tazunoki, and T. Endo. Existence of the Coaxing Effect and Effects of Small Artificial Holes on Fatigue Strength of an Aluminum Alloy and 70-30 Brass. *Metallurigical Transactions A*, 15A:2029–2038, 1984.

[167] J. Goodman. *Mechanics applied to engineering*. Longmans, Green, 1919.

[168] B. P. Haigh. Experiments on the fatigue of brasses. *Journal of the Institute of Metals*, 18(2):55–86, 1917.

[169] B. M. Schönbauer and H. Mayer. Effect of small defects on the fatigue strength of martensitic stainless steels. *International Journal of Fatigue*, 127:362–375, 2019. ISSN 01421123. doi: 10.1016/j.ijfatigue.2019.06.021.

[170] M. Chapetti. Fatigue propagation threshold of short cracks under constant amplitude loading. *International Journal of Fatigue*, 25(12):1319–1326, 2003. ISSN 01421123. doi: 10.1016/s0142-1123(03)00065-3.

[171] G. Masing. Internal stresses and hardening of brass. *Proc. 2^{nd} Int. Congress for Appl. Mech.*, 1926.